Magnetoelastic Coupling in Ferromagnetic Films and Surface Stress Studies on Ir(100)

DISSERTATION

zur Erlangung des akademischen Grades

doctor rerum naturalium
(Dr. rer. nat.)
genehmigt durch

Martin-Luther-Universität
Halle-Wittenberg

vorgelegt von
Frau M. Sc. Zhen Tian
geboren am 06.01.1978 in Hebei, China

Gutachter:

1. Prof. Dr. Jürgen Kirschner

2. Prof. Dr. Wolf Widdra

3. Prof. Dr. Reinhold Koch

Halle (Saale), March 28, 2008

Verteidigungsdatum: February 19, 2008

Abstract

Measurements on the correlation between stress, strain and magnetic anisotropy of epitaxial monolayers are performed in this work. To this end, mechanical stress during film growth and stress during magnetization processes are measured directly by the optical cantilever curvature technique.

Epitaxial misfit induced film stress is measured for Fe, Ni and Co monolayers on Ir(100). Film stresses of the order of several GPa are detected, which are ascribed to the epitaxial misfit. The stress measurements also indicate structural and morphological changes in the growing film. The first 2 monolayers of Fe on Ir(100) can be described as a fcc precursor, which serve as a template for the subsequent growth of bcc Fe at higher thickness. Ni and Co are found to grow in a fcc phase on Ir.

The results on the magnetoelastic stress indicate that the magnetoelastic coupling coefficients B_1^{eff} and B_2^{eff} of Fe, Ni and Co deviate sharply from the respective bulk behavior, and they suggest that strain may play an important role for this non-bulklike magnetoelastic behavior. The role of this non-linear magnetoelastic coupling for the magnetic anisotropy of ferromagnetic monolayers is studied. The magnetic anisotropy for out-of-plane magnetization is analyzed. MOKE measurements reveal that the easy magnetization axis is in-plane for Fe and Co films on Ir(100), and changes from out-of-plane to in-plane for Ni at about 15 ML for increasing film thickness. These experimental observations can be well described by the measured magnetoelastic coupling coefficients.

The relation between surface stress and surface reconstruction of the Ir(100)surface is investigated by adsorbate-induced stress measurements and low energy electron diffraction (LEED). During the H-induced surface reconstruction from Ir(100)-(5×1)Hex to Ir(100)-(5×1)-H, a compressive stress change of -1.75 N/m is obtained. LEED spot intensities for integer and fractional order spots are measured during reconstruction, and their intensities identify the progress of the surface reconstruction during H exposure. A direct correlation between the surface stress change and the spot intensity ratio (I_{int}/I_{frac}) is established, which shows a linear dependence, suggesting that surface stress should be considered as an important factor during this reconstruction.

The stress change during formation of CoO(111) is measured during the oxidation of 2 monolayers Co. LEED identifies the c(10x2) structure of the CoO(111) film, which is under a tensile stress of $+2.1$ N/m. The magnitude of this stress can be quantitatively ascribed to the anisotropic lattice misfit between CoO(111) and Ir(100). This first stress measurement on an oxide surface suggests that Coulomb-interactions within the presumably polar CoO(111) layers do not contribute to the oxide film stress.

I

II

Zusammenfassung

Es werden Messungen zur Korrelation zwischen mechanischen Spannungen, Filmdehnungen und magnetischer Anisotropie in epitaktischen Monolagen durchgeführt. Dazu werden Spannungen während des Filmwachstums und während Magnetisierungsvorgängen direkt mit der Kristallkrümmungstechnik gemessen.

Epitaktische Fehlpassung induziert Filmspannungen in der Größenordnung von etlichen GPa während des Wachstums von Fe, Co und Ni Monolagen auf Ir(100). Spannungsmessungen identifizieren strukturelle und morphologische Veränderungen im Film. Die ersten beiden Monolagen Fe wachsen als kfz-Vorstufe für das nachfolgende Wachstum von krz-Fe auf Ir(100). Ni und Co wachsen in der kfz-Phase auf Ir(100).

Die magneto-elastischen Spannungsmessungen zeigen, dass die magneto-elastischen Kopplungskoeffizienten B_1^{eff} und B_2^{eff} stark von den entsprechenden Werten des Volumenmaterials abweichen. Diese Ergebnisse deuten an, dass Filmdehnungen erheblich für das veränderte magneto-elastische Verhalten verantwortlich sein könnten. Die Rolle dieser veränderten magneto-elastischen Kopplung für die magnetische Anisotropie wird diskutiert. Magneto-optische Kerr-Effekt (MOKE) Messungen zeigen eine leichte Magnetisierungsrichtung innerhalb der Filmebene für Fe und Co, wohingegen Ni einen Spinreorientierungsübergang zu einer leichten Magnetisierungsrichtung senkrecht zur Filmebene bei 15 Monolagen mit abnehmender Filmdicke zeigt. Diese magnetischen Ansitropien können zutreffend mithilfe der gemessenen magneto-elastischen Koeffizienten beschrieben werden.

Die Beziehung zwischen Oberflächenspannungen und Oberflächenrekonstruktion wird mit kombinierten Spannungs- und Beugungsexperimenten (LEED) am Beispiel der H-induzierten Oberflächenrekonstruktion von Ir(100)-(5×1)Hex zu (5×1)-H untersucht. Diese Änderung der Rekonstruktion geht mit einer Oberflächenspannungsänderung von -1.75 N/m einher. Während der Rekonstruktion ändert sich die relative LEED Intensität zwischen ganz-zahligen und gebrochen Reflexen, proportional zur Oberflächenspannungsänderung. Dieses Ergebnis deutet an, dass die Oberflächenspannung eine Rolle bei dieser Oberflärekonstruktion spielt.

Erstmals wird die Spannung in Oxidmonolagen gemessen. Die Bildung des gewünschten CoO(111) über die Oxidation von 2 Atomlagen Co wird mit der Beugung langsamer Elektronen (LEED) verifiziert, bis dass das Beugungsbild die Bildung der c(10x2) Struktur von CoO(111) auf Ir(100) zeigt. Diese Oxidation führt zu Zugspannungen von $+2.1$ N/m, die quantitativ mit der anisotropen Fehlpassung von CoO(111) auf Ir(100) erklärt werden. Dieses Ergebnis zeigt, dass die Coulomb-Wechselwirkung in den vermeintlich polaren CoO Lagen keinen nennenswerten Beitrag zu den Spannungen liefert.

III

IV

Contents

Chapter 1

Introduction

It has been found that the magnetic properties of thin films [1], nanodots and other low-dimensional systems can be quite different from those of bulk materials. An important property of the magnetic materials is the magnetic anisotropy energy, which is essential for fundamental research as well as for applications [2,3]. Theoretical studies [2,4] show that magnetic anisotropy is responsible for the presence of the long range magnetic order in two dimensional systems. In addition, it is a key factor that influences the application of the magnetic materials that are widely used in sensors, actuators, data storage [5] as well as permanent magnets [6]. However, in a low-dimensional system the magnetic anisotropy, e.g. the direction of magnetic easy axes, may differ from that of the bulk sample [7,8]. A well studied example is Ni on Cu(001) [9,10], which shows a spin reorientation transition from in-plane to out-of-plane, then back to in-plane depending on the film thickness.

Theoretical studies reveal that magnetic anisotropy varies dramatically as the crystal lattice experiences a distortion. Calculation on the dependence of the magnetic anisotropy on strain indicates a non-monotonical behavior [11, 12]. As the variation of magnetic anisotropy associated with strain is ascribed to magnetoelastic coupling, which is well known from the *magnetostriction* phenomena in a bulk sample, it is therefore obligatory to explore magnetoelastic coupling also in monolayer thin films in order to understand the unexpectedly complex magnetic anisotropy behavior. In thin films as well as in other strained nanostructures, magnetoelastic coupling is often determining the magnetic anisotropy. However, it has been found that the magnetoelastic coupling coefficients in these nano-scale systems deviate from the corresponding bulk values. This has been initially ascribed to a surface magnetoelastic coupling effect [13–15], which follows the idea of surface effects on magnetic moment and magnetic anisotropy. Nevertheless, it has been found that the magnetoelastic coupling coefficient in Fe films of the same thickness shows different values when the film stress is changed [16], and this contrasts with a surface effect. Later more experiments [17–20] and theoretical works [21–24] point to the importance of strain dependence of the magnetoelastic coupling coefficients. Previous experimental determination of the magnetoelastic coupling coefficients are summarized in Table 1.1. The strain-dependences of the magnetoelastic coupling coefficients have been obtained by combining film stress measurement and magnetoelastic stress measurement. However, as can be seen from Table 1.1, up to now the experimental results are rather limited, even the strain dependence of magnetoelastic coefficients such as B_2 of Ni and Co, have not been explored yet. Due to the

Table 1.1: Experimental determined strain dependent magnetoelastic coupling coefficients at room temperature from cantilever bending measurements on epitaxial films [8]. The in-plane strain ranges where the linear strain dependence is obtained are also summarized accordingly.

	B_i^{eff} (MJm^{-3})	Strain dependence	Strain range	References
Fe	B_1^{eff}	$-3.0 + 1000\epsilon$	$0 \sim 0.6\%$	[25]
		$-3.4 + 1041\epsilon$	$0 \sim 0.5\%$	[16][1]
	B_2^{eff}	$+7.5 - 360\epsilon$	$0.8\% \sim 3.1\%$	[16]
	$(3B_1^{eff} + B_2^{eff})/4$	$+0.35 + 0.22\epsilon$	$0.4\% \sim 0.8\%$	[17]
Ni	B_1^{eff}	$+9.4 - 234\epsilon$	$1\% \sim 2.5\%$	[17]
Co	B_4^{eff}	$+3.4 + 1346\epsilon$	$1\% \sim 2.0\%$	[26][2]

[1]Data are taken for Fe on different substrates and the strain is calculated from the film stress with $\tau = 208\epsilon$.

[2]The film structure is comparable to $dhcp$, therefore the reference for the constant value is not B_4^{hcp}, but rather $B_4^{dhcp} \approx 6$ MJm^{-3}.

complexity of the underlying principles, it is far from sufficient to draw a conclusion by investigating the magnetoelastic coupling in a small strain range, which might be accessible by epitaxial growth of a crystalline film on a substrate. It is also not clear whether the surface structure, such as different surface reconstructions of the substrate, may also influence the magnetoelastic coupling. To study the relation between strain and magnetoelastic coupling, all aspects such as structure, strain, and magnetoelastic coupling need to be systematically measured. In this work Fe, Co and Ni films are prepared on Ir(100), as large misfit strains are expected and rich surface reconstructions are observed on Ir(100) as well. Indeed, our experimental results indicate that strain might modify the magnetoelastic coupling substantially.

Straining a sample is one approach for measuring magnetoelastic parameters, and it has been applied to a ribbon sample [13, 27]. In amorphous alloys and metallic glasses, the magnetoelastic parameters are found to be different when external stress and strain are applied. The constraint of this method is, due to the danger of breaking the sample, the maximum strain variation is only of the order of 10^{-4}. However, the misfit induced strain in a thin film can be as large as a few percent, due to the misfit strain during deposition. Exploring epitaxial misfit strain, the advanced cantilever techniques [25, 28, 29] are employed to determine the magnetoelastic coefficients in magnetic metal films [25] as well as other magnetic materials [30].

However, more measurements are still required for better understanding of the high-order magnetoelastic coupling effects in magnetic thin films. The goal of this study is to investigate the correlation between stress, strain, structure, magnetoelastic coupling and magnetic anisotropy, and to determine the strain dependence of the magnetoelastic coupling coefficients for Fe, Ni and Co films grown on a Ir(100) substrate.

Almost all ultra thin films grown on substrates have internal stresses, which are important in determining the film growth mode as well as some other properties. Great efforts have been made to explain the mechanisms of the stresses developed during film

growth, yet because most of the growth processes are rather kinetically controlled and several factors contribute to the stress, the origin of stress is still not well understood for all cases yet. In this study, the stress change induced by epitaxial growth is measured during deposition. The relation between stress, strain and structural evolution is also discussed.

Surface stress as a specific quantity of the surface or interface plays an essential role in surface physics [31]. It builds up a link between the microscopic chemical bonding configuration and the macroscopic properties of a surface or interface. Many surface processes such as surface reconstruction, faceting and interface mixing have been shown to be strongly influenced by surface stress or companied with surface stress. Recently, it is also recognized that surface stress is an important aspect in the study of microstructures, as it can induce self-assembly or it can be induced by self-assembly [32].Hence, to study whether surface stress is the driving force of structural instabilities helps for qualitative and quantitative understanding of these microscopic and mesoscopic processes, as well as for potential technology applications such as micro-sensors and actuators. Theory models have been developed to explain surface stress effects. But due to lack of a reliable experimental method, the absolute value of surface stress cannot be measured directly at present. Indirect methods of measuring the dispersion of the surface phonons may indicate whether the surface is under tensile or compressive stress [33], but fail to describe the surface stress quantitatively. Therefore the experimental investigations on surface stress changes with high sensitive measurements provide an approach to compare model predictions with experiment [34, 35]. The cantilever technique allows high precision measurements of stress changes induced by sub-monolayer adsorbate on single crystal substrate surfaces, and this method is applied here. Experiments on surface stress are presented in this work.

This work covers the following aspects:

- Structural study on Fe, Co and Ni monolayers on Ir(100): by stress measurement and LEED studies, the thickness range for pseudomorphic growth of fcc-Fe, bcc-Fe, fcc-Co and fcc-Ni on Ir(100) is determined; our stress measurement reveals that the lattice structure of Fe on Ir(100) is bcc above 2 ML and shows a fct precursor below 2 ML.

- Magnetic properties of Fe, Co and Ni monolayers on Ir(100): MOKE measurements indicate a spin reorientation transition from out-of-plane to in-plane at about 15 ML Ni with increasing thickness; in-plane magnetization is obtained for Co and Fe monolayers.

- Experimental determination of magnetoelastic coupling coefficients for magnetic monolayers: the effective magnetoelastic coupling coefficients B_i^{eff} are obtained by magnetoelastic stress measurements, the values of B_i^{eff} differ from the bulk value; a strain dependence of B_i^{eff} is discussed.

- Relation between surface stress change and adsorption induced surface reconstruction: large compressive stress change of -1.7 N/m is measured during the H-adsorption induced surface reconstruction from Ir(100)-(5×1)Hex to (5×1)-H; in combination with *in situ* LEED measurements, a direct relation between stress change and structural change is found during the reconstruction.

- Investigations on the surface stress change induced by oxide formation: the stress change during CoO(111) formation is measured; the quantitative analysis of the induced stress change reveals that the overall stress change is determined by misfit rather than by repulsive coulomb interaction within each layer.

The thesis is organized as follows. In Chapter 2 the basic concepts and the idea for experimental determination of magnetoelastic coefficients are introduced, and the geometries of the sample needed for different ME coefficients measurement are deduced accordingly. The experimental techniques, including the two-beam optical bending beam method, LEED, MOKE are introduced in Chapter 3, and the sample preparation method is also introduced in this chapter. In Chapter 4 the experimental results are presented and summarized. The discussion of the experimental data follows in Chapter 5 and finally the conclusions are given in Chapter 6.

Chapter 2

Basic Concepts and Background

2.1   Stress at surface and interface

The concept of surface stress is developed by Gibbs [36] in his work on the thermody-
namics of surfaces, he is also the first to point out the difference between the surface
stress and surface free energy. The surface free energy γ is the excess free energy asso-
ciate with the existence of a surface and equals to the reversible work per unit area to
create a surface. The surface stress τ_{ij} can be defined as the reversible work per unit
area to stretch a pre-existing surface elastically.

The total work needed to create a surface of area A was first formulated by Shut-
tleworth [37] as

$$d(\gamma A) = A\tau_{ij}d\epsilon_{ij} \tag{2.1}$$

where ϵ_{ij} is the strain of the surface. Consequently, the surface stress can be expressed
as

$$\tau_{ij} = \frac{\partial(\gamma A)}{\partial\epsilon_{ij}} = \gamma\frac{\partial A}{\partial\epsilon_{ij}} + A\frac{\partial\gamma}{\partial\epsilon_{ij}} = \gamma\delta_{ij} + \frac{\partial\gamma}{\partial\epsilon_{ij}} \tag{2.2}$$

where δ_{ij} is the Kronecker delta. For a highly symmetric surface the surface stress is
isotropic and Equation 2.2 can be simplified as $\tau = \gamma + \partial\gamma/\partial\epsilon$. Similarly, the excess
free energy and stress can also be defined for interfaces. Different from the surface free
energy that must be positive, the surface stress can be positive "tensile" or negative
"compressive" according to whether the surface tends to contract or expand under its
own stress. A large tensile or compressive stress may cause structural instabilities such
as reconstructions at the surface.

The physical origin of the surface stress is considered to come from the surface
bonding state and the interatomic distance at the surface that are different from those
in the bulk. When a surface is created (by cleavage for example), the coordination of
the atoms at the surface is changed and the electronic charge redistribute as a response
to the missing atoms. A simple model is as shown in Figure 2.1: at a clean surface that
is created by removing the other atoms, the charge of surface atoms from bonds with
the missing atoms redistribute inwards, hence the inter-layer and intra-layer bonds of
the surface may be strengthened, and the surface lattices tend to contract. However,
the out-of-plane relaxation is free but the in-plane relaxation is restricted by the under-
layer lattice, therefore the surface shows tensile stress. This is a typical scenario for
transition metal and noble metal surfaces [38]. If there is chemical adsorption on the
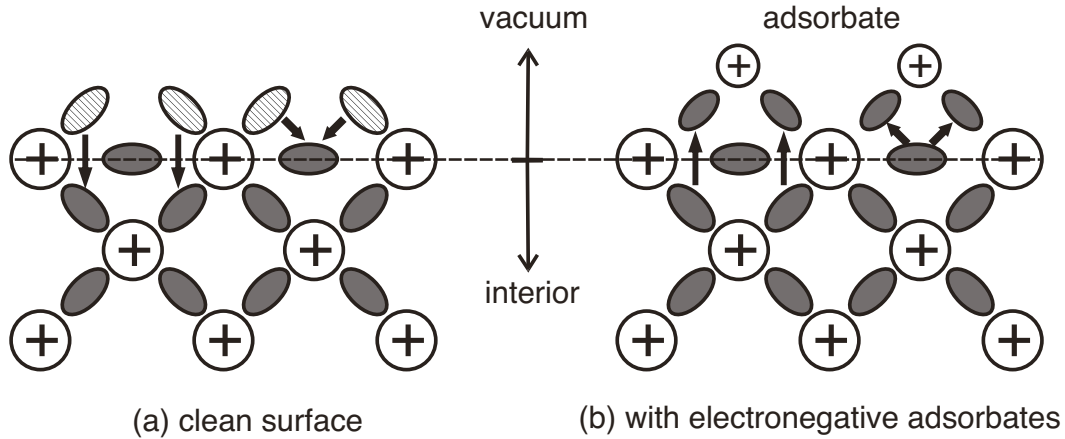
Figure 2.1: Illustration of a simple model of charge redistribution to explain (a) tensile stress at clean metal surface and (b) a compressive stress caused by electronegative adsorbate, adapted from Ref. [38]

surface, the surface bonding is changed and the tensile stress of the clean surface will be reduced in this simple picture. With electronegative adsorbates, the bond charge should be removed to the adsorbate atoms and the intra-layer bonding is impaired so that the tensile stress is reduced, or even changed into compressive stress. Despite of its simplicity, this model is in agreement with many experimental results [39, 40] for adsorbate covered surfaces.

Till nowadays, the quantitative studies of surface free energy and surface stress mainly come from calculations at zero Kelvin, as the experimental methods to measure the surface free energy at room temperature or the absolute value of surface stresses for clean crystal surfaces is rather deficient. Fortunately, the changes of surface stress due to adsorbates can be experimentally determined through high sensitivity measurements with optical, capacity and tunnel current deflection methods.

For recent reviews of surface free energy and surface stress the readers are referred to the papers of Ibach [38], Cammarata [41], Sander and Ibach [42], Haiss [31].

2.2 Stress and strain in epitaxial monolayers

Epitaxial monolayers on a substrate are very often constrained laterally by the substrate lattices, which will result in a stress in the films. Compressive (negative) or tensile (positive) stresses may be induced as is shown in Figure 2.2. Consequently, a sample bending may be observed for a thin substrate and it can be exploited for determining the stresses in the films (as will be introduced in Section 3.1).

The stresses in thin films can be ascribed to extrinsic and intrinsic origins. Extrinsic stresses are caused by external forces or change in ambient conditions such as temperature and magnetic field. Thermal stresses and magnetoelastic stress are two types of extrinsic stresses. Thermal stresses arises from the temperature alternation when the film and the substrate have different coefficients of thermal expansion, which is well understood and can be calculated without difficulty. The magnetoelastic stress appears if the magnetization state is changed, for example, by an externally applied magnetic field. It depends on the magnetoelastic coupling in the material, therefore it can be
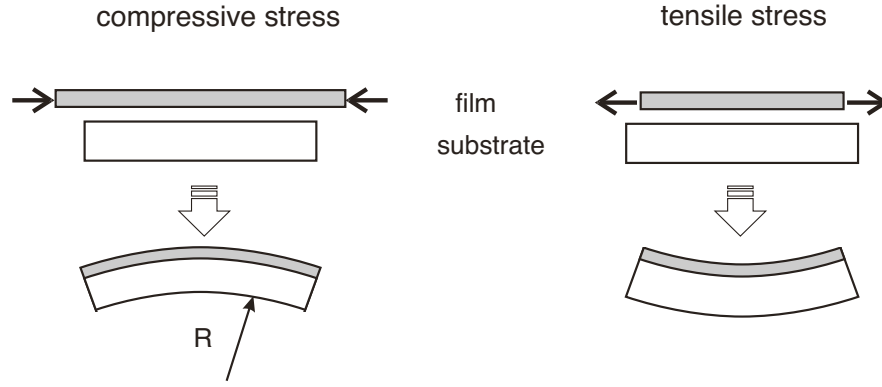
Figure 2.2: Illustration of compressive stress and tensile stress in the thin films, and the induced bending for a thin substrate.

applied for experimental determination of magnetoelastic coupling coefficients of the film, as will be introduced in Section 2.4. The intrinsic stresses, on the contrary, are developed during the formation of the films, including coherency stresses and growth stresses. The coherency stresses, which are also called mismatch induced stress, exist in epitaxial films because the in-plane lattice spacing of the film is constrained by the substrate and is different from its lattice spacing in the bulk. The growth stresses (sometimes are called intrinsic stresses [41]) are developed during film growth on a substrate.

To associate with this work, three cases that are normally related with thickness regimes are introduced separately in the following: the submonolayer range before a continuous layer is developed, the pseudomorphic growth range and beyond pseudomorphic growth.

a. Submonolayer: surface stress effect

At the very beginning of the growth, a new interface between the substrate s and the thin film f is formed. Three surfaces are involved: the surface of the substrate $\tau_s^{(s)}$, the newly created interface $\tau_{f-s}^{(i)}$ and the surface of the thin film $\tau_f^{(s)}$. The observed sample bending is not caused by the film stress alone but also a combination of surface stresses and interface stress as $\tau_f^{(s)} + \tau_{f-s}^{(i)} - \tau_s^{(s)}$.

b. Pseudomorphic growth

The term "pseudomorphic growth" refers to a situation in which the overlayer material adopts a crystal structure and lattice constant that matches to the underlying substrate coherently [43]. The unit mesh of the film is forced to match the lattice constants of the substrate that are different from those of the equilibrium state. When the lattice constant of the substrate is larger than the lattice constants of the film material in the bulk, the film tends to contract and causes a tensile stress in the film; conversely, if the lattice constant of the substrate is relatively small the film lattice tends to expand and causes a compressive stress. In this case, the misfit induced stress (coherency stress) is the dominant stress in the thin film and can be calculated from the misfit between the film and the substrate:
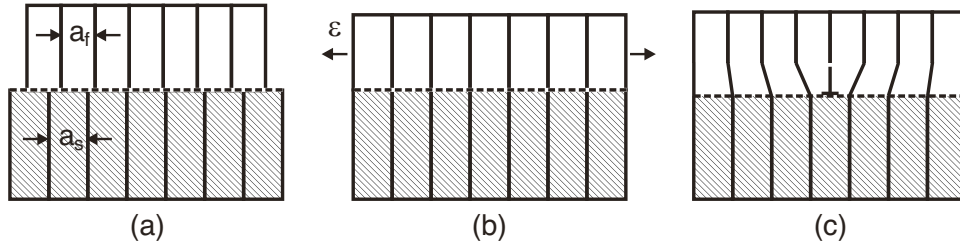
Figure 2.3: Sketch of (a) ideal non-interacting film and substrate with different lattice parameters, (b) elastically strained film to match the substrate lattice, and (c) relaxed by misfit dislocations in the film.

$$\tau = \frac{Y}{1-\nu}\eta, \qquad \eta = \frac{a_{sub} - a_{equ}}{a_{equ}}.$$

Here a_{sub} is the in-plane lattice spacing of the substrate that is adopted by the film, a_{equ} is the lattice spacing in the bulk of the film in a equilibrium state. Y and ν are the Young's modulus and Poisson's ratio of the film respectively, $(1-\nu)$ describes the biaxial nature of the stress.

The first few deposited monolayers are normally confined strongly by the substrate lattice within pseudomorphic growth, but it is also possible that the film does not take the dimensions of the substrate, and hence no pseudomorphic growth occurs.

c. Beyond pseudomorphic growth

As the pseudomorphic growth continues with more film material being deposited, the elastic energy in the film accumulates until a critical thickness is reached [44] when dislocations are more energetically favorable for strain relief. Above this thickness, the energy to introduce dislocations is less than the elastic energy being released. Figure 2.3 (c) shows a simplified sketch of a dislocation formed at the interface. For more details about the complete dislocations, partial dislocations and defects that are associated with the misfit strain the readers are referred to the works by Frank and van der Merwe [44, 45], Matthews and Blakeslee [46, 47].

Experiments [48] show that even if the film growth starts from a two dimensional layer-by-layer growth mode, later three dimensional islands will be formed as the film thickness increases. The stresses during this kind of film growth are no more as straight-forwardly analyzed as the misfit induced stress, here the mechanisms may be attributed to the island growth, islands coalescence, dislocations and so on. Both compressive stress and tensile stress can be produced during these processes, therefore one should be careful when interpreting the stress curves in this situation. As these stress relaxation mechanisms hold true for epitaxial monolayers, it is beneficial to combine the stress measurement with the structure detecting methods–e.g. STM and LEED, so that a clearer picture maybe achieved. For example, in this study it is found that during the epitaxial growth of Fe monolayers on Ir(100), the stress is relaxed after the pseudomorphic growth ($\sim$10 ML), and extra diffraction spots stem from dislocation network are observed in LEED images, hence it is reasonable to believe that the dislocation forma-

tion causes the stress relaxation after pseudomorphic growth, which is also indicated by STM images (see Section 4.1 and Section 5.1.1).

2.3 Magnetic anisotropy in thin films

In ferromagnetic materials, the direction of spontaneous magnetization is not isotropic but has one or several energetically preferred axes, and the term "magnetic anisotropy" is used to describe this phenomenon. Although the magnetic anisotropy energy is in the order of $\sim \mu\text{eV/atom}$ and much smaller comparing to the exchange energy of $10\text{-}10^3$ meV/atom, it is essentially important for both fundamental and application point of view. Especially for two-dimensional systems such as thin films, the magnetic anisotropy energy is crucial in explaining the ferromagnetic order at non-zero temperature, it is also much larger than in the bulk and it is of great interest for applications using magnetic layers. For example, the magnetic anisotropy energy for bulk Ni is $\sim 0.2~\mu\text{eV/atom}$, and it is $\sim 30~\mu\text{eV}$ in the Ni films on Cu(100) substrate [49], which is about two orders of magnitude larger.

The physical origin [50] of magnetic anisotropy can be attributed to dipole-dipole interaction and the spin-orbit coupling. Dipole-dipole interaction is responsible for shape anisotropy , and spin-orbit coupling is the origin of many other type of magnetic anisotropies such as magneto-crystalline anisotropy and magnetoelastic anisotropy.

Shape anisotropy originates from the long-range magnetic dipolar interaction. It is determined by both the magnetization and the shape of the sample. The shape anisotropy per unit volume for a perfectly flat film is

$$f_{shape} = -\frac{1}{2}\mu_0 M_s^2 \cos^2\theta \tag{2.3}$$

in which θ is the angle of the magnetization with respect to the film normal. It is a main energy contribution to the magnetic anisotropy, which prefers an in-plane magnetization direction in thin films. According to Bruno, in a real film the roughness will also cause a small dipolar surface anisotropy that favors an out-of-plane magnetization direction, but it is shown to be a very small effect [51].

Magnetocrystalline anisotropy in highly symmetric crystal is a very small contribution as the orbital moment is quenched. The magnetocrystalline energy in cubic crystals is expressed as

$$f_{MC} = K_1(\alpha_1^2\alpha_2^2 + \alpha_2^2\alpha_3^2 + \alpha_3^2\alpha_1^2) + K_2\alpha_1^2\alpha_2^2\alpha_3^2 \tag{2.4}$$

in which K_i is the magnetocrystalline anisotropy constant, α_i is the direction cosine of the magnetization with respect to the crystalline axis

In a strained system, the spin-orbit coupling is modified, and this modification in the magnetic anisotropy is called magnetoelastic anisotropy. The epitaxial thin films are normally strained due to the mismatch between the substrate and the lattice constants of the film material in its equilibrium state. Under this situation, the magnetoelastic anisotropy is not negligible. The magnetoelastic anisotropy will be specifically introduced in the next section.

The total magnetic anisotropy f_{MA} consists of all the contributions from both dipole-dipole interaction origin and the spin-orbit coupling origin. A quantitative description

Table 2.1: Magneto-crystalline anisotropy f_{MC} and magnetoelastic anisotropy f_{ME}, calculated for an isotropic in-plane film strain $\epsilon_{\parallel}$ for various epitaxial orientations, adapted from Ref. [52].

	f_{MC}	f_{ME}
Cubic(100), in-plane, $f([100]) - f([110])$	$-\frac{1}{4}K_1$	0
Cubic(100), out-of-plane, $f([100]) - f([001])$	0	$B_1\left(\frac{c_{11}+2c_{12}}{c_{11}}\epsilon_{\parallel}\right)$
Cubic(110), in-plane, $f([001]) - f([\bar{1}10])$	$-\frac{1}{4}K_1$	$(B_1 - B_2)\left(\frac{c_{11}+2c_{12}}{c_{11}+c_{12}+2c_{44}}\epsilon_{\parallel}\right)$
Cubic(110), out-of-plane, $f([\bar{1}10] - f([110])$	0	$2B_2\left(\frac{c_{11}+2c_{12}}{c_{11}+c_{12}+2c_{44}}\epsilon_{\parallel}\right)$
Cubic(111), in-plane, all directions	0	0
Cubic(111), out-of-plane, $f[-\frac{1}{\sqrt{2}}, \frac{1}{\sqrt{2}}, 0] - f[111]$	$-\frac{1}{12}K_1$	$2B_2\left(\frac{c_{11}+2c_{12}-2c_{44}}{c_{11}+2_c12+4c_{44}}\epsilon_{\parallel}\right)$

of the magnetic anisotropy can be expressed as

$$f_{MA} = f_{MC} + f_{shape} + f_{ME} \tag{2.5}$$

where the surface and interface anisotropy are included in different terms. In this work we concentrated on the magnetic properties of Fe, Co and Ni films, and the expressions for the magneto-crystalline and the magnetoelastic energy for in-plane and out-of-plane anisotropies are shown in Table 2.1. The magnitude of the constants related with different magnetic anisotropy terms for Fe, Co and Ni are presented in Table 2.2 for comparison.

2.4   Magnetoelastic coupling and the measurement

According to Kittel [55], the magnetoelastic coupling energy arises from the interaction between the magnetization and the mechanical strain of the lattice, which is responsible for the strain-dependent magnetic properties. For cubic system, the standard expression of magnetoelastic energy is [55, 56]

$$f_{ME}^{cubic} = B_1(\epsilon_1\alpha_1^2 + \epsilon_2\alpha_2^2 + \epsilon_3\alpha_3^2) + 2B_2(\epsilon_4\alpha_2\alpha_3 + \epsilon_5\alpha_3\alpha_1 + \epsilon_6\alpha_1\alpha_2) + \cdots \tag{2.6}$$

where α_i is the direction cosine of the magnetization with respect to the cubic axes and ϵ_i is the strain measured along the cubic axes. B_1 and B_2 are the so called magnetoelastic coupling coefficients. As the internal energy density must be invariant with respect to the time reversal, therefore the expression is even with respect to the direction cosines α_i, in terms of 0th, 2nd, 4th... order of α_i. Higher order (≥ 4) terms of α_i are not included but can be found in Ref. [57, 58]. For clarity, higher order terms of strain ϵ_i are not shown here. However, we will show in this study, that in a thin film with considerable strain, the higher order strain terms are not negligible, which will be discussed in Chapter 5.

In a zero-strain system, the magnetoelastic energy is also zero. As has been discussed in the previous sections, the mismatch strain exists in all the epitaixal films that have a

Table 2.2: Saturation magnetization, shape anisotropy for out-of-plane magnetization in thin films $(-\frac{1}{2}\mu_0 M_s^2)$, magnetic crystalline anisotropy constants K_i and magnetoelastic coefficients B_i in bulk elements bcc Fe, hcp Co and fcc Ni [53,54].

	unit	bcc Fe	hcp Co	fcc Ni
saturation magnetization	μ_B	2.216	1.715	0.616
$-\frac{1}{2}\mu_0 M_s^2$	MJ/m^3	1.85	1.32	0.15
	meV/atom	0.13	0.09	0.01
K_1	MJ/m^3	0.048	0.513	-0.006
	meV/atom	0.0035	0.035	-0.0004
K_2	MJ/m^3	0.0001	0.143	-0.00247
	meV/atom	0.00007	0.00007	-0.0002
B_1	MJ/m^3	-3.43	-8.1	9.38
	meV/atom	-0.25	-0.55	0.62
B_2	MJ/m^3	7.83	29.0	10
	meV/atom	0.57	1.97	0.67

different lattice constant as in the substrate, and some other factors will also influence the film strain during growth. The magnetoelastic constants of bulk Fe, Co and Ni are orders of magnitude larger than the magnetocrystalline anisotropy constants K_i, therefore even a small film strain will cause a considerable magnetoelastic anisotropy. As a converse process, the change of magnetization direction will induce a strain change in the sample. Figure 2.4 shows the comparison of magnetoelastic coupling in bulk sample and in a thin film. In a bulk magnetic sample, the volume and dimension changes when the sample is magnetized along a certain direction, which is called *magnetostriction*. The magnetostrictive strains λ are of the order 10^{-4} for transition metals, and the relation between magnetoelastic coefficients B_1, B_2 and the magnetostriction constants λ_{100}, λ_{111} is [50,55]

$$\lambda_{100} = -\frac{2}{3}\frac{B_1}{(c_{11} - c_{12})} \quad \text{and} \quad \lambda_{111} = -\frac{1}{3}\frac{B_2}{c_{44}}. \tag{2.7}$$

In thin films, the lateral lattice is constrained by the substrate that is not able to expand or contract freely, only the out-of-plane lattice spacing is free to change. In this case, the magnetoelastic coupling will induce a stress in the thin film and a bending of the sample will result, as indicated in Figure 2.4.

The total energy density that depends on the strain and magnetization directions is given by magneto-crystalline anisotropy f_{mc}, magnetoelastic energy f_{me} and the elastic energy f_{el}:

$$f = f_{mc} + f_{me} + f_{el} \tag{2.8}$$

For a cubic system, the elastic energy can be expressed as

$$f_{elastic}^{cubic} = \frac{1}{2}c_{11}\left(\epsilon_1^2 + \epsilon_2^2 + \epsilon_3^2\right) + c_{12}\left(\epsilon_1\epsilon_2 + \epsilon_2\epsilon_3 + \epsilon_1\epsilon_3\right) + \frac{1}{2}c_{44}\left(\epsilon_4^2 + \epsilon_5^2 + \epsilon_6^2\right) \tag{2.9}$$

In accordance with the stress induced by elastic strain, the magnetoelastic stress equals the strain derivative of the magnetoelastic energy. When the crystal is magne-
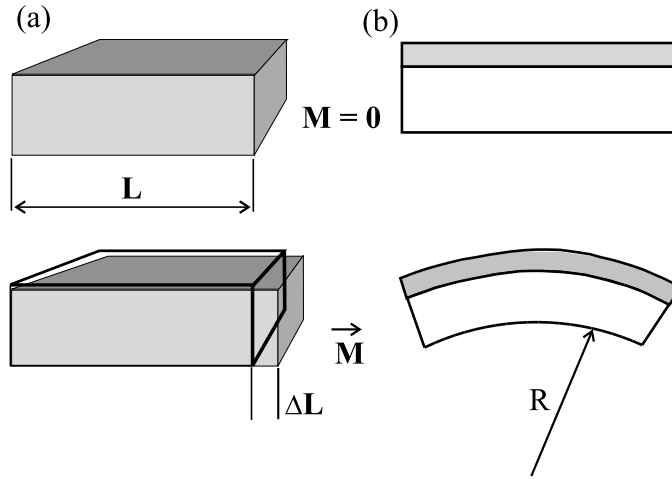
Figure 2.4: The magnetoelastic coupling in (a) a bulk sample and (b) in a magnetic thin films on a substrate from Ref. [25]. (a) The magnetoelastic coupling induces a magnetostrictive strain $\Delta L/L$ in bulk samples. (b) The bonding to the substrate induces a magnetostrictive stress that induces a bending of the filmsubstrate compound.

tized in the direction α, the strain in the equilibrium state can be obtained by minimizing the total energy density f. The magnetoelastic stress will affect the dimensions of the sample until the equilibrium state is realized. In a bulk sample, during the magnetization process the magnetoelastic stress will cause a deformation of the dimensions to minimize the total energy and results in the magnetostrictive strain. While in the epitaxial thin films that are constrained laterally by the substrate, the sample cannot expand or shrink freely in the plane, the magnetoelastic stress in the magnetized films can cause a measurable bending of the whole sample, if the substrate is sufficiently thin. This will be explained in Section 3.1.

The idea of our experiments for magnetoelastic coupling coefficients B_i is to measure the magnetoelastic coupling induced stress in well defined magnetization states, and correlate the stress change with the respective magnetoelastic coupling coefficients B_i. Taking a cubic crystal for example, when its magnetization is aligned along [100] axis, we have $\alpha_1 = 1$, $\alpha_2 = 0$ and $\alpha_3 = 0$; when magnetized along [010] axis, $\alpha_1 = 0$, $\alpha_2 = 1$ and $\alpha_0 = 0$. Consequently, B_1 can be obtained from the stress change as the magnetization direction is switched in-plane from [100] to [010] direction:

$$\Delta\tau = \tau_1^{M\|100} - \tau_1^{M\|010} = \frac{\partial f(M\|100)}{\partial \epsilon_1} - \frac{\partial f(M\|010)}{\partial \epsilon_1} = B_1 \qquad (2.10)$$

From the analysis above, we find the way to measure the value of B_1 is to orient the cantilever sample in such a way that the length of the sample is parallel to [100] direction of the film and the width is along the [010] direction. By switching the magnetization direction from along the length to the along the width with external magnetic field, B_1 is directly given by the stress difference between the two states.

When the sample is not oriented to coincide with the crystal axes, a strain tensor transformation is necessary to obtain the corresponding stress-strain relation. Here we consider the case when the in-plane coordination of a (001) film is rotated 45° from the crystal axes (as shown in Figure 2.5 (c)). The crystal axes direction x, y, z are
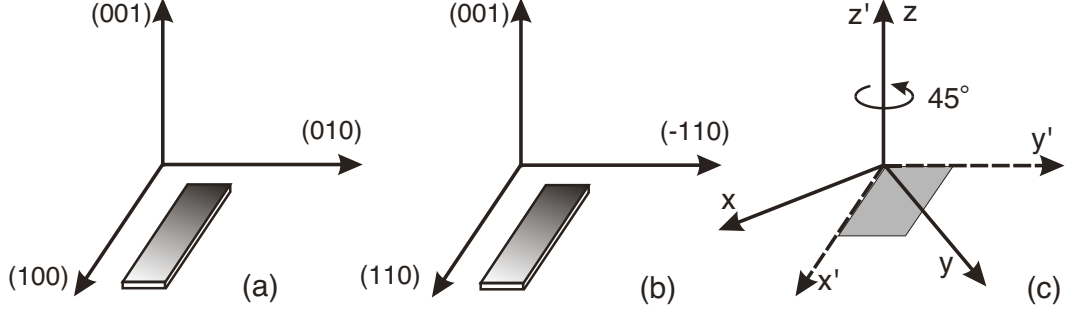
Figure 2.5: Geometry of magnetoelastic coupling coefficients measurement in this work. (a) Length and width of the sample parallel to the (100) and (010) directions of the crystal axes in the film, for B_1 measurement. (b)The length and width of the sample is parallel to (110) and ($\bar{1}$10) of the crystal axis, for B_2 measurement. (c) (100) and (010) directions of the crystal axes are rotated from along the length and width of the sample by 45°.

expressed as the film direction x′, y′ and z′ with the transformation matrix a:

$$
\begin{array}{c|ccc}
 & \text{x} & \text{y} & \text{z} \\
\hline
x' & \frac{\sqrt{2}}{2} & \frac{\sqrt{2}}{2} & 0 \\
y' & \frac{\sqrt{2}}{2} & -\frac{\sqrt{2}}{2} & 0 \\
z' & 0 & 0 & 1
\end{array}
\qquad
a = \begin{pmatrix} \frac{\sqrt{2}}{2} & \frac{\sqrt{2}}{2} & 0 \\ \frac{\sqrt{2}}{2} & -\frac{\sqrt{2}}{2} & 0 \\ 0 & 0 & 1 \end{pmatrix}
$$

The transformed strain tensor is obtained as

$$
\epsilon = a^T \epsilon' a = \begin{pmatrix} \frac{1}{2}(\epsilon_1' + \epsilon_2') & \frac{1}{2}(\epsilon_1' - \epsilon_2') & 0 \\ \frac{1}{2}(\epsilon_1' - \epsilon_2') & \frac{1}{2}(\epsilon_1' + \epsilon_2') & 0 \\ 0 & 0 & \epsilon_3' \end{pmatrix}
$$

The values of ϵ in Equation 2.6 are expressed in terms of ϵ'. When the magnetization is along the length and width of the sample, the values of α_i are:

$$
M\|110 : \alpha_1 = \tfrac{\sqrt{2}}{2}, \alpha_2 = \tfrac{\sqrt{2}}{2}, \alpha_3 = 0;
$$
$$
M\|\bar{1}10 : \alpha_1 = -\tfrac{\sqrt{2}}{2}, \alpha_2 = \tfrac{\sqrt{2}}{2}, \alpha_3 = 0.
$$

Similar to Equation 2.10, we obtained the respective stress change $\Delta\tau'$:

$$
\Delta\tau' = \frac{\partial f(M\|110)}{\partial \epsilon'} - \frac{\partial f(M\|\bar{1}10)}{\partial \epsilon'} = B_2. \tag{2.11}
$$

Chapter 3

Experimental Techniques

Stress measurements using optical bending beam method can be applied for UHV system as well as in air. However, the magnetic properties of ultra thin films are better to be measured *in-situ* as deposited, as the magnetic properties can be sensitive to the surface conditions. The surface changes such as adsorption or desorption processes can only be studied in a UHV environment. Hence the measurements are all performed in a UHV system, the relative techniques and the UHV apparatus are introduced in this chapter.

3.1 Optical bending beam method

The stress measurements in this work are carried out using the optical bending beam method based on the cantilever technique. The idea of stress measurement using cantilever bending originates from the pioneering work by Stoney [59], who related the curvature of the sample with film stress. Today the advanced techniques measure the curvature of the sample by detecting the capacitance [28] or the optical deflection [60,61], which greatly increased the sensitivity so that small surface stress changes can also be measured. Similar optical method have been successfully employed in surface stress and film stress measurements for Si samples [62,63].

The principle of the technique is shown in Figure 3.1(b). The rectangular thin substrate is clamped along its width at the upper end and free at the lower end. It is used as a cantilever that will bend when its front side and backside endure different forces or stresses. A laser beam is used to detect the deflection of the cantilever sample. The laser beam is split in two beams that are aligned to point at the sample surface with a short separation in between. Subsequently, the beams reflected from the surface are detected by two separated position-sensitive detectors with photo current amplifier that transform the positions of the beams into voltages. The position changes (Δd) of the two laser beams on the detectors are transferred into the slope changes Δm on the sample surface where they are reflected:

$$\Delta m = \frac{\Delta d}{2L}$$

in which L is the distance between the sample and the detector. The curvature of the substrate $\kappa = 1/R$ can be obtained from the slope differences and the separation

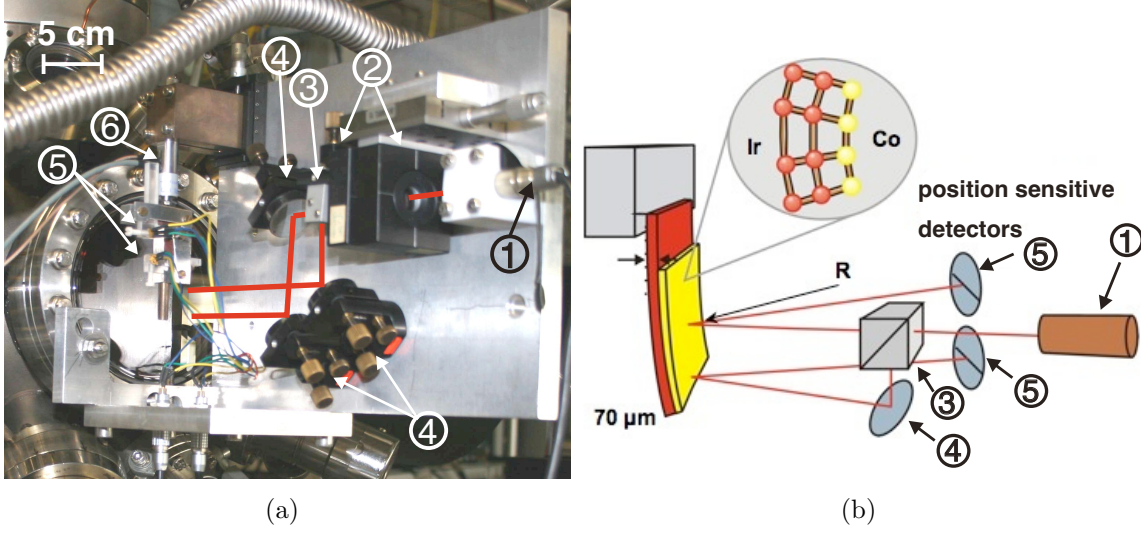(a)   (b)

Figure 3.1: Setup of the optical bending beam method: (a) photo of the optical plate fixed to a UHV-window flange: 1- laser diode, 2-focus lens, 3-beam splitter, 4-mirrors, 5- position sensitive detectors, 6-piezo for calibration.(b) Sketch of the principle of the stress measurement from [64].

between two laser spots (Δl) on the surface in a good approximation.

$$\Delta\kappa = \Delta(\frac{1}{R}) = \frac{\Delta m_2 - \Delta m_1}{\Delta l} \tag{3.1}$$

For a rectangular cantilever sample with appropriate length-to-width ratio (no less than 1.5), the bending of the substrate can be taken as a free two-dimensional bending case [65]. The expressions for biaxial film stresses in terms of radii of the curvatures along the width and length of the sample follow as [25]

$$\tau_x = \frac{Y_S t_S^2}{6(1-\nu_S^2)}(\frac{1}{R_x} + \nu_S \frac{1}{R_y}) \quad \text{and} \quad \tau_y = \frac{Y_S t_S^2}{6(1-\nu_S^2)}(\frac{1}{R_y} + \nu_S \frac{1}{R_x}). \tag{3.2}$$

In principle, the two stresses τ_s and τ_y are to be determined, and normally the curvature change along the length of the sample is measured for a rectangular cantilever sample. However, if the stress is isotropic, there is $\tau_x = \tau_y = \tau$, and the stress τ can be calculated using the so called modified Stoney equation according to the curvature $\frac{1}{R}$

$$\tau = \frac{Y_S}{(1-\nu_S)}\frac{t_S^2}{6R} \tag{3.3}$$

where t_S is the thickness of the substrate, Y_S and ν_S are the Young's modulus and Poisson ratio of the substrate. With the optical bending beam method, the curvature change can be obtained, and the stress change is calculated from Equation 3.3 as

$$\Delta\tau = \frac{Y_S t_S^2}{6(1-\nu_S)}\Delta\frac{1}{R} \tag{3.4}$$

When the stress is changed by film deposition, the total stress change is an integral of film stress τ_F throughout the film thickness t_F, i.e. $\Delta\tau = \Delta(\tau_F t_F)$.
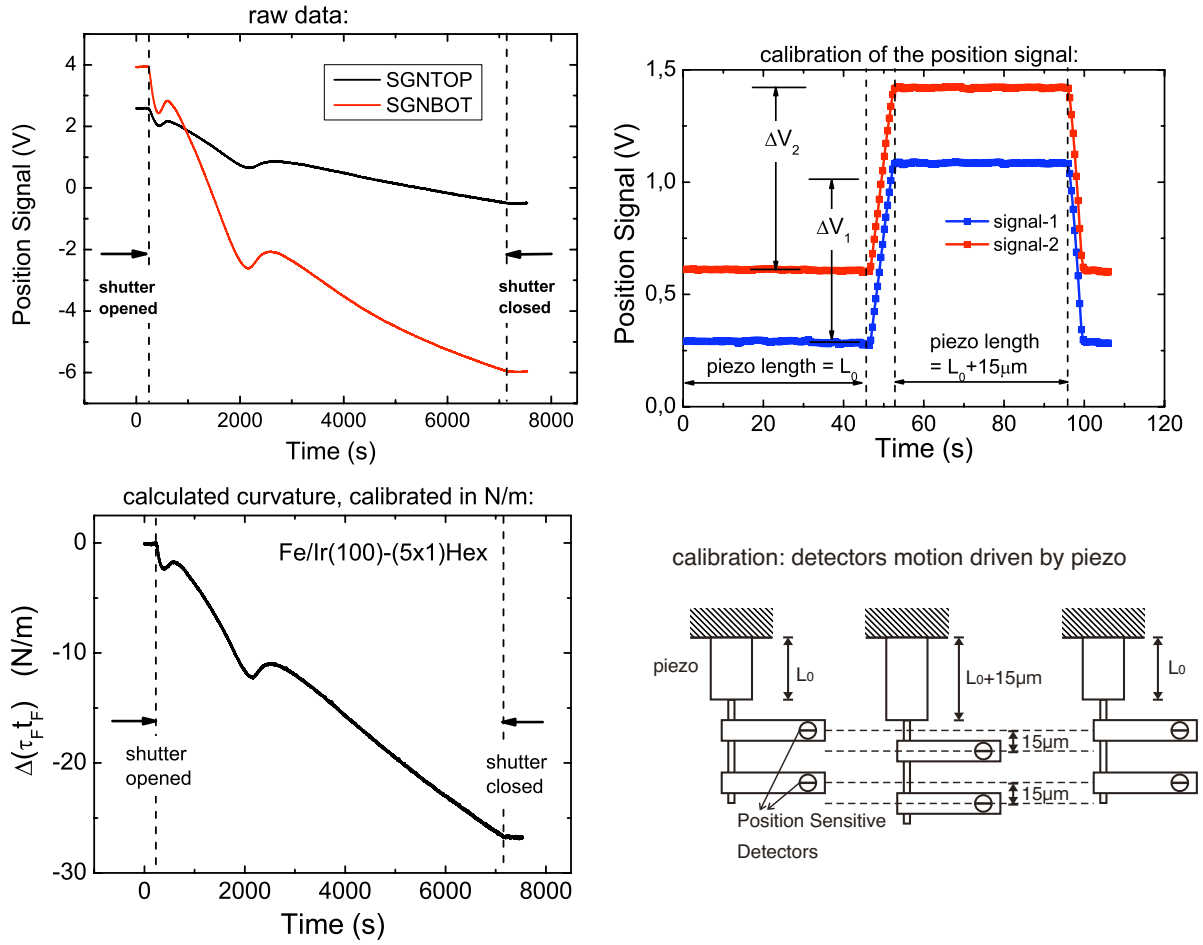
Figure 3.2: The position signals from the detectors during epitaxial growth of Fe mono-layers on Ir(100)-(5×1)Hex. Two detectors are illuminated by the laser beams and reflected from the upper (SGNTOP) and lower (SGNBOT) part of the sample surface. The relation between signal voltage and the deflection of the beam —calibration factor— is obtained using a piezo translation of the detectors.

The two optical beam bending method takes advantages of [66]: (a) direct curvature measurement with high precision, and (b) enhanced signal-to-noise ratio by eliminating the common noise of the two signals with a difference measurement. An example of a stress measurement during deposition is shown in Figure 3.2. The position signal obtained from two position sensitive detectors are transformed into deflections of the sample at two positions, and the curvature change of the sample is calculated from the deflections using Equation 3.1. Finally the stress change is obtained according to the curvature change.

The mismatch between the epitaxial film and the substrate induces a stress in the order of GPa that corresponds to a curvature change of several $(km)^{-1}$. But the magne-toelastic coupling induced stress change is two orders of magnitude smaller which makes it more demanding to be measured. The two optical beam bending method is used in this work to measure the magnetoelastic coupling induced stress change in the magnetic monolayers of Fe, Co and Ni on Ir(100) substrate (as illustrated in Figure 3.3(a)). The sample is put into magnetic fields (Figure 3.4) that can force the magnetization to be
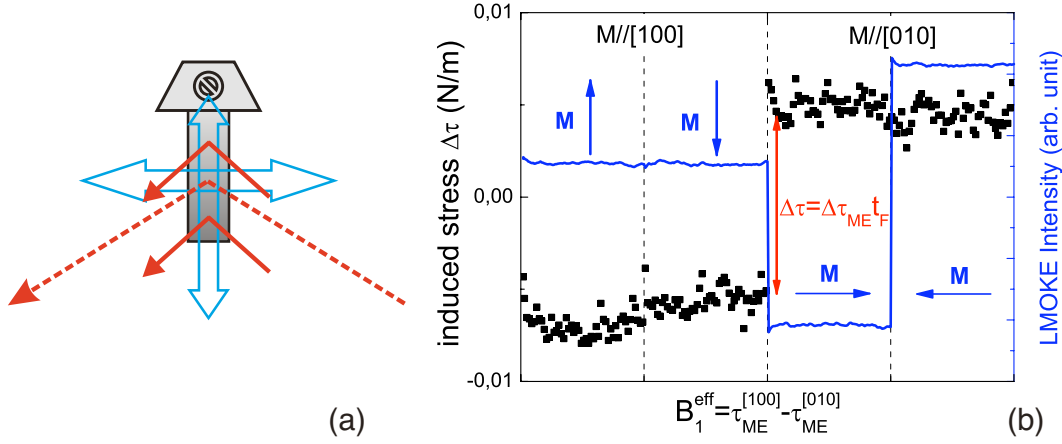
Figure 3.3: Illustration of the magnetoelastic stress measurement. (a) Setup of the magneto-elastic stress measurement: the horizontal and vertical magnetic field (blue volume arrows) are applied by two external magnets, the incident and reflected laser beams for MOKE (red dash line) and stress measurement (red solid line) are also shown. (b) Magneto-elastic coupling induced stress change for 8 ML Fe on Ir(100)-(1×1) when magnetization is switched in-plane from along the Fe(100)-[100] to [010]. The MOKE signal is monitored during the stress measurement to ensure that the magnetization is in full remanence during this magnetization reversal.

saturated along the magnetic field direction. Magnetoelasitic stress is measured as the magnetization is aligned along horizontal and vertical directions, alternatively. The stress difference gives the value of the magnetoelastic coupling coefficients B_i according to the relative coordination of the crystal axes and the external field, as has been introduced in Sec. 2.4. In order to minimize the influence of a large magnetic field on the movement of the UHV manipulator, the magnetic field is firstly applied to saturate the magnetization and then reduced to a smaller field where full remanence still remains, as verified by MOKE, and then the stress measurement is performed in this magnetization state. An example is given in Figure 3.3(b). Unlike the stress induced by epitaxial growth, which is isotropic in the plane, the magnetoelastic stress results in an anticlastic curvature [67] if the magnetization is saturated along one direction. The expression of magnetoelastic stress in terms of radii of the curvature is

$$\tau_{me}t_F = \frac{Y_S}{(1+\nu_S)}\frac{t_S^2}{6R}.$$ (3.5)

According to Equation 2.10 and 2.11, the expression for B_1 and B_2 as a function of the curvature change is:

$$B_1 = \tau_{M\|100} - \tau_{M\|010} = \frac{Y_St_S^2}{6(1+\nu_S)t_F}\left((\frac{1}{R})_{M\|100} - (\frac{1}{R})_{M\|010}\right)$$ (3.6)

$$B_2 = \tau_{M\|110} - \tau_{M\|\bar{1}10} = \frac{Y_St_S^2}{6(1+\nu_S)t_F}\left((\frac{1}{R})_{M\|110} - (\frac{1}{R})_{M\|\bar{1}10}\right)$$ (3.7)

In this study we take single crystalline Ir(100) as a substrate. To measure both B_1 and B_2 of Fe, Co and Ni films, two Ir(100) crystals are used as substrates: one of the

Table 3.1: Elastic properties of the elements involved in this work from Ref. [68]. Young's modulus Y and Poisson's ratio ν can be calculated from the elastic constants c_{ij} with $Y = (c_{11} + 2c_{12})(c_{11} - c_{12})/(c_{11} + c_{12})$ and $\nu = c_{12}/(c_{11} + c_{12})$. The values of c_{ij} and Y are given in GPa.

Element	c_{11}	c_{12}	c_{44}	Y	ν
fcc Ir	600	270	260	500	0.299
bcc Fe	229	134	115	131	0.37
fcc Fe	200	134	77	92	0.401
fcc Ni	249	152	118	133	0.38
fcc Co	242	160	128	114	0.40

sample is cut with its length and width along Ir(100)-[110] and [$\bar{1}$10] axes respectively, the other along Ir(100)-[100] and [010]. The dimension of the substrate is 10mm×3mm. To obtain a desired high sensitivity, the substrate thickness is about $100\mu m$. The values for the elastic properties for Ir(100) and the ferromagnetic elements we explored are given in Table 3.1.

3.2 The ultra high vacuum (UHV) system

The experiments are performed in a UHV apparatus with a base pressure of 4×10^{-11} mbar. The sketch of the UHV system is shown in Figure 3.4. The system can be separated into two chambers with a gate valve. Surface analysis and magnetic properties are measured in-situ in the upper and lower chamber, respectively. Sample preparation and surface analysis are carried out in the upper chamber, which is equipped with LEED (low energy electron diffraction), AES (Auger election spectroscopy) a QMS (quadrupole mass spectrometry) and an ion gun. The lower chamber is equipped with a MOKE setup with magnets which can produce a field of up to 0.4 T along the horizontal and polar direction, and 0.1 T along the vertical direction. The sample is fixed to a vertical manipulator with X-Y freedom and can be lowered into the magnetism chamber. As has been introduced in the Section 3.1, the two laser beam deflection optics are fixed to the windows on the apparatus. They are mounted on both upper and lower chambers. During deposition or adsorption process the stress change is measured *in-situ* and magneto-strictive stress is measured together with the magnetic field and MOKE in the lower chamber .

The temperature of the sample can be raised to more than 1200°C by e-beam heating from the backside of the sample. In order to protect the special cantilever sample as well as to heat the sample more evenly, an iridium shield is put between the sample and the filament. The shield is heated by accelerated electrons directly, and the radiation from the shield heats the sample. To avoid a deformation of the sample, one should not keep the sample at very high temperature for too long, therefore the high temperature annealing is finished in just a few seconds. The sample can be also cooled down with a liquid-nitrogen (LN$_2$) reservoir attached to the manipulator, which is connected to the upper end of the sample. The sample temperature is measured by a K-type thermo-
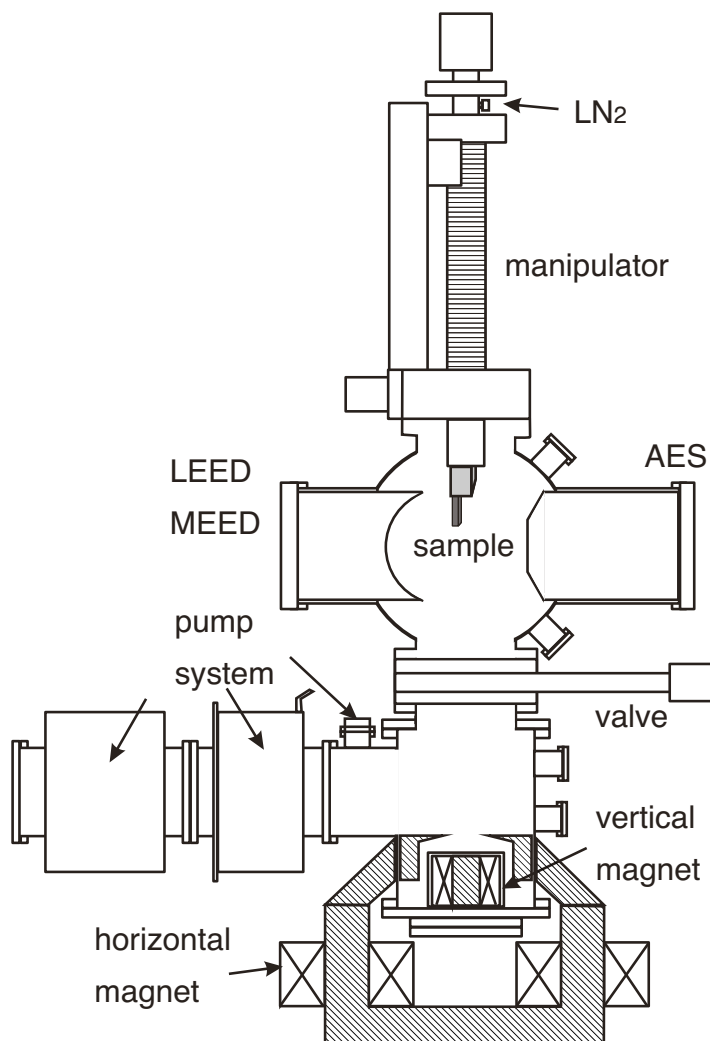
Figure 3.4: Sketch of the UHV apparatus. The sample-preparation and surface charac-
terization chamber can be separated from the lower chamber with a gate valve. Mag-
netic properties are measured in-situ in the lower part.

couple fixed on the manipulator close to the sample.

For the purpose of adsorption experiment, various gas tanks are directly connected to
the upper chamber through leak valves. During adsorption and desorption procedures,
the pressure is of the order of 5×10^{-10} mbar. Both the reading from the ion gauge
and the thermocouple can be collected by a PC simultaneously, which is important for
monitoring the pressure and the temperature during the adsorption experiments.

As shown in Figure 3.4, the magnetic field is supplied by two electromagnets: the
vertical magnet is fixed to the concave bottom of the lower chamber ; the horizontal mag-
net is embedded on a rotatable platform out of the chamber and with a corresponding
rotatable yoke inside the UHV-chamber, and the magnetic field can be applied parallel
or perpendicular to the sample surface by turning the outside magnet and the inside
yoke together.

In the following the other two main experimental techniques employed in this work,
LEED and MOKE, are introduced briefly, with examples from our experimental results.
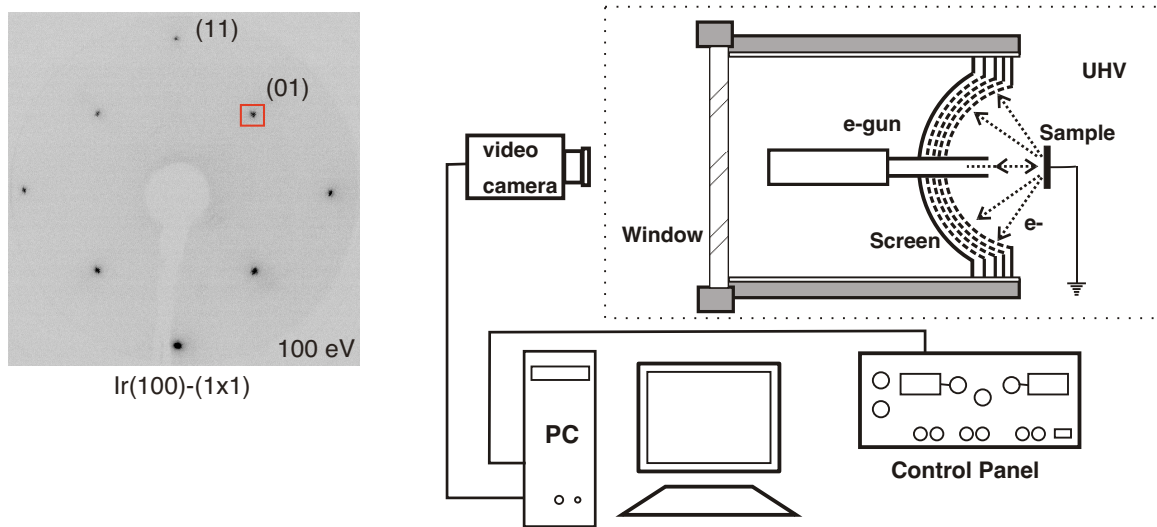
Figure 3.5: Sketch of LEED-I(V) measurement. The electron voltage is controlled by software via the control panel and the images of diffraction patterns are captured by a video camera then transfered to PC. Intensity of the diffraction spot is recorded versus the incident electron energy. (LEED-I(V) spectra of (01) diffraction spots for Ir(100)-(1×1) is shown in page 27.)

Low Energy Electron Diffraction(LEED)

Wavelengths of electrons with an energy between about 10 eV and 400 eV is comparable with the lattice constants of crystals, and the penetration depth is about 5-10Å, which results in a high surface sensitivity.

Figure 3.5 shows the sketch of LEED measurement in this lab. In addition to the LEED patterns, the intensity spectra of the diffraction spots–i.e., LEED-I(V) spectra– can also be obtained with a commercial package–AIDA2000/specs. A desired beam spot in the LEED pattern is chosen firstly, and the spot intensity is recorded when the energy of the incident electron beam is changed under the control of a computer. The LEED-I(V) spectra of the same surface may vary slightly for different systems, however the main features remain the same and give a finger print to identify a certain surface. As will be presented in Section 3.3, the LEED-I(V) spectra of the (01) spot is taken to distinguish different surface reconstructions on Ir(100).

Due to the nature of the low energy electrons, surface crystallography using LEED requires complex theoretical descriptions considering the strong electron-ion-core scattering and the multi-scattering procedure. Nevertheless, the vertical lattice spacing of the surface layers can be extracted from a quantitative analysis of LEED-I(V) spectra of the (00) beam. As shown in Figure 3.6(a), the sample is rotated to deviate from normal to the incident electron beam by a small angle θ. Tuning the incident electron energy to fullfill the Bragg condition (Equation 3.8), the intensity of the specular beam will reach a maximum for:

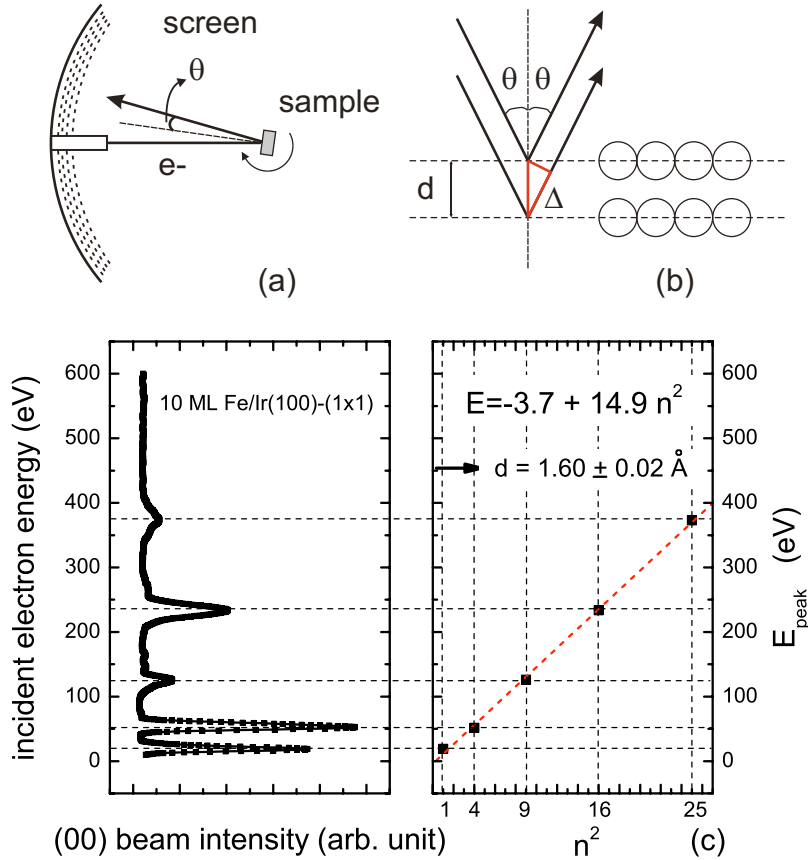$$2d \cos \theta = n\lambda \qquad (n = 1, 2, 3, \cdots) \tag{3.8}$$

Figure 3.6: Illustration of how to extract interlayer lattice spacing from LEED-I(V) spectra. (a) The sample is rotated a small angle θ from normal to the incident electron beam; (b) intensity maxima of (00) beam fulfills Bragg reflection condition; (c) example of lattice spacing measurement on 10 ML Fe on Ir(100)-(1×1): I(V) spectra of (00) beam and linear fitting of $E_{peak} \sim n^2$ relation.

Thus the interlayer lattice spacing d can be obtained by fitting the relation between electron energy E and the interference order n (Figure 3.6(c)). Note that when the electrons penetrate into the surface layers, their kinetic energy is modified by the internal potential of the material V. As a result, the wavelength of the incident electron is changed to $\lambda(\text{Å}) = \sqrt{\frac{150.4}{(E-V)(\text{eV})}}$ [69]. Consequently, the electron energy corresponds to the maximum intensity should fulfill the following

$$E_{peak} - V = \frac{150.4}{4d^2 \cos^2\theta} n^2 \qquad (n = 1, 2, 3, \cdots)$$

By fitting the linear relation between E_{peak} and n^2, the slope can be obtained, and it gives the value of lattice spacing d accordingly.

Figure 3.6(c) shows the lattice spacing measurement for 10 ML Fe on Ir(100)-(1×1) by the LEED-I(V) method, the linear fitting of $E_{peak} \sim n^2$ relation indicates that the averaged lattice spacing is 1.6 ± 0.02 Å. The results are discussed in Section 5.1.1.
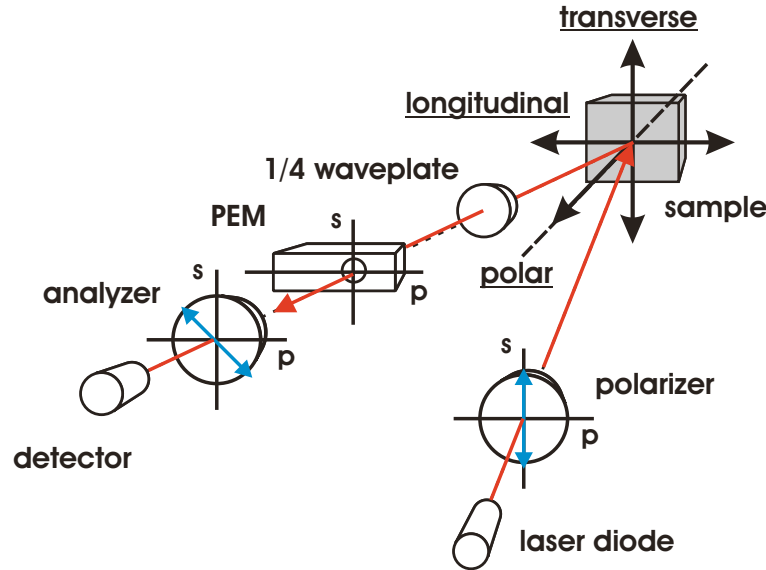
Figure 3.7: Sketch of the MOKE measurement. Longitudinal, transverse and polar geometry of MOKE measurement are shown. Polarization directions of the polarizer (s-polarization) and analyzer (45° to s-polarization) respective to the scattering plane are indicated as blue arrow that show typical angle of longitudinal and polar MOKE measurement. (Settings for transversal MOKE measurement are described in the text.)

Magneto-Optical Kerr Effect (MOKE)

The magnetic properties of the magnetic monolayers grown on Ir(100) are investigated by the magneto-optical Kerr effect (MOKE) [70, 71] *in-situ*. Despite of the difficulty in obtaining absolute value of magnetization, this method has been successively applied for the measurement of magnetization hysteresis loops for thin films. What the MOKE measures is the magneto-optical response. It has been found that the polarization state of the light is changed when reflected from a surface of magnetic material. The polarization state change includes both in-phase component (Kerr rotation) and out-of-phase components (Kerr ellipticity). The origin of the magneto-optic effect is ascribed to the antisymmetric parts of the dielectric tensor of a medium in a macroscopic picture based on dielectric theory. Microscopically, the electric field of the propagating light couples with the electron spin in the medium through spin-orbital interaction.

The diagram of an AC-MOKE measurement is schematically shown in Figure 3.7. Three conventional magneto-optic configurations (longitudinal, transverse and polar MOKE) are defined according to the respective direction of the magnetization to the scattering plane. The magnetization direction and especially the magnetic anisotropy of the magnetic films can be studied along three axes by analyzing the hysteresis loops obtained from measurements with three MOKE geometries. For longitudinal and polar MOKE measurements, the incident beam is s-polarized by a polarizer and the analyzer is set away by 45° from s-polarization direction. The reflected beam passes through a PEM (photoelastic modulator) to measure Kerr rotation (at twice the fundamental frequency) and Kerr ellipticity (at fundamental frequency) with the same geometry. The 1/4 wave-plate is used to compensate the birefringence of the UHV window and the ellipticity of the metallic reflection on the substrate. According to the dielectric
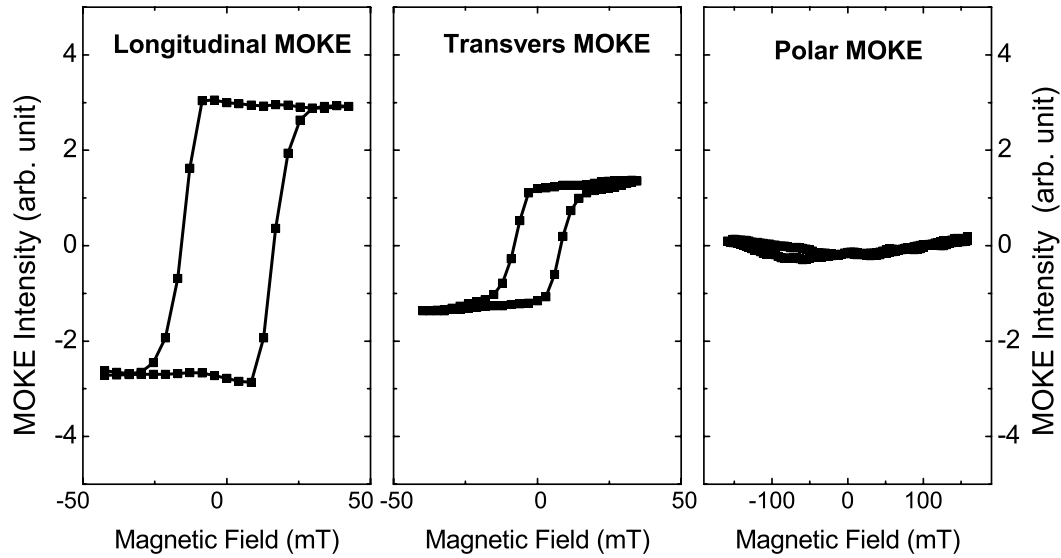
Figure 3.8: MOKE measurements for 19 ML Fe on Ir(100)-(5×1)H with longitudinal, transverse and polar geometry.

theory [72], with transverse MOKE geometry the vector product of magnetization and the electric field of the incident light is zero, therefore no change in the polarization state of the light can be detected. Here, the intensity of the reflected light depends on the magnetization of the sample. To measure transverse MOKE, the polarizer is set away by 45° from the s-polarization direction. The major axis of the PEM and the analyzer are also rotated 45° accordingly and the 1/4 wave-plate can be removed. Figure 3.8 presents the typical MOKE curves showing an in-plane easy magnetization axis. With longitudinal MOKE and transverse MOKE, the square-like hysteresis loops for in-plane magnetization are obtained that correspond to the easy axes of the magnetization. Along polar direction, which is a hard axis, the magnetization can not be aligned with the external field due to the large magnetic anisotropy.
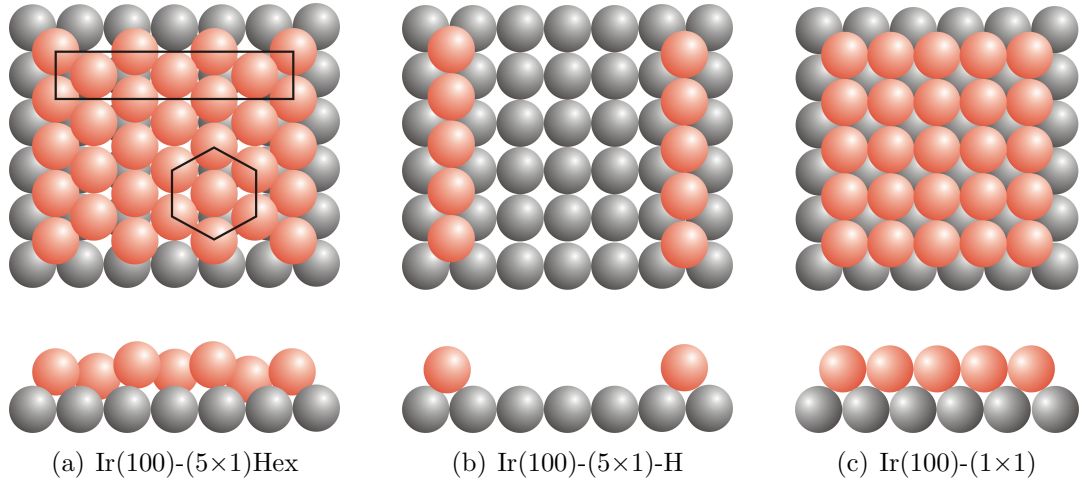
(a) Ir(100)-(5×1)Hex   (b) Ir(100)-(5×1)-H   (c) Ir(100)-(1×1)

Figure 3.9: Hard sphere model of different Ir(100) surface reconstructions according to the STM studies from the literature [74, 75]

3.3   Preparation of Ir(100) surface reconstructions

The Ir(100) surface can be prepared with three reconstructions (Figure 3.9): Ir(100)-(5×1)Hex, Ir(100)-(5×1)-H and Ir(100)-(1×1). The Ir(100)-(5×1)Hex surface is a quasi-hexagonal structure with 20% more atoms in the topmost layer compared to the bulk [73]. With hydrogen adsorption, the 20% extra atoms in the surface layer of Ir(100)-(5×1)Hex can be lifted and form long mono-atomic rows on the top. STM images [74] reveal that between the atomic rows the under layer is rearranged to a bulk-like structure. The metastable Ir(100)-(1×1) phase can also be obtained from Ir(100)-(5×1)Hex as will be introduced below. In the STM images [75] it shows large patches of (1×1) islands accommodated on bulk-like rearranged layers.

To prepare different Ir(100) surface reconstructions, we took the recipe provided by the Erlangen group [74, 75] as a reference and modified it according to our special cantilever sample.

Firstly the Ir(100) surface is cleaned by Ar ion sputtering (HV=3 kV, I_e=20 mA, $I_{sample} \approx 1~\mu$A) at room temperature. After sputtering the sample is quickly heated to about 1100°C in an O_2 atmosphere (5×10^{-6} mbar) and kept in the O_2 atmosphere for another 5 minutes until a fully oxidized layer is formed. The O(2×1+1×2) [76] LEED pattern as shown in Figure 3.10 is taken as an indication of a successful oxidation process. Contaminations, such as carbon, are removed in this way. Finally, the sample is flashed to 1200°C and the Ir(100)-(5×1)Hex reconstruction is obtained. Offering H_2 to the Ir(100)-(5×1)Hex reconstructed surface at room temperature, the Ir(100)-(5×1)-H can be obtained above the critical exposure (approximately 4 Langmuir, see Section 4.3, page 45.) After the oxidation procedure as described above, if the sample is annealed at 120°C in H_2 atmosphere (2×10^{-7} mbar) for 5 minutes, the Ir(100)-(1×1) surface reconstruction can be obtained.

The LEED patterns of different Ir(100) surface reconstructions are shown in Figure 3.11. Typical Ir(100)-(5×1)Hex and Ir(100)-(5×1)-H reconstructions appear in two mutually orthogonal domains. Furthermore, the different Ir(100) surface reconstruc-
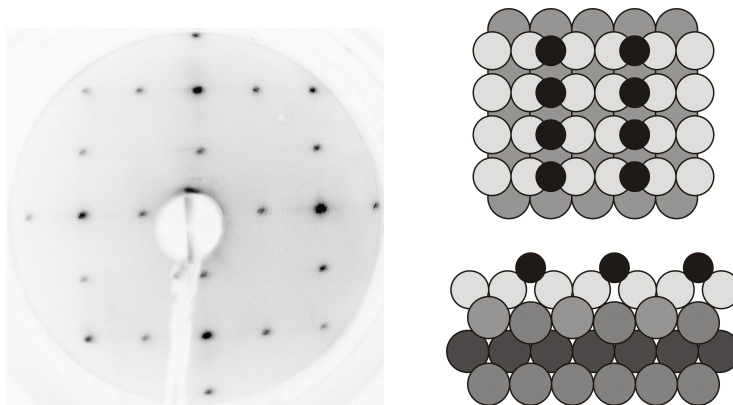
Figure 3.10: LEED pattern of O(2×1+1×2) reconstruction at 100 eV obtained after oxidation of Ir(100) in this lab. The solid-ball model of Ir{100}-(2×1)-O from [76] .

tions can also be identified by their typical I(V) curves. As shown in Figure 3.11(d), the LEED intensity of the (10) spot shows different features when the electron energy is changed. For example, the I(V) curve of Ir(100)-(5×1)Hex surface shows a single peak at about 150eV while there are four continuous peaks in the I(V) curve of Ir(100)-(5×1)-H. The difference between the I(V) curve of Ir(100)-(5×1)-H and Ir(100)-(1×1) is not so drastic although the LEED patterns are quite different for the two reconstructions, the main difference is the observations of peaks around 300eV, the 1×1 reconstructions show two clear peaks with the similar height while for (5×1)-H reconstruction the first peak is more predominant and the latter peak is much lower in intensity.

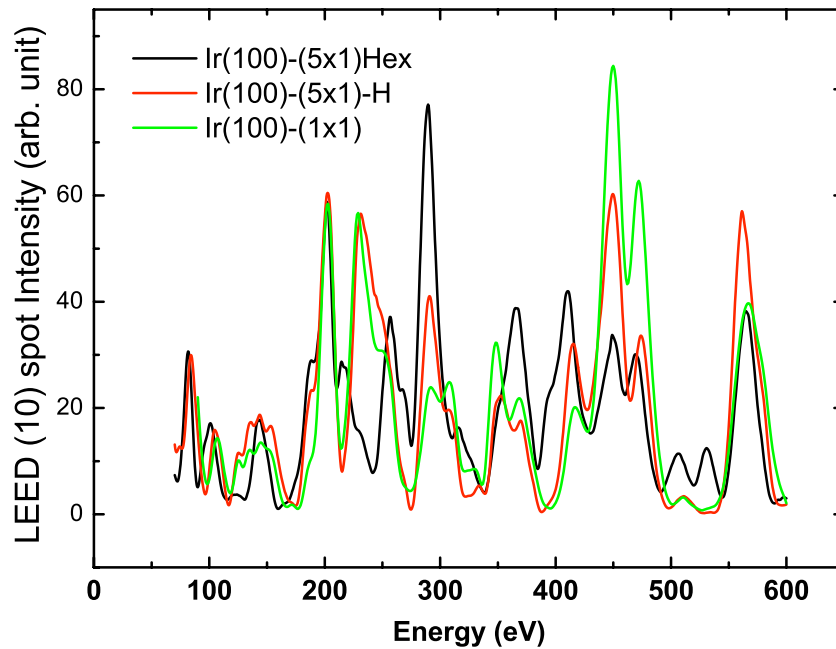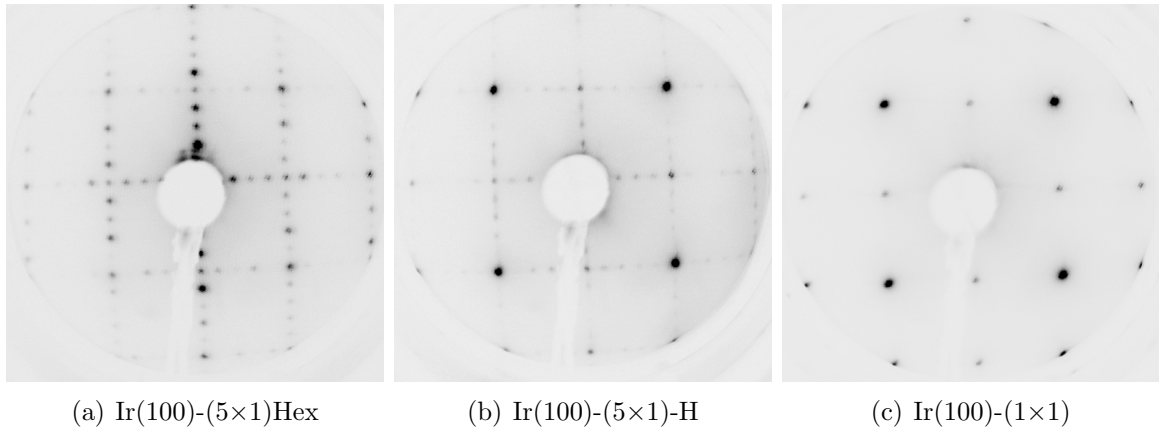(a) Ir(100)-(5×1)Hex   (b) Ir(100)-(5×1)-H   (c) Ir(100)-(1×1)

Figure 3.11: LEED patterns of different Ir(100) surface reconstructions at 180 eV(a)-(c) and comparison of the (10) LEED spot spectra of different Ir(100) surface reconstructions. The difference between these patterns are apparent: the patterns for Ir(100)-(5×1)Hex and Ir(100)-(5×1)-H exhibit superspots/fractional spots originating from (5×1+1×5) reconstructions. The fractional spots in the pattern for the quasi-hexagonal surface are isolated from each other, each individual spot is clearly separated from the one next to it. While for (5×1)-H surface, there are stripes between the fractional spots that connect them with the neighboring spots. There are no fractional spots in the LEED pattern for the (1×1) surface.

ex

Chapter 4

Experimental Results

The main experimental results of this work are presented in this chapter. For the sake of clarity, the results are divided into four parts. In the first section the film stress and the structural properties for Fe, Co and Ni monolayers on Ir(100) are introduced respectively. The magnetic properties and also the results of the magnetoelastic coupling measurements for these thin films are shown in the second section. The last two sections describe the studies of the surface stress change with respect to the structural change of the Ir(100) surface. The results for hydrogen induced surface reconstruction from Ir(100)-(5×1)Hex to Ir(100)-(5×1)-H are given in the third section, and the results for oxidation of 2 ML Co on Ir(100) to give CoO(111) are presented in the last section.

4.1 Film stress and structure of ferromagnetic monolayers on Ir(100)

Prior to the measurements, the Ir(100) substrate is cleaned and treated to show the desired surface reconstruction following the procedures introduced in Section 3.3. The monolayers of Fe, Co and Ni are deposited at room temperature ($\sim$300 K). The film thickness is calibrated with MEED oscillations. To study the film stress evolution during epitaxial growth, the stress change is measured using the optical bending beam method, and LEED measurements are performed before and after growth to study the structure of the substrate and film, respectively.

Film stress and structure of Fe on Ir

The stress change induced by epitaxial growth of Fe films on Ir(100)-(1×1) is shown in Figure 4.1(a). In the submonolayer range ($t_F < 0.8$ ML), a compressive stress change ($\Delta\tau < 0$) of ~ -1 N/m is induced. As has been introduced in Section 2.2, the stress change in the submonolayer range is dominated by the change of the surface stress. During deposition of the second monolayer, a tensile stress change ($\Delta(\tau_F t_F) > 0$) is induced, and the stress curve shows a positive slope up to +7 GPa. At 2 ML, a clear kink shows up in the stress curve, after which the stress change switches to compressive instantly with a large negative slope of up to -10 GPa. Subsequently, the linear-like stress curve between 2 ML and 10 ML exhibits nearly constant slope indicating that the Fe monolayers are uniformly strained layer by layer. Around 10 ML, the stress
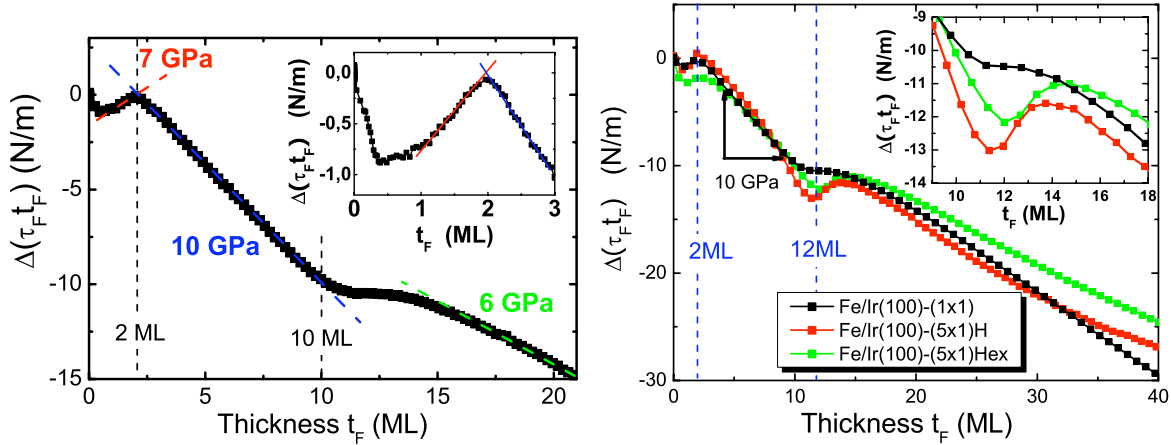
Figure 4.1: Stress measurement during deposition of Fe monolayers on Ir(100)-(1×1). Comparison of stress curves for Fe monolayers on different Ir(100) surface reconstructions. The dashed lines are to help to see the slope of the curves.

curve deviates gradually from the almost straight curve as shown in Figure 4.1(a), and another kink is observed ranging from 12 ML to 15 ML. Above 15 ML, the slope of the stress curve is about −6 GPa, much less than what is obtained between 2 ML and 10 ML.

To investigate the influence of different Ir(100) surface reconstructions on the film stress of epitaxial Fe monolayers, the stress measurements are also carried out for Fe films grown on Ir(100)-(5×1)Hex and Ir(100)-(5×1)-H surfaces. Comparison of the stress curves are shown in Figure 4.1. Except for the initial compressive surface stress change in the submonolayer range, all the three curves exhibit clear kinks at 2 ML and 12 ML∼15 ML that divide the film growth into 3 stages. The slope of the stress curves changes from positive to negative before and after the appearance of the kink at 2 ML. Large compressive stress changes are observed for the film thickness ranging from 2 ML to 10 ML then the stress is relaxed after the kink between 12 ML and 15 ML. No full stress relaxation—i.e., slope of the stress curve goes to zero—is observed even when the film thickness is as large as 6 nm. By comparing the film stress we obtained with the expected mismatch-induced film stress for fcc-Fe and bcc-Fe on Ir(100), it is suggested that when the thickness is less than 2 ML a fcc-Fe lattice is formed, and then pseudomorphic growth of bcc-Fe lasts from 2 ML to 10 ML. A quantitative analysis and discussions are given in Section 5.1.1 on page 52.

LEED measurements are taken before and after the Fe films are prepared. As shown in Figure 4.2, for $t_F < 10$ ML, the patterns are similar to that of the clean Ir(100)-(1×1) and the diffraction spots are clear and sharp. With increasing film thickness extra satellite-spots start to appear around the original spots. Notice that at the same thickness the stress curve starts to deviate from the constant slope (between 2∼10 ML) and shows a kink subsequently. The fine structure of the diffraction spots can be clearly seen from the (00) spot when the sample is rotated a small angle (e.g., 8 degree) away from normal to the incident electron beam with an electron energy of 20 eV. Figure 4.2(g)+(h) show merged satellite spots around the (00) spot. The satellite spots may originate from the extra periodic atom arrangement along [110] directions
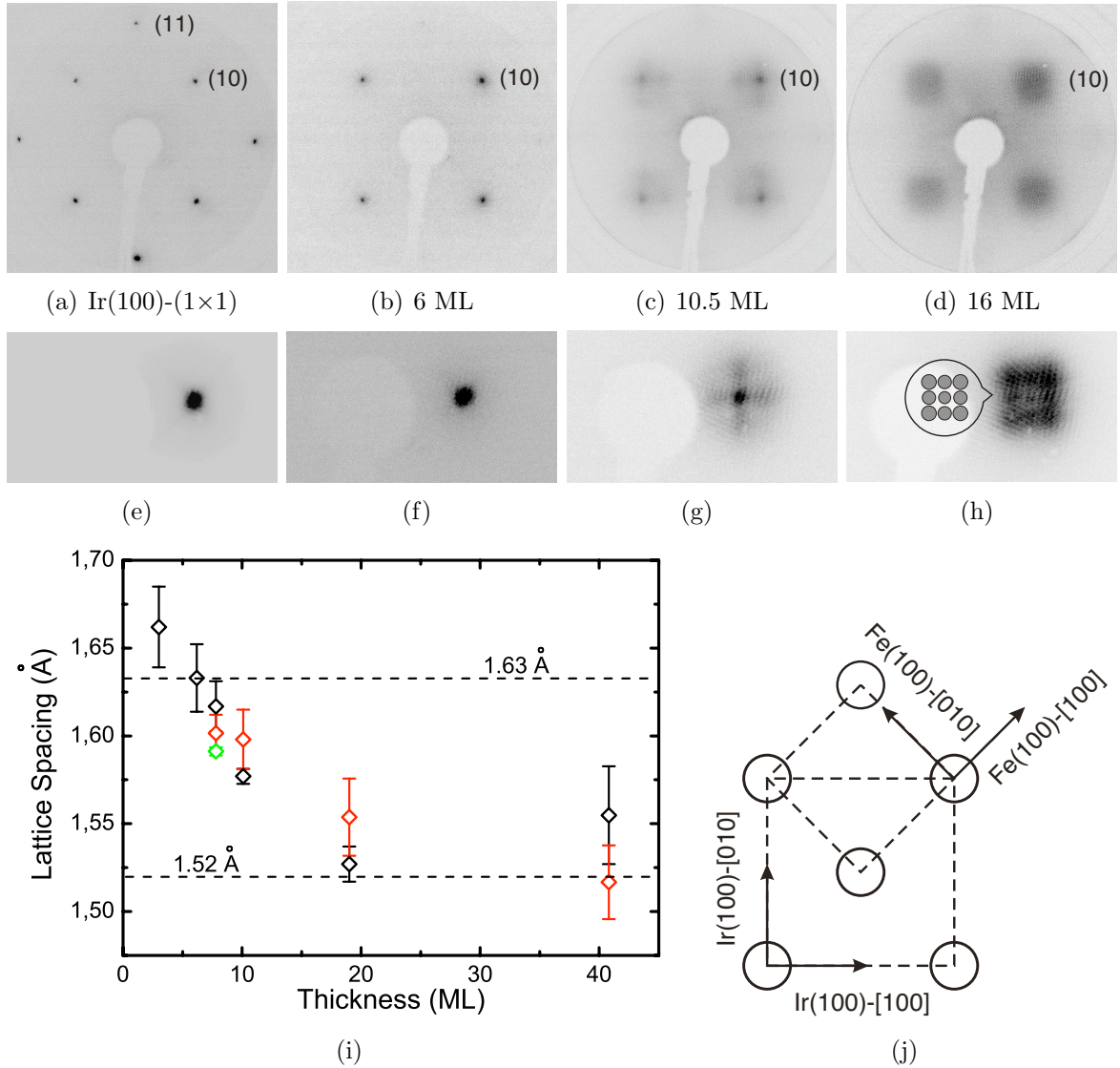
(a) Ir(100)-(1×1)   (b) 6 ML   (c) 10.5 ML   (d) 16 ML

(e)   (f)   (g)   (h)

(i)   (j)

Figure 4.2: Selection of LEED patterns of Fe monolayers grown on the Ir(100)-(1×1) substrate with increasing film thickness. Patterns (a)-(d) are taken at 98 eV, the corresponding figures of the (00) spot (e)-(h) are taken at 20 eV and the incident electron beam deviate from surface normal with a small angle of 8 degrees. (i) Lattice spacing of Fe/Ir(100) for different film thickness obtained from LEED-I(V) of (00) beam spot, and the calculated lattice spacing of elastically strained fcc-Fe ($\sim$1.63Å) and bcc-Fe($\sim$1.52Å) are indicated by the horizontal dashed lines. The geometry of the bcc-Fe(100) lattice on Ir(100) is illustrated in (j) for understanding the LEED patterns (see text).

of Fe(100) surface (that is also the [100] directions of Ir(100)), and the periods varies as the spots are weak. For 16 ML Fe (Figure 4.2(h)), there are more satellite spots around the original spots, and the satellite spots become more clear and concentrated, suggesting that the atomic rearrangements beside the original lattice are more periodic and obvious. These periodic atomic rearrangements are not only along [100] of Fe(100) but also along the [110] directions, and the periods are around 5-6 atomic distances comparing the two diffraction patterns shown in Figure 4.2(d) and 4.2(h).
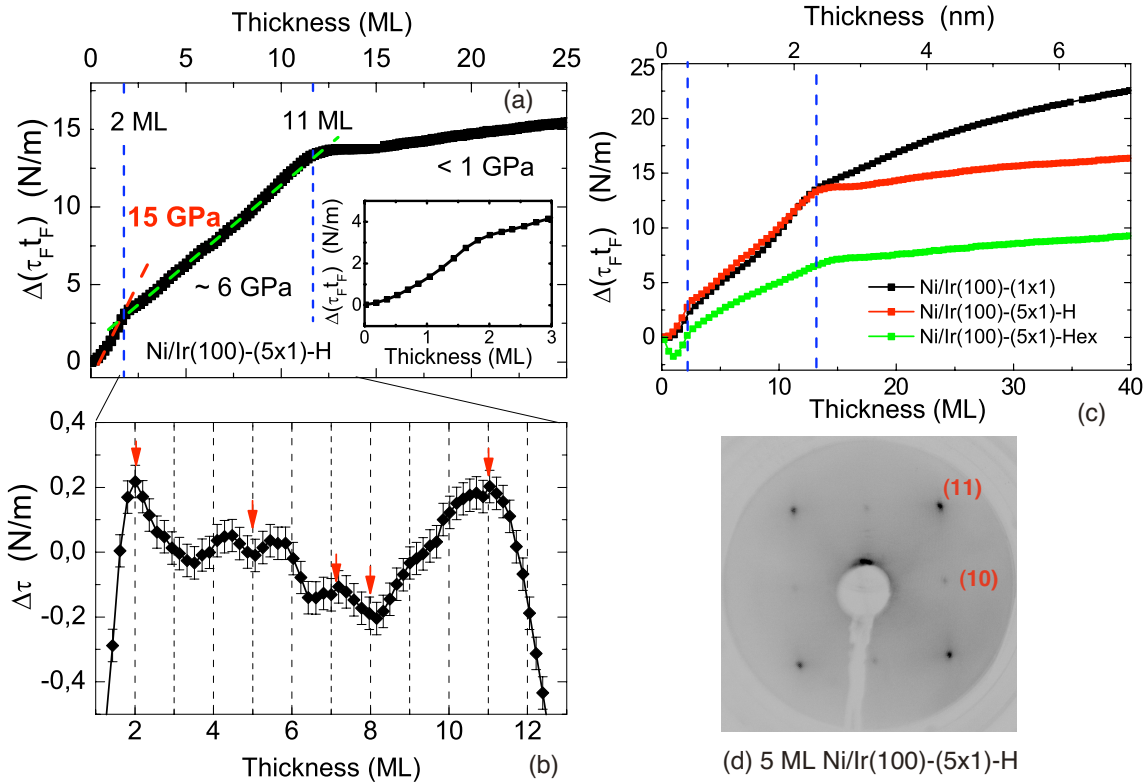
Figure 4.3: Stress change induced by deposition of Ni monolayers on Ir(100)-(5×1)-H surface(a). (b)The stress curve shows slight modulations from 2 ML to 12 ML. (c)Comparison of induced stress change of Ni monolayers on different Ir(100) surface reconstructions. (d) LEED image for 5 ML Ni grown on Ir(100)-(5×1)-H taken at 150 eV

The perpendicular lattice spacing of Fe monolayers on Ir(100)-(1×1) are obtained by LEED-I(V) measurements for the (00) spot. As presented in Figure 4.2(i), the lattice spacing is more than 1.65 Å for a thickness below 3 ML, then it decreases to 1.51 Å as the film thickness increases.

Film stress and structure of Ni on Ir

Ni films are prepared on Ir(100) substrate with a deposition speed of 3-5 min/ ML at room temperature. The stress measurements are carried out during epitaxial growth of Ni monolayers and the film thickness is calibrated with MEED oscillations simultaneously.

Figure 4.3(a) is a characteristic stress curve of Ni monolayers grown on the Ir(100)-(5×1)-H substrate. The surface stress change is slightly increased when the Ni coverage is less than about 0.5 ML. Then up to 2 ML, the tensile surface stress change is induced by the epitaxial growth. For all three surface reconstructions (Figure 4.3(c)) the stress curves show a large positive slope up to 15 GPa in this range (1-2 ML). The surface stress change is relaxed after a kink at 2 ML but remains tensile. Another kink appears around 11-16 ML after which the surface stress is further relaxed and the slope of the curve decreases to less than 1 GPa. Taking a closer look into the thickness range
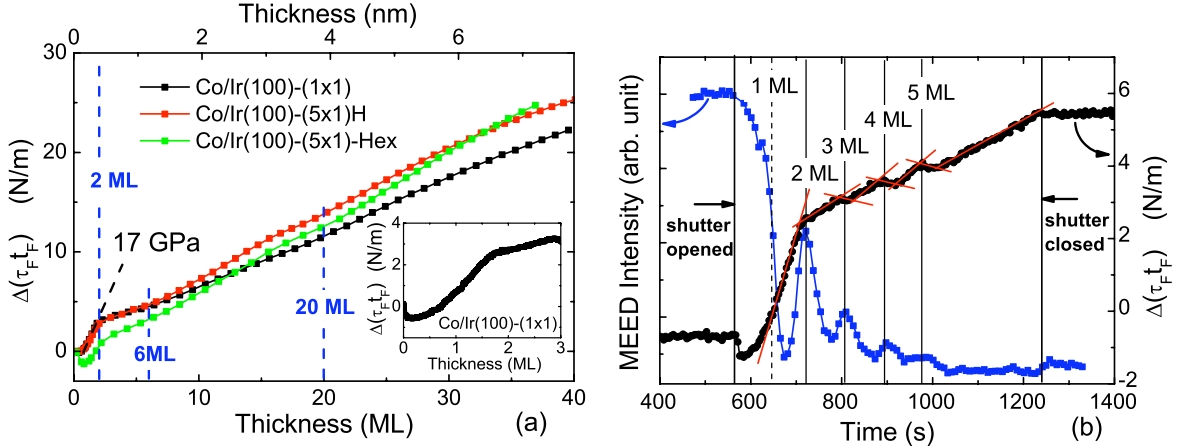
Figure 4.4: (a) Comparison of surface stress change induced by depositing Co mono-layers on different Ir(100) surface reconstructions. (b) Stress oscillations and MEED oscillations during deposition of Co on Ir(100).

between the two kinks at 2 ML and 11-12 ML as shown in Figure 4.3 (b), weak layer-wise modulations appear after subtraction of a reference line (the linear fitting of the data—green dashed line in Figure 4.3(a)), the amplitude of the modulation is less than 0.2 N/m. In the same thickness range, partial dislocations are found to occur by STM studies [77], which may be associated with the stress modulations.

The stress curves for Ni on different Ir(100) surface reconstructions exhibit the same thickness dependence at various stages, as shown in Figure 4.3 (c). In the submonolayer range, the surface stress is reduced considerably to about -1.7 N/m with no more than 0.8 ML Ni coverage on Ir(100)-(5×1)Hex, but it remains unchanged on the (1×1) and (5×1)-H surface reconstructions. From 1 ML to 2 ML, the slopes of all the three stress curves are as large as 15 GPa. In the next stage, the stress change on (1×1) and quasi-hexagonal surface reconstructions are very similar up to 20 ML. However, the slope of the stress curve is reduced more on the (5×1)-H substrate. Figure 4.3 (d) shows the LEED image for 5 ML Ni grown on Ir(5×1)-H surface taken at room temperature. The clear quadratic pattern is similar to that of a Ni film on the (1×1) surface.For Ni films on (1×1) below 5 ML, the LEED patterns are clear and similar to that of the Ir substrate. The diffraction spots in the LEED images for Ni films thicker than 5 ML are blurred gradually, suggesting a deteriorating long-range order of the Ni lattice.

Film stress and structure of Co on Ir

The stress curves for Co films grown on different Ir(100) surface reconstructions are shown in Figure 4.4(a). From 1 ML to 2 ML, a large tensile stress change which corresponds to a film stress of 17 GPa is observed. With increasing film thickness the stress curve bend down, indicating a relaxed film stress. The induced stress change shows a slight up-and-down change from 6 ML to about 20 ML which is more clear in the stress curve of Co on the (5×1)-H and the (5×1)Hex surface reconstructions than on the (1×1) surface. There is no more obvious changes with more Co layers being deposited.

In the large scale plot there are some features hard to be noticed. When taking a
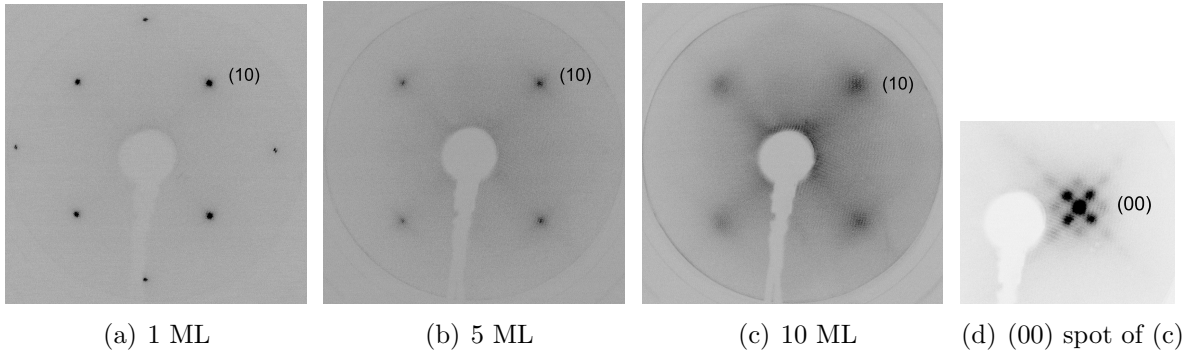
(a) 1 ML   (b) 5 ML   (c) 10 ML   (d) (00) spot of (c)

Figure 4.5: LEED images of Co on Ir(100)-(1×1) for different film thickness at 100 eV (a)-(c) and (d) the (00) spot for 10 ML Co on Ir(100)-(1×1) at 20 eV.

closer look at the low coverage range we find film stress oscillates with mono-layer period from 2 ML to 5 ML. The stress curve and the MEED oscillation obtained simultaneously are plotted in Figure 4.4(b). It can be clearly seen that the stress curve shows small modulations from 2 ML to 5 ML which is coincident with the oscillation of MEED intensity. The magnitude of the stress oscillations in the curve increases as the thickness increase from 3 to 5 ML when the MEED oscillations show a decreasing amplitude.

Figure 4.5 presents the LEED images for Co monolayers on the Ir(100)-(1×1) substrate. For Co films with thickness of no more than 2 ML, clear (1×1) patterns are observed. Extra spots emerge around the original spots in the (1×1) pattern for film thickness larger than 5 ML, which is easier to see at low energy around 20 eV as shown in Figure 4.5(d). These satellite spots may be attributed to the dislocation network formation, as will be discussed in Section 5.1.1.
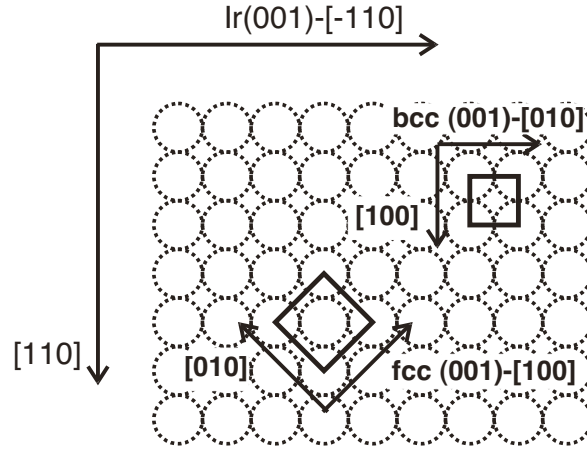
Figure 4.6: The Ir(100) substrate and the respective directions of crystal axes in the epitaxial films. The dashed circles represent the Ir atoms at the surface and the solid squares stand for the lattice of the epitaxial film.

4.2 Magnetism and magnetoelastic coupling of Fe, Co and Ni monolayers on Ir(100)

Magnetic properties of Fe, Co and Ni monolayers are measured with MOKE after deposition. The in-plane magnetization is studied with longitudinal MOKE and transverse MOKE, and the out-of-plane magnetization is investigated with polar MOKE. Whether the easy magnetization is perpendicular to the film or parallel to the film is hence determined.

According to Equation 2.6, for cubic (001) magnetic films, the magnetoelastic anisotropy for out-of-plane magnetization is $B_1(\epsilon_\parallel - \epsilon_\perp)$, with $\epsilon_\parallel$ and $\epsilon_\perp$ representing the in-plane strain and out-of-plane strain respectively. Therefore the value of B_1 is of great significance in determining the perpendicular magnetization easy axis or the spin reorientation, especially when film strain is not negligible. The film strain can be obtained from the stress that is measured during growth (see page 55). The magnetoelastic coupling in thin films can be quite different from that in the bulk [25, 28, 78], and therefore I measured the effective magnetoelastic coefficients B_1^{eff} and B_2^{eff} for Fe, Ni and Co monolayers on Ir(100).

Based on the analysis in Section 2.4, the value of B_1 can be obtained from the magnetoelastic coupling induced stress change between M∥[100] and M∥[010] (an example has been shown in Figure 3.3). Similarly, the effective magnetoelastic coefficient B_2 can be measured by magnetoelastic stress measurement with magnetizations along [110] and [$\bar{1}$10], respectively. For our experiments, the [100] and [010] axes of the magnetic films are parallel to the length and width of the sample. From the structural analysis we learn that Ni and Co show a fcc phase on Ir(100) and their [100] direction is parallel to Ir(100)-[100], while for bcc-Fe the lattice is rotated 45° for epitaxial growth hence Fe(100)-[100] is parallel to Ir(100)-[110]. The relative geometry of fcc lattice for Ni and Co and bcc lattice for Fe on Ir(100) is shown in Figure 4.6. For the reasons mentioned above two Ir(100) substrates are used in the experiment to obtain both B_1 and B_2. One has its length and width along [100] and [010] axis, the other one is cut along [110] and

(a) MOKE for 40 ML Co on Ir(100)-(1×1)

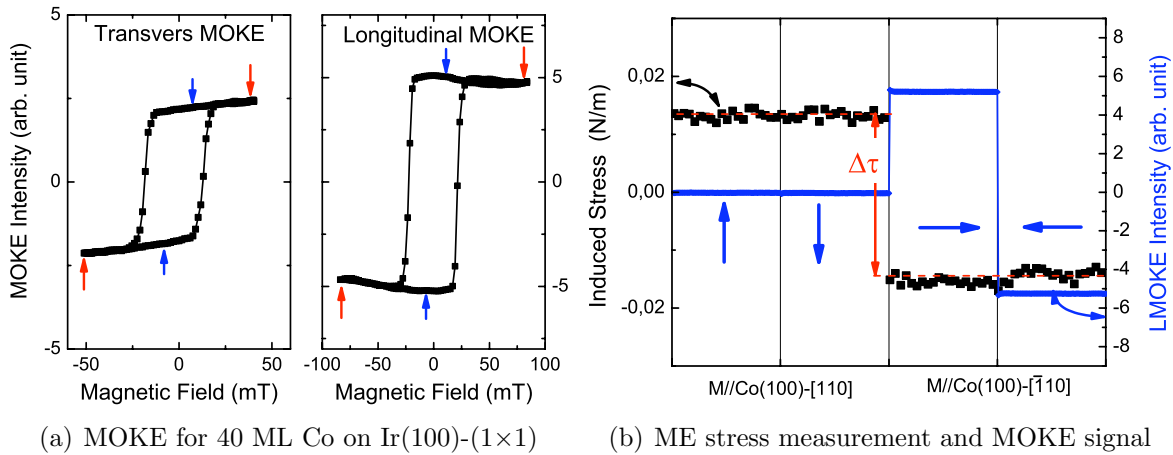(b) ME stress measurement and MOKE signal

Figure 4.7: (a) Hysteresis loops for 40 ML Co on Ir(100)-(1×1) with transvers MOKE and longitudinal MOKE. The magnetic fields applied for saturate and fix the magnetization (see description in page 17) are indicated with red and blue arrows respectively. For magnetoelastic stress measurement (b) the magnetization is firstly aligned with transverse directions ([110] of fcc-Co(100)) and then switched to longitudinal directions([$\bar{1}$10] of fcc-Co(100)). The magnetoelastic coupling induced stress change is represented by the black dots, and the blue dots exhibits the longitudinal MOKE intensity during the magnetoelastic stress measurement.

[$\bar{1}$10], respectively.

Figure 4.7 shows an example of magnetoelastic stress measurement for B_2^{eff} of 40 ML Co on Ir(100)-(1×1). The MOKE measurements give the response of the magnetization to the external field by the hysteresis loops. After that, the magnetoelastic stress measurement is performed in the following sequence: external field large enough to align the magnetization in the vertical in-plane direction upwards, then the induced stress change is measured in a reduced magnetic field that is close to zero but large enough to maintain the alignment of the magnetization. With the same sequence, magnetoelastic stress is measured for magnetization along the vertical direction downwards, and horizontal direction towards left and right. The magnetization states are monitored during the stress measurements by MOKE for confirmation. The value of B_2^{eff} is given by the magnetoelastic stress difference $\Delta\tau_{ME} = \Delta\tau/t_F$, hence for 40 ML Co on Ir(100), $B_2^{eff} = 3.8$ MJ/m^3.

As is introduced in Chapter 1, it has been found that the effective magnetoelastic coupling coefficients in thin films show a strain dependence. And we found a linear-like strain dependence for the value of B_i^{eff} obtained in this study, therefore the relation between B_i^{eff} and in-plane strain is fitted with $B_i^{eff} = B_i + D_i\epsilon_{//}$ considering the second-order effect, as will be discussed in Section 5.1.3.
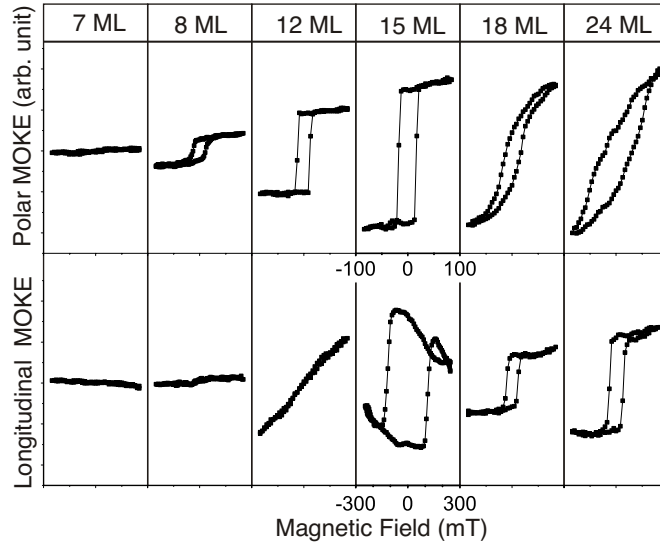
(a)
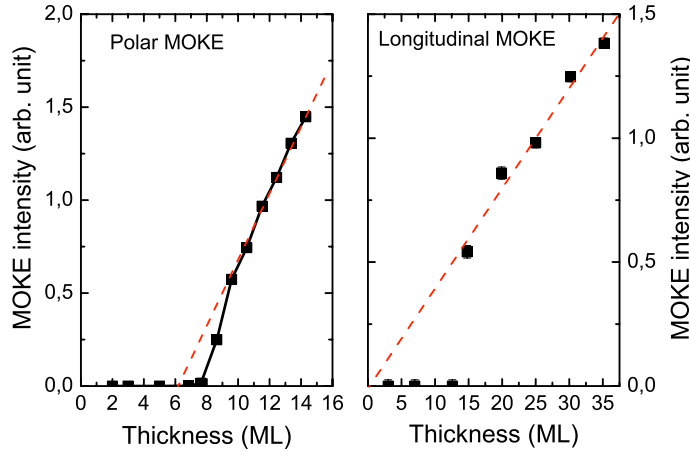
(b)

Figure 4.8: (a) MOKE hysteresis loops at different Ni film thickness at room temperature. The x and y axis are in the same scale for different loops, except for the longitudinal MOKE curve of 15 ML Ni. Here the magnetic field is 3 times larger as compared to the other curves. (b) Intensity of the saturated MOKE signal of Ni monolayers on Ir(100)-(5×1)Hex, measured at room temperature. The polar MOKE measurements are performed in a series of successive experiments.

4.2.1 Magnetism, spin reorientation and magnetoelastic coupling of Ni/Ir(100)

A spin reorientation from out-of-plane to in-plane for Ni films on Ir(100) is observed in this study. At room temperature, there is no hysteresis loop observed for a thickness less than 8 ML, neither in polar nor in longitudinal MOKE measurement. Square-like hysteresis loops show up for polar MOKE at $t_F = 8$ ML, and the amplitude increases with thickness up to about 15 MLs as shown in Figure 4.8(a). Longitudinal MOKE shows the hysteresis loops along hard axis, indicating that the easy magnetic axis is per-
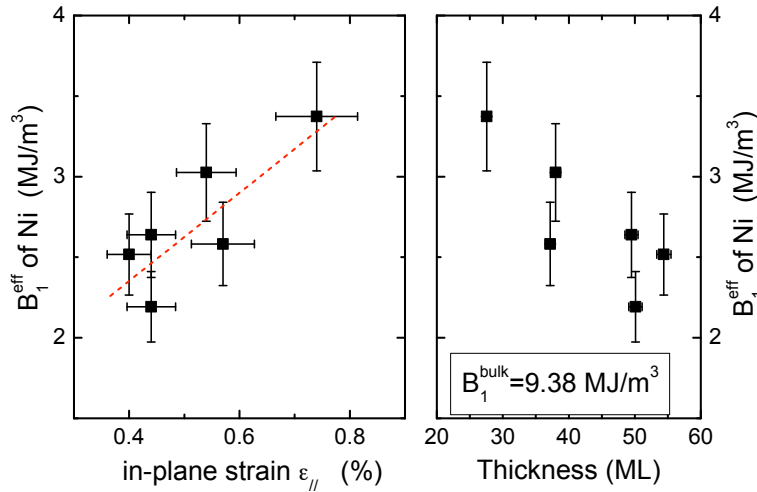
Figure 4.9: Strain and thickness dependence of effective magnetoelastic coefficient B_1 of Ni on Ir(100). The red dashed line represents a linear fit between B_1^{eff} and in-plane strain $\epsilon_{//}$: $B_1^{eff}=1.3$ MJ/m^3+273 MJ/m$^3 \epsilon_{//}$.

pendicular to the film surface from 8 ML to ∼15 ML. At higher Ni thickness, square-like hysteresis loops are observed in the longitudinal MOKE geometry and the polar MOKE shows hysteresis loops along the hard axis accordingly. This indicates that the easy axis changes from out-of-plane to in-plane. It is notable that the longitudinal MOKE of 15 ML Ni also shows a hysteresis loop, while the coercivity is much larger than that of the polar MOKE loop, the maximum intensity is obtained close to zero field and when the longitudinal field is increased, the signal decreases accordingly. The maximum intensity of the longitudinal MOKE is the same with that of the polar MOKE. Since the optical settings for longitudinal MOKE measurement are the same with the polar MOKE measurement except that the magnetic field is applied perpendicularly (see Section 3.2), the magnetization signal close to zero field may be attributed to longitudinal MOKE. The linear fitting of the longitudinal MOKE intensity (Figure 4.8(b)) extrapolated to zero ML is almost zero, suggesting that there is no "dead layer" at the surface or interface, and the magnetization of all the Ni layers turns to in-plane after the spin reorientation.

With LN$_2$ cooling, hysteresis loops for polar MOKE are also observed at 7 ML, indicating the easy magnetization axis for 7 ML Ni is out of plane and that the Curie temperature is below room temperature. Comparing with Ni films on Cu(001) and Ni(111) on Re(0001) whose Curie temperature of 4-5 ML Ni is already above room temperature [49] (5.3 ML Ni/Cu(001): Tc∼330 K; 4 ML Ni(111)/Re(001): Tc∼450 K), the Curie temperature of Ni films on Ir(100) appears to be relatively low.

The MOKE measurements reveal that Ni films show a perpendicular easy magnetization direction when the thickness is less than 18 ML. Since the magnetization need to be aligned between two in-plane directions for magnetoelastic stress measurements to get the B_1^{eff} and B_2^{eff}, the magnetoelastic stress measurements are carried out for Ni films thicker than 20 ML when the magnetization is in-plane, as verified by MOKE. The results are shown in Figure 4.9 and Figure 4.10.

The magnetization is saturated along Ni(100)-[100] and [010] to measure B_1^{eff} of the Ni films. As shown in Figure 4.9(right panel), the values of the effective B$_1$ for various
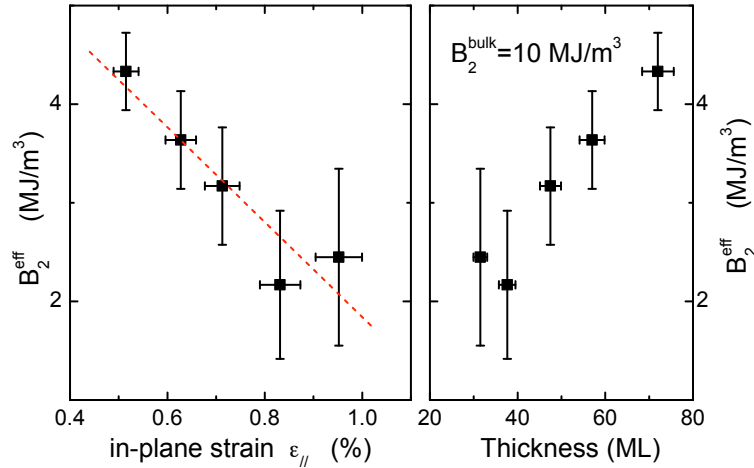
Figure 4.10: The effective magnetoelasitic coupling coefficient B_2 of fcc Ni on Ir(100). The linear fitting of the strain dependence is indicated as the red dashed line, which gives $B_2^{eff} = 6.6\frac{\text{MJ}}{\text{m}^3} - 480\frac{\text{MJ}}{\text{m}^3} \cdot \epsilon_{\parallel}$.

thicknesses differ from the bulk value of 9.38 MJ/m³. In the thickness range explored (20∼60 ML), B_1^{eff} deviates more from the bulk value as the thickness increases. To demonstrate the dependence on the film strain, the in-plane film strain $\epsilon_{//}$ obtained from stress measurement is set as x-axis. Linear fitting of the plots results in the relation between B_1^{eff} and in-plane strain $\epsilon_{//}$ as follows

$$\text{(fcc-Ni with positive film strain):} \quad B_1^{eff} = 1.3\frac{\text{MJ}}{\text{m}^3} + 273\frac{\text{MJ}}{\text{m}^3} \cdot \epsilon_{\parallel} \tag{4.1}$$

To obtain B_2^{eff} of Ni on Ir(100), the magnetization is switched between Ni(100)-[110] and [$\bar{1}$10]. Ni films with thickness from 30 ML to 70 ML with the easy axis in the plane are studied, MOKE measurements reveal that the magnetization remains at full remanence at zero field along [110] and [$\bar{1}$10].

The obtained B_2^{eff} of Ni on Ir(100)-(1×1) is plotted in Figure 4.10. The data all differ from the bulk value of 10 MJ/m³. However, the value of B_2^{eff} gets close to the bulk value as the film thickness increases.

The strain dependent B_2^{eff} can be fitted with linear relation as

$$B_2^{eff} = 6.6\frac{\text{MJ}}{\text{m}^3} - 480\frac{\text{MJ}}{\text{m}^3} \cdot \epsilon_{\parallel} \tag{4.2}$$

As shown in Figure 4.9 and 4.10, the experimental determined B_i^{eff} of Ni monolayers shows a strain dependence, and can be expressed as a linear relation. It is in line with the idea of strain dependent magnetoelastic coupling and will be discussed in Section 5.1.3.
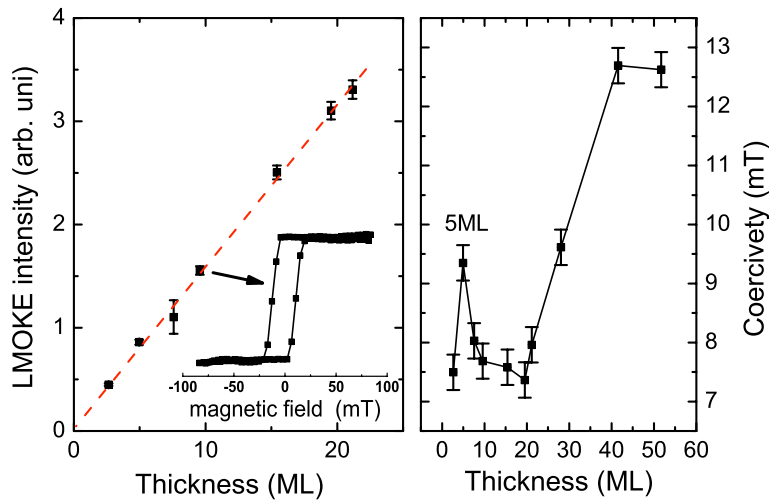
Figure 4.11: MOKE intensity with saturated magnetization and the coercivity for different Co film thicknesses.

4.2.2   Magnetism and magnetoelastic coupling of Co on Ir(100)

For Co films grown on Ir(100), square-like shape hysteresis loops are obtained with thickness ranging from 2 ML to 60 ML in longitudinal MOKE measurements, indicating an in-plane magnetic easy axis in the whole thickness range. The longitudinal MOKE intensity at saturated magnetization states is plotted in Figure 4.11, in which the MOKE intensity increases linearly with film thickness. The extrapolation of the linear fitting goes through the origin point, with no positive or negative offset within the error bar. Coercivety during the magnetization process is also obtained from the hysteresis loops for different film thicknesses. From 2 ML to 20 ML, the coercivety is about 7-8 mT except for the anomaly at 5 ML, where H_c peaks at 9.5 mT. The coercivity increases gradually from 20 ML to about 45 ML and then keeps constant up to 55 ML. The change of the coercivity in Co films when the magnetic field is parallel to the easy axis will be discussed in Chapter 5.

B_1^{eff} for fcc-Co monolayers on Ir(100) is measured with the magnetization switched between [100] and [010]. The results are shown in Figure 4.12. The experimental results differ from the bulk value of -9.2 MJ/m^3, and the results can be described with a strain dependence of B_1^{eff} as

$$\text{(fcc-Co with positive film strain):}\quad B_1^{eff} = 3.5\frac{\text{MJ}}{\text{m}^3} - 842\frac{\text{MJ}}{\text{m}^3}\cdot\epsilon_\parallel \qquad (4.3)$$

The experimental results are well described with the linear fitting as the in-plane strain ranges from 0.85% to 0.4%. However, when the strain is larger than 0.85% or the film thickness is less than 15 ML, the plots departs from the linear fitting. Similar to the results for Ni monolayers, again the value of B_1^{eff} deviates more from the bulk value as the film strain decreases or the film thickness increases.

B_2^{eff} of fcc Co with a positive film strain ranging from $\sim 0.6\%$ to 1.0% is measured, with the thickness from 8 ML to 42 ML. The results are shown in Figure 4.13.

The strain dependence of B_2^{eff} is also fitted (least square fitting) with a linear
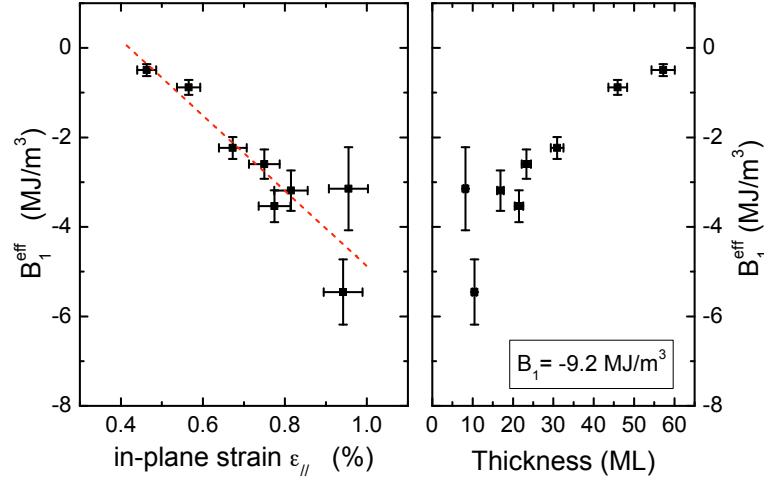
Figure 4.12: Measured effective magnetoelastic coefficient B_1 of Co on Ir(100)-(1×1). The strain dependence can be expressed by a linear fit $B_1^{eff} = 3.5\frac{\text{MJ}}{\text{m}^3} - 842\frac{\text{MJ}}{\text{m}^3} \cdot \epsilon_{\parallel}$, as indicated by the dashed red line (see text).
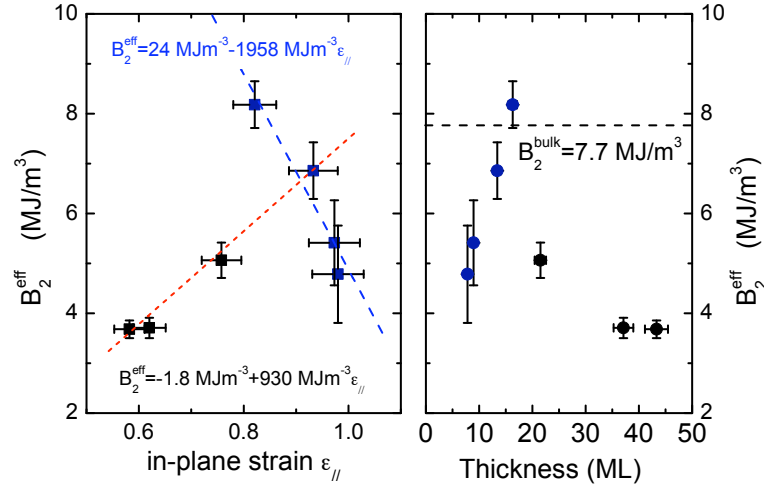

Figure 4.13: The effective magnetoelasitic coupling coefficient B_2 of fcc Co on Ir(100). (B_2 of fcc Co in the bulk is 7.7 MJ/m³.) The obtained B_2^{eff} does not show a simple relation with either in-plane strain or the film thickness. A least-square linear fitting is given for comparison (red dashed line), and the values for thinner films (t_F less than 20 ML) are fitted separately, which will be discussed in Sec. 5.1.3.

relation as

$$B_2^{eff} = -1.8\frac{\text{MJ}}{\text{m}^3} + 930\frac{\text{MJ}}{\text{m}^3} \cdot \epsilon_{\parallel} \qquad (4.4)$$

However, the plots with in-plane strain larger than 0.8% depart drastically from the linear fitting. In the right graph, two types of B_2^{eff} behavior can also be distinguished. For film thickness less than about 20 ML, B_2^{eff} increases with the thickness, yet for the thickness larger than 20 ML, the value of B_2^{eff} decreases gradually.
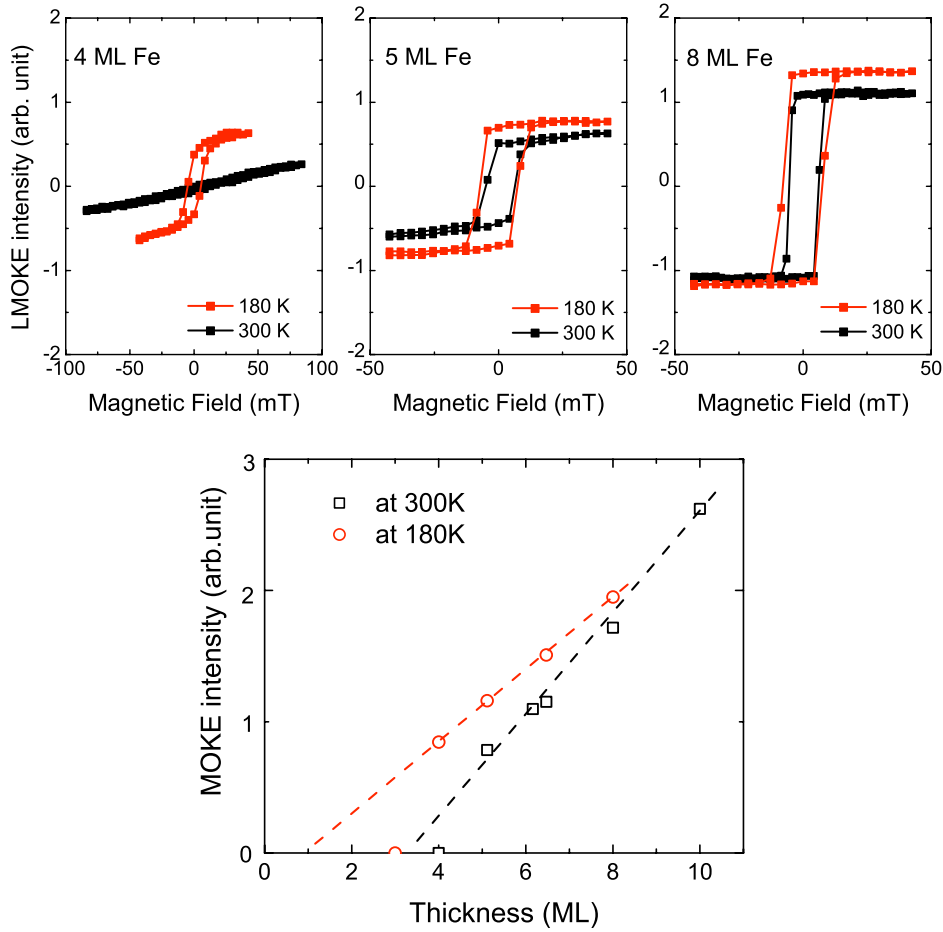
Figure 4.14: MOKE intensity of Fe monolayers on Ir(100)-(1×1) for different thickness. The hysteresis loops are obtained at 180 K and 300 K

4.2.3   Magnetism and magnetoelastic coupling of Fe on Ir(100)

The magnetic properties of Fe monolayers on Ir(100) are explored by MOKE measurements both at room temperature and low temperature with LN_2 cooling. At room temperature, hysteresis loops are obtained for Fe films with thickness no less than 5 ML. When the sample is cooled down to ~180 K, a hysteresis loop is also obtained at 4 ML, yet no magnetic signal is observed for the 3 ML Fe film. Longitudinal MOKE shows square-like hysteresis loops from 4 ML up to 60 ML and no perpendicular magnetization is observed, indicating an in-plane easy magnetization axis. In Figure 4.14, the MOKE intensity of the saturated magnetization is plotted for different Fe thickness within the pseudomorphic growth range (less than 10 ML). The intensity increases linearly as the film thickness increases, and the extrapolation to zero ML might approach to zero as the temperature is reduced further.

The B_1^{eff} in Fe(001) monolayers with compressive misfit strain of -4.9% is explored on Ir(100). The film strains for different thicknesses are obtained from stress measurement as discussed in Section 5.1.1 and shown in Figure 5.3(b) (page 56). The results are shown in Figure 4.15. The values of B_1^{eff} are significantly different from the bulk value of -3.4 MJ/m^3 with film thickness varying from a few monolayer up to about 10 nm. As indicated in the figure, for Fe films with different thicknesses but similar film strain
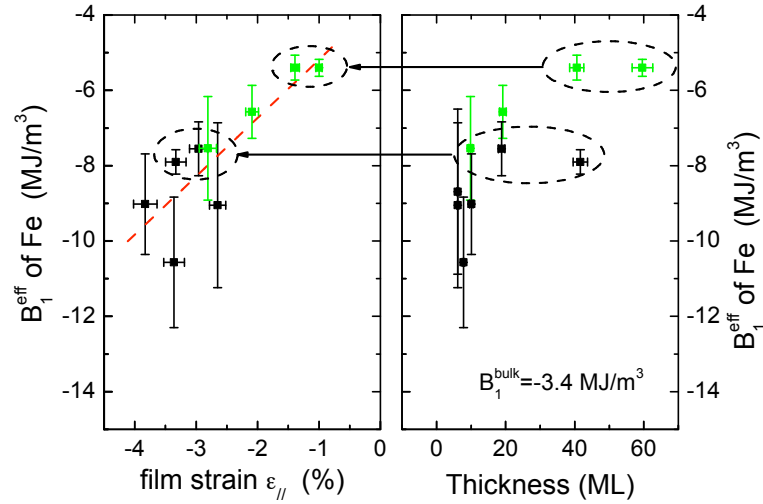
Figure 4.15: Strain and thickness dependence of the effective magnetoelastic coefficient B_1^{eff} for Fe monolayers deposited on Ir(100). B_1^{eff} values for Fe(100) films on Ir(100)-(5×1)-H are given by the green dots and the black dots indicate the B_1^{eff} for Fe on the (1×1) surface. The red dashed line is the linear fitting of the relation between B_1^{eff} and in-plane strain $\epsilon_{//}$ as $B_1^{eff} = -3.6\frac{\text{MJ}}{\text{m}^3} + 155\frac{\text{MJ}}{\text{m}^3} \cdot \epsilon_{\parallel}$. The datas in the dashed ellipse with different thickness but similar strain show a similar value of B_1^{eff} (see text).

(points in the ellipses) the values B_1^{eff} are alike, which implies that the magnetoealstic coupling coefficient of B_1^{eff} is rather strain-dependent than thickness dependent. The relation between B_1^{eff} and the film strain can be expressed as

$$(\text{bcc-Fe with negative film strain}): \quad B_1^{eff} = -3.6\frac{\text{MJ}}{\text{m}^3} + 155\frac{\text{MJ}}{\text{m}^3} \cdot \epsilon_{\parallel}. \quad (4.5)$$

It is found that B_1^{eff} of Fe on Ir(100)-(1×1) and (5×1)-H surface show the same strain dependence.
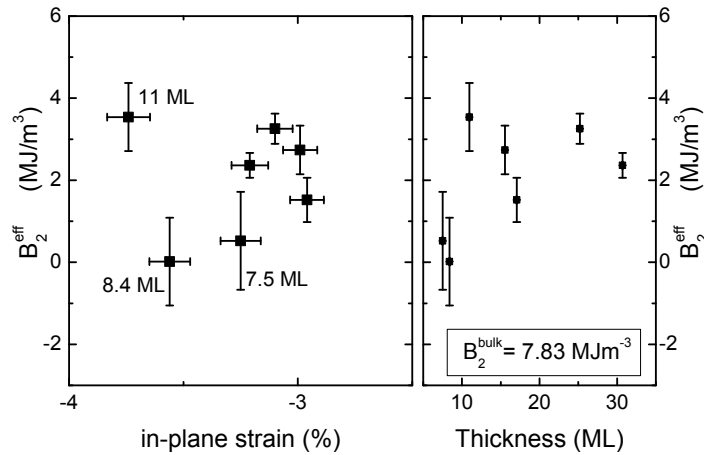

Figure 4.16: The effective magnetoelastic coupling coefficient B_2 of bcc Fe(100) films on Ir(100). The values of B_2^{eff} show no clear dependence on strain and thickness. The values of B_2^{eff} are all different from the respective bulk value of 7.83 MJ/m³.

B_2^{eff} of Fe films grown on Ir(100)-(1×1) are measured for film thickness between 7.5 ML and 30 ML. As shown in Figure 4.16 the obtained B_2^{eff} differs from the bulk value of 7.83 MJ/m^3. For Fe films with thickness of 7.5 ML and 8 ML, B_2^{eff} is almost zero within the error limits. The relation between B_2^{eff} and strain and/or thickness is not evident from the substantial scatter of the data points, and a fit of the data points does not appear to be justified.
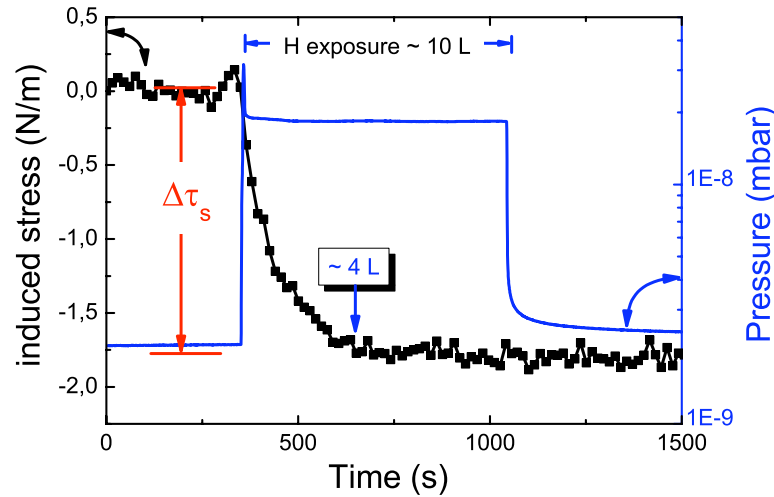
Figure 4.17: The surface stress change during H adsorption on Ir(100)-(5×1)Hex as a function of time at P_H=2×10^{-8} mbar.

4.3 Adsorption-induced surface reconstruction — combined surface stress and LEED studies

As has been introduced in Section 3.3, the Ir(100)-(5×1)-H surface reconstruction can be obtained by hydrogen adsorption on Ir(100)-(5×1)Hex at room temperature. After the Ir(100)-(5×1)Hex surface is prepared, hydrogen is then offered at room temperature with a constant pressure, e.g. 2×10^{-8} mbar. The surface stress change is measured as the quasi-hexagonal surface changes into the (5×1)-H upon H-exposure. Simultaneously, the system pressure and the temperature of the sample are recorded.

Figure 4.17 shows a typical stress curve for the H-induced surface reconstruction change. Before hydrogen is introduced into the chamber, the surface stress is constant. A compressive stress change is observed as soon as hydrogen is offered onto the Ir(100)-(5×1)Hex surface. As hydrogen exposure increases, the induced stress increases toward the negative direction gradually till the hydrogen exposure reaches 4 L (1 Langmuir=1.33×10^{-6} mbar·s) when the surface stress change saturates. The overall stress change is −1.7 N/m (± 0.05 N/m).

The LEED images of Ir(100)-(5×1)Hex and Ir(100)-(5×1)-H have been shown in Figure 3.11. For the quasi-hexagonal surface, the diffraction spots are clear and sharp, the intensity of integer spots and fractional spots are almost equivalent. Contrary to this, the LEED image of Ir(100)-(5×1)-H presents weak stripes between spots, the intensities of the integer spots is higher than those of the fractional spots. The evolution of LEED pattern during H-induced reconstruction is shown in Figure 4.18. The integer spot intensity is enhanced when hydrogen is offered on the Ir(100)-(5×1)Hex surface at room temperature, and the fractional spot intensity decreases at the same time. The ratio between integer spot intensity and fractional spot intensity is regarded as an indication of surface reconstruction.

In order to explore the influence of H-adsorption on the structural change, the surface stress change is carefully measured during exposure at 150°C, which is above the desorption temperature (∼130°C [79]) of H on Ir(100). After the clean Ir(100)-(5×1)Hex

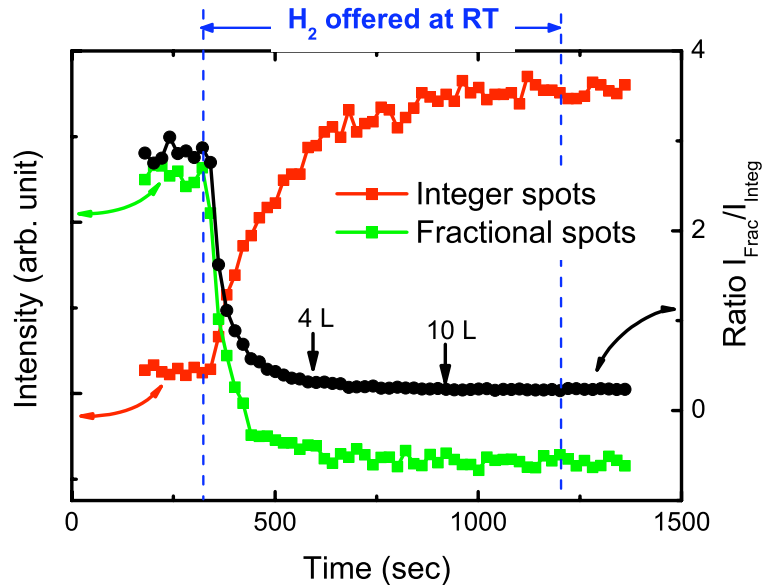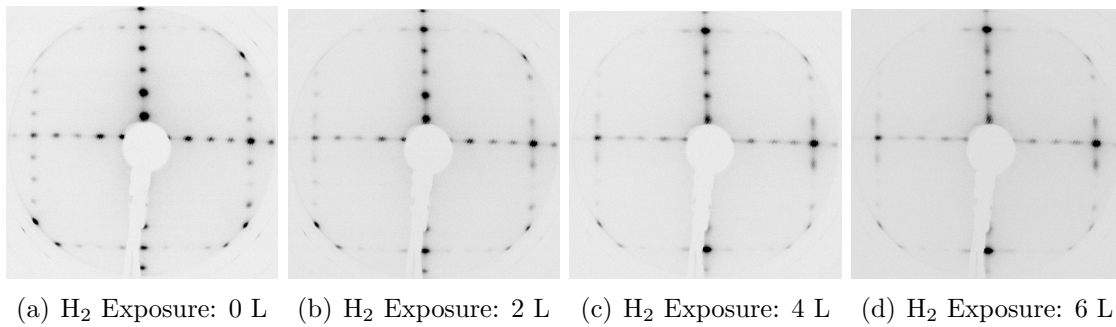(a) H₂ Exposure: 0 L   (b) H₂ Exposure: 2 L   (c) H₂ Exposure: 4 L   (d) H₂ Exposure: 6 L

Figure 4.18: LEED patterns of Ir(100) surface (a)-(d) and (e)LEED spot intensity change as the surface reconstruction changes from (5×1)Hex to (5×1)-H upon H₂ Exposure.

surface is obtained, the sample is slowly heated to 150°C. The sample temperature is stabilized before stress measurement. As shown in the Figure 4.19(a), the surface stress is stable before and after hydrogen is offered and remains the same upon hydrogen exposure. With the same amount of hydrogen exposure as applied at room temperature ($\approx$ 10 L), the surface stress change of -1.75 N/m measured at room temperature is not observed. In addition, the LEED pattern (Figure 4.19(c)) also remains the same as that before hydrogen is offered, which is in line with the stress measurement.

For comparison, the induced stress change are measured for H-adsorption on Ir(100)-(1×1) surface at room temperature, the results are shown in Figure 4.20. A compressive stress change is observed when hydrogen is offered onto the clean (1×1) surface. The stress change saturates upon H-exposure of $\sim$3 L and the overall stress change is -0.5 N/m. LEED measurements show no difference before and after H-exposure.
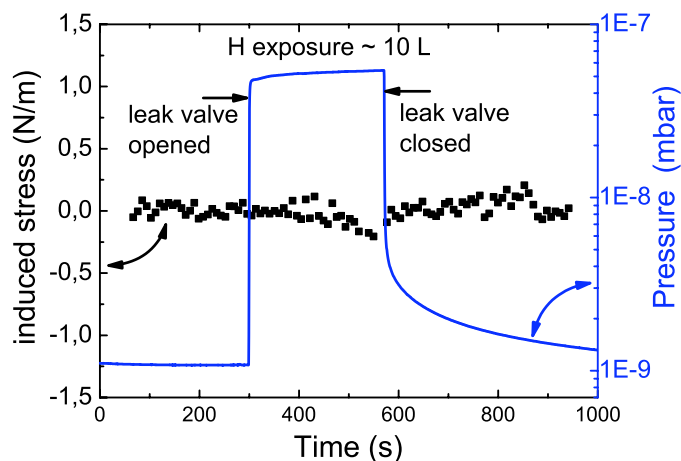
(a)
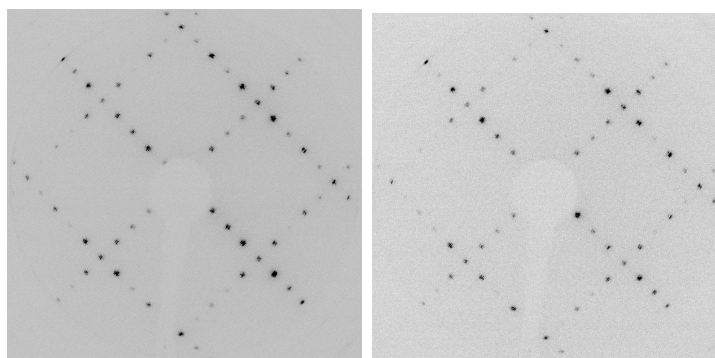
(b) before (E=100 eV)   (c) after (E=100 eV)

Figure 4.19: The stress change during H-exposure at about 130°C and the LEED images taken before and after hydrogen is offered onto the Ir(100)-(5×1)Hex surface. The LEED images are almost unchanged, and the stress stays unchanged before and after exposure.
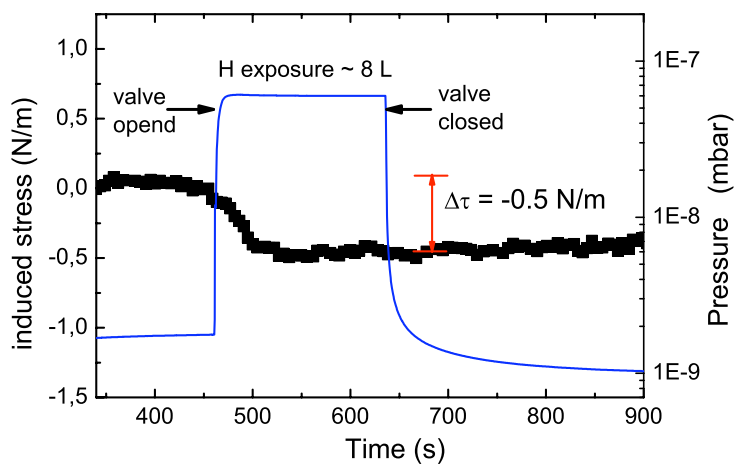

Figure 4.20: Stress change (black dots) measured during H-adsorption on clean Ir(100)-(1×1) surface. The pressure is recorded during exposure as indicated by the blue line. The overall stress change is −0.5 N/m.
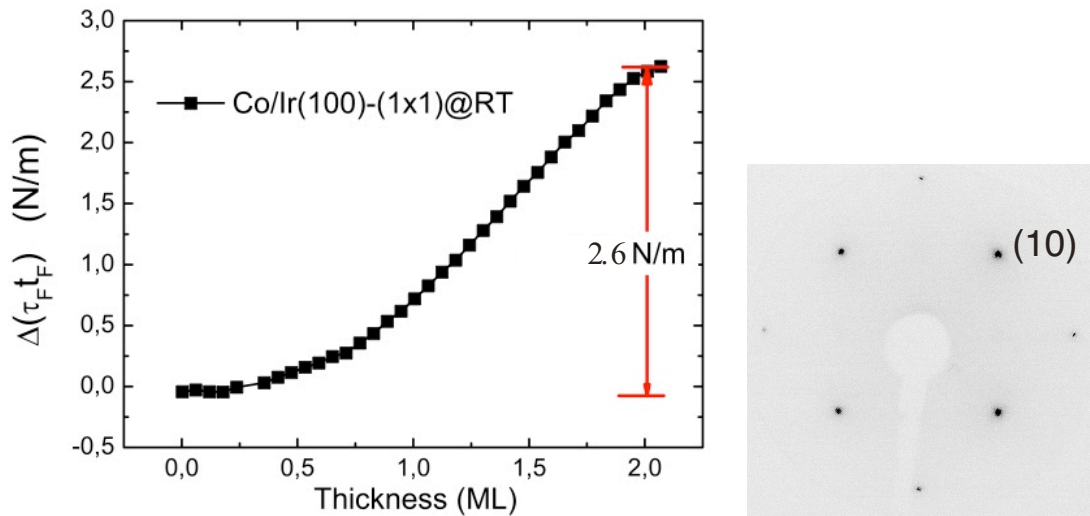
Figure 4.21: Stress change induced by epitaxial growth of 2 ML Co on Ir(100)-(1×1) and the LEED image taken after deposition (E=100 eV).

4.4   Surface stress study during oxidation of 2 ML Co on Ir(100)

It has been found recently that the polar oxide CoO(111) films can be obtained by post-oxidation of thin Co films epitaxially grown on Ir(100)-(1×1) [80]. This provides a good opportunity to study the surface stress change duringan oxide formation with a polar surface. After the clean (1×1) substrate is prepared (see Section 3.3), 2 ML Co is deposited at room temperature. The stress curve during deposition and LEED images taken for 2 ML Co on Ir(100)-(1×1) are shown in Figure 4.21. As has been introduced in Section 4.1 (page 33), a tensile stress change is induced by Co film growth, and the pseudomorphic growth ends at 2 ML. The overall stress change induced by 2ML Co on Ir(100)-(1×1) is about 2.6 N/m. LEED images clearly show a (1×1) pattern with sharp spots.

The sample is then carefully heated to about 200°C, and the sample temperature is stabilized before the stress measurement. Additionally, the pressure during heating is kept below 5×10^{-10} mbar. Then oxygen is offered at a pressure of 2×10^{-6} mbar, the induced surface stress change is shown in Figure 4.22.

With the sample temperature being stable at about 200°C, the stress keeps constant before oxygen is introduced into the chamber. As soon as oxygen is offered, a dramatic compressive stress change as large as -4.3 N/m is induced within exposure of 10 L. Then the stress increases quickly until the oxygen exposure reaches about 100 L where it starts to creep up much slower up to an exposure of 350 L. After that, the stress stays constant upon more oxygen exposure (even up to 5000 L, which is not shown in the figure) and remains unchanged after the oxygen is removed from the UHV chamber. The largest stress change is induced with oxygen exposure less than 100 L, resulting in the significant negative peak at the very beginning of the oxidation process. Eventually, the overall compressive stress change is -0.5 N/m(± 0.1 N/m).

The LEED images taken after oxidation are shown in Figure 4.22. The diffraction

(a)

(b) 400 L

(c) 10 L

(d) 100 L

(e) 160 L
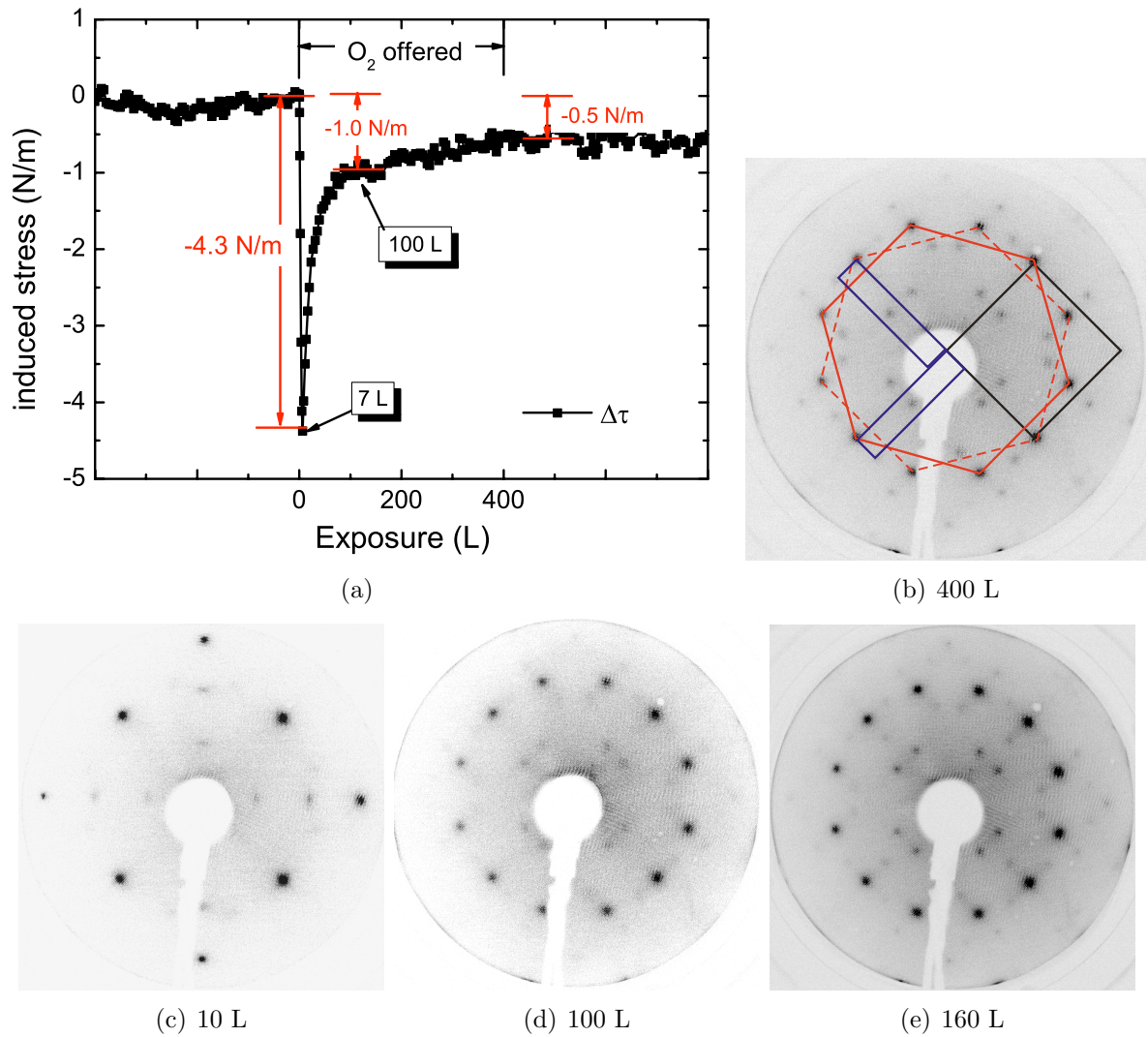
Figure 4.22: Stress change measured during post-oxidation of 2 ML Co on Ir(100) at about 200 °C and the corresponding LEED pattern of 2 ML CoO/Ir(100) (see text), and the LEED images of post oxidation of 2 ML Co on Ir(100)-(1×1) upon different amount of oxygen exposure.

spots originate from the quasihexagonal CoO(111) film with a c(10×2) reconstruction [80]. There are two equivalent orthogonal domains for this c(10×2) structures, and the LEED pattern is a result from multi-diffraction of the quadratic substrate and the quasi-hexagonal CoO layers. The hard sphere model for 2 ML CoO(111) on Ir(100)-(1×1) adapted from Ref. [80] is given in Section 5.2.2 as shown in Figure 5.12. LEED images for different oxidation stages are shown in Figure 4.22. Figure 4.22(c) is taken for 2 ML Co(100) upon oxygen exposure of 10 L, in which the spots mainly stem from a (1×1) cubic lattice. The LEED image in Figure 4.22(d) is taken after oxygen exposure of 100 L and shows diffraction spots that mainly originate from a hexagonal layer while the c(10×2) spots are very weak. Figure 4.22(e) is taken after 160 L oxygen is applied, and the LEED images are identical for the samples that are exposed to oxygen longer than 400 L, even up to 5000 L.

For comparison, oxygen is also offered at room temperature, which results in an

incomplete oxidation. The LEED pattern in Figure 4.23 originates from the quasi-hexagonal CoO(111) surface while the spots are less sharp and the c(10×2) superspots are missing. The diffraction pattern from the (1×1) lattice structure is also not clear, which suggests that the Co(100) monolayers are partially oxidized, resulting in a loss of the 1×1 order. The stress measurement is shown in Figure 4.23. The stress curve also shows a striking decrease as soon as oxygen is offered and then increase rapidly. Upon a certain amount of oxygen exposure the stress curve starts to change slightly and keeps constant at last. Different from a sufficient oxidation process as shown in Figure 4.22, the maximum of the compressive stress change is -2.7 N/m—which is less than -4.3 N/m observed at 200°C—with less H exposure of 4 Langmuir, after 4 L of hydrogen exposure the stress increases again and stopped at 12 L, the overall stress change is about -1.6 N/m.
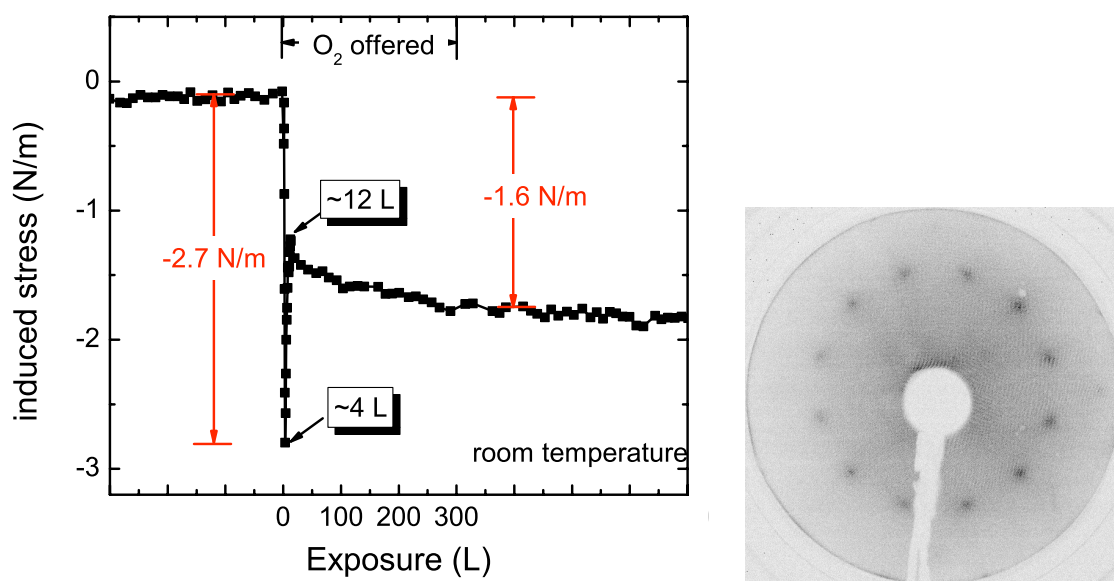

Figure 4.23: O_2 exposure of 2 ML Co/Ir(100)-(1×1) at room temperature. LEED and stress curves identify incomplete oxidation.

Chapter 5

Discussion

The experimental results presented in Chapter 4 reveal that there are close links between strain, stress and the structural change during epitaxial growth as well as the surface structural alternations, such as surface reconstruction and oxidation. For the magnetic thin films, strain dependence of the magnetoelastic coupling is also obtained that contributes to the magnetic anisotropy and influences the magnetism. In this chapter, the relation between stress, strain and structure and the magnetoelastic coupling in the epitaxial film is discussed in Section 5.1. An analysis for the role of surface stress for structural transitions is given in Section 5.2

5.1 The correlation between stress, strain, structure and magnetic properties in ultrathin films

According to the results of stress and structural measurements for Fe, Ni and Co monolayers on Ir(100), the stress change during deposition reflects the structural properties in the films, such as lattice structure, pseudomorphic growth and dislocation formations. The film strain can be derived from the inspection of the stress curves. It is found that the effective magnetoelastic coupling coefficients deviates from the bulk value. Film strain may be a decisive factor, and the magnetoelastic anisotropy contributes to the magnetic anisotropies in the magnetic monolayers, therefore the magnetic anisotropies are also linked to the film strain and hence, the film stress.

5.1.1 Structural analysis from the view of stress

a. Pseudomorphic growth: bcc or fcc?

The strain in the films will give rise to a corresponding film stress that generally exists in the epitaxial thin films. For pseudomorphic growth on the substrate, the mismatch η induces a film stress of $\tau_F = \frac{Y_F}{1-\nu_F}\eta$, as has been introduced in Sec. 2.2. Therefore, quantitative analysis of the stresses in the film gives the film strain as well as other structural informations. Based on the *in-situ* stress measurement during deposition, the thickness range of pseudomorphic growth can be determined. The quantitative stress analysis helps to decide whether a strained Fe film corresponds to the fcc or bcc
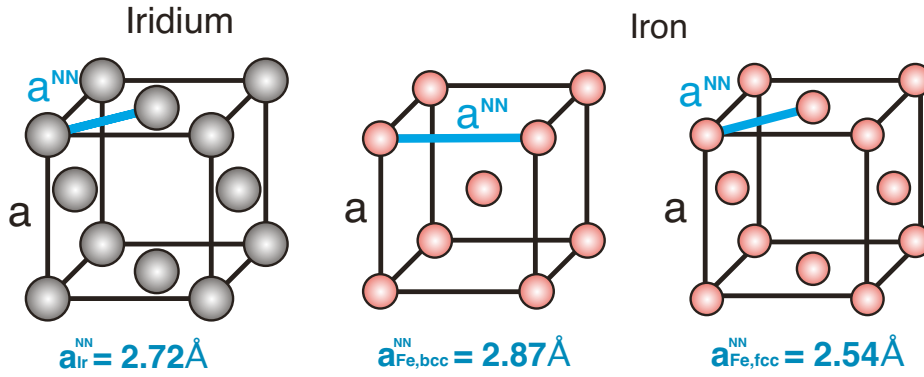
Figure 5.1: Ball model of fcc Ir, bcc Fe and fcc Fe crystal lattices and the corresponding nearest neighbor distances a^{NN} in (100) planes.

Table 5.1: Lattice constants a in Å from Ref. [81], epitaxial misfit $\eta = a_{\parallel,film} - a_{\parallel,bulk}/a_{\parallel,bulk}$, calculated strain along the film normal $\epsilon_{33} = -2\eta c_{12}/c_{11}$, elastic constants c_{ij} in GPa from Ref. [68], Young's modulus $Y = (c_{11}+2c_{12})(c_{11}-c_{12})/(c_{11}+c_{12})$ in GPa, and Poisson's ratio $\nu = c_{12}/(c_{11} + c_{12})$. For a discussion of these quantities see [25].

	a	η	ϵ_{33}	c_{11}	c_{12}	c_{44}	Y	ν
Ir	3.839			600	260	270	443	0.302
Fe, bcc	2.866	-0.053	$+0.062$	230	134	116	131	0.368
Fe, fcc[1]	3.574	$+0.074$	-0.099	200	134	92	92	0.401

[1] Data for fcc-Fe have been obtained for bulk fcc-Fe at high temperature [81,82]. The tabulated values are extrapolated to 300 K. The thermal expansion of fcc Fe is taken as 8.5×10^{-5} Å/K. The c_{ij} are extrapolated to 300 K, assuming the same temperature dependence as given for bcc Fe [83]. Thus, the high temperature data for fcc-Fe [82] c_{11}, c_{12}, and c_{44} are increased by 30 %, 10 %, and 20 %, respectively.

phase.

Fe on Ir(100)

The lattice constant of bcc-Fe is $a_{bcc,Fe}$=2.866 Å in its equilibrium state, and the lattice constant of fcc-Fe is $a_{fcc,Fe}$= 3.574 Å. The crystal lattices and corresponding nearest neighbor distance (a^{NN}) of (100) plane are illustrated in Figure 5.1. The in-plane nearest neighbor distance of Ir(100) (a_{Ir}^{NN}) happens to be in between that of the fcc-Fe(100) and bcc-Fe(100). Accordingly, as shown in Table 5.1 the mismatch between the in-plane lattice spacing of bcc-Fe(100) and Ir(100) is $\eta = -5.3\%$, between fcc-Fe and Ir(100) is $\eta = +7.4\%$. As a result, for bcc-Fe lattice on Ir(100), a compressive film stress of $\tau_F = -11$ GPa is expected, and for fcc-Fe lattice on Ir(100), a tensile film stress of $\tau_F = +11.4$ GPa is expected.

The stress curve obtained for Fe monolayers grown on Ir(100) substrate presents a positive slope of about +7 GPa between 1 ML and 2 ML, then the sign of the slope is

changed at 2 ML, and shows an almost constant negative slope ranging from 2 ML to 10 ML. As has been introduced in Section 2.2, the obtained stress change $\Delta\tau$ is attributed to the integral of the film stresses τ_F in the epitaxial layers as $\Delta\tau = \Delta(\tau_F t_F)$. Therefore the slope of the stress curve indicate the film stress in the epitaxial layers. Comparing with the mismatch induced film stress as calculated above, the film stress from 2 ML to 10 ML is in agreement with the mismatch induced stress for bcc-Fe grown on Ir(100), and the experimental tensile stress from 1 ML to 2 ML is reasonable assuming fcc-Fe grown on Ir(100). The agreements indicate that the pseudomorphic growth of bcc-Fe lattice on Ir(100) extends from 2 ML to 10 ML and the first 2 ML Fe can be understood as a fct precursor.

According to continuum elasticity theory, the out-of-plane strain $\epsilon_\perp$ can be calculated from the in-plane strain $\epsilon_{//}$ from $\epsilon_\perp = -\frac{2\nu}{(1-\nu)}\epsilon_{//}$ considering a homogeneous in-plane strain. So the out-of-plane strain for bcc-Fe is expected to be 6.2% and the perpendicular lattice spacing is 1.52 Å, the lattice is elongated along the perpendicular direction. This is in agreement with the results from LEED-I(V) measurements for thick Fe films, as has been shown in Figure 4.2(i). It is therefore an indication that the thick Fe films are bct rather than fct. In addition, the LEED-I(V) measurements reveal a lattice spacing of around 1.65 (±0.02) Å for 2 ML Fe on Ir(100), which is the same as the calculated lattice spacing of 1.63 Å for fcc Fe film being elastically strained on Ir(100). This is consistent with the above analysis on the stress curve, indicating that the Fe film is bct for thicker films, and it can be described as a fct precursor for the first 2 ML.

Ni and Co on Ir(100)

Unlike Fe films on Ir(100), tensile stresses are induced for Ni and Co monolayers grown on Ir(100) above submonolayer range, there is no change of sign of the slope of the stress curves. The crystal structure of the Ni and Co monolayers are given by analyzing the film stress for pseudomorphic growth as follows.

LEED images for Ni films on Ir(100) show diffraction spots that are quite similar to that of the Ir(100) when the thickness is below 5 ML. The structural properties of Ni on Ir(100) have been carefully studied by Klein [77] *et al.* with STM and LEED. The combination of experimental results from STM and LEED measurements suggest that the pseudomorphic growth of Ni on Ir(100) ends when film thickness reaches 2 ML, and partial dislocations appear when more Ni is deposited.

Bulk Ni crystals have a fcc structure with a lattice constant $a_{fcc,Ni} = 3.52$ Å, hence the in-plane mismatch for fcc-Ni(100) grown on Ir(100) is $\eta = \frac{a_{Ir}-a_{Ni}}{a_{Ni}} = +9.1$ %, and the misfit induced stress is expected to be a tensile stress of about $+19.3$ GPa, the sign of which is in agreement with the tensile stress observed, and the value is close to the film stress in the thickness range of 1-2 ML obtained from stress measurement ($+15$ GPa). Therefore, the stress measurement support that fcc-Ni(100) lattice is pseudomorphically grown on Ir(100) below 2 ML.

Similar to Ni films, for Co monolayers deposited on Ir(100), clear (1×1) LEED patterns are observed for the first few layers. It is known that bulk Co crystallize into an hcp lattice , whereas the fcc phase Co is only stable at high temperature. However, using MBE, Co films in a fcc phase have been successfully fabricated on Cu(100) [84–86] with a misfit strain of -1.8%. With the lattice constant of 3.55 Å, the misfit between fcc-

Table 5.2: Elastic constants c_{ij} and lattice constant of bcc-Ni $a_{bcc,Ni}$ and bcc-Co $a_{bcc,Co}$ from *ab initio* calculations. The Young's modulus Y and ν are calculated from c_{ij} with $Y = (c_{11}+2c_{12})(c_{11}-c_{12})/(c_{11}+c_{12})$, $\nu = c_{12}/(c_{11}+c_{12})$. Misfit of bcc-Ni and bcc-Co on Ir(100) and the misfit induced film stress are also calculated consequently. The results of LSDA and GGA[1] calculation are from Ref. [93], GGA[2] calculations on both nonmagnetic (NM) phase and ferromagnetic (FM) phase of bcc-Ni are from Ref. [92]. The elastic constants c_{ij} and the calculated misfit induced stress τ_F is in GPa.

	$a_{bcc,Ni}$	η	c_{11}	c_{12}	Y	ν	τ_F
LSDA	2.73	-0.00549	199	262	-98.8	0.57	1.26
GGA[1]	2.79	-0.02688	152	232	-128.3	0.60	8.72
GGA[2]-NM	2.80	-0.03036	84	276	-339.2	0.77	44.13
GGA[2]-FM	2.80	-0.03036	157	223	-104.7	0.59	7.70
	$a_{bcc,Co}$	η	c_{11}	c_{12}	Y	ν	τ_F
GGA[2]-FM	2.82	-0.037	193	241	-74.7	0.56	6.3

Co and Ir(100) is as large as +8.2%, and the mismatch induced film stress is expected to be 16 GPa, which is very close to the film stress of 17 GPa we obtained from stress measurement between 1 ML and 2 ML, indicating that the pseudomorphic growth of fcc-Co lasts until 2 ML, similar to the case Ni films on Ir(100).

It has been proposed that bcc phases of Ni and Co can also be obtained by MBE. Experimentally, bcc-Ni thin films are prepared by epitaxial growth on Fe(100) [87, 88] and GaAs(100) [89], and the bcc-phase of Co is also obtained on GaAs(100) and Pt(100) [90]. Bcc-Ni in its equilibrium state is expected to have a lattice constant of $a \approx 2.79$ Å according to *ab initio* calculations [91–93], and the lattice constant in bcc-Ni on GaAs(100) is reported to be 2.82 Å. Experiments [78] and calculations [92] all indicate that the lattice constant of bcc-Co is about 2.82 Å. In the following I shall demonstrate that the bcc phases of Ni and Co do not agree with our results.

We take the elastic constants from *ab initio* calculations due to lack of experimental data and estimate the misfit induced film stress τ_F, the results are listed in Table 5.2.

Remarkably enough, the Young's modulus calculated from the elastic constants c_{ij} is negative. A negative Young's modulus means the lattice will undergo a tensile stress with a negative strain (lattice constant becomes smaller than the equilibrium state) and a compressive stress with a positive strain. However the lattice is deformed elastically, the film stress tends to enhance the deformation, indicating that the bcc-Ni and bcc-Co lattices are unstable once the lattice constant is forced to change. The authors of the calculation also pointed out the instability due to the negative shear modulus (defined as $\frac{1}{2}(c_{11}-c_{12})$), but did not comment on a negative Young's modulus. As shown in Table 5.2, if taking the elastic constants from calculations into consideration, the expected mismatch induced film stresses are also tensile, in line with the experimental observations for Ni and Co on Ir(100). However, the magnitudes of the estimated stresses fail to match the experimental results that are 15 GPa for Ni and 17 GPa for Co on Ir(100), therefore the bcc phase of Ni and Co crystal structure can be excluded.
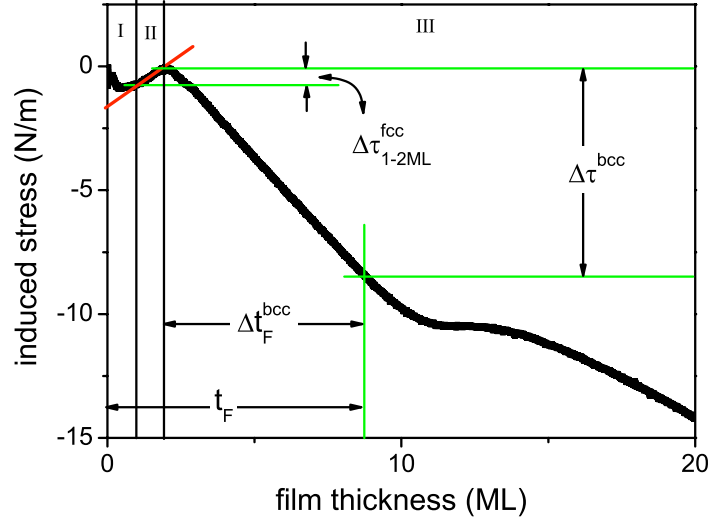
Figure 5.2: Interpretation of the film strain obtained from stress change for Fe monolayers on Ir(100)-(1×1) (see text).

b. Film strain and dislocations

As has been introduced in Section 4.1, pseudomorphic growth is observed for Fe, Ni and Co monolayers grown on Ir(100). Beyond pseudomorphic growth, the film strain is influenced by the occurrence of defects in the crystal as well as by the growth mode. As film thickness increases, it is more and more difficult to determine the inter-atomic distances by surface-analysis techniques such as LEED, so that the film strain as determined by diffraction techniques becomes less reliable.

However, the averaged stress ($\bar{\tau} = \Delta\tau/t_F$) reflects the strain throughout the whole film, and the in-plane film strain $\epsilon_{//}$ can be calculated as

$$\epsilon_{//} = \frac{1 - \nu_F}{Y_F} \bar{\tau} \tag{5.1}$$

in which $\bar{\tau}$ is averaged over the whole thickness range, thus an alternative way to extract strain, which does not rely on diffraction experiments, is possible.

For Ni and Co, strain can be conveniently obtained from the averaged stress change. For Fe on Ir(100), however, the situation is more complicated. As has been discussed in the previous part, the stress curve for Fe films reveals that the first two monolayers could be ascribed as a strained fcc-Fe lattice, which needs to be considered separately. It will not influence the strain for larger thickness, yet need to be accounted for in thinner films. Also, our magnetoelastic coupling coefficients measurements are performed for a few monolayers of Fe, hence it is worthwhile to discuss the strain layer by layer. As shown in Figure 5.2, the stress curve is divided into three regimes. In the submonolayer range, the stress change is responsible for the surface stress change but not the film stress in the first layer. From 1 ML to 2 ML, the positive slope suggests that a fcc-Fe lattice is formed, and the film strain can be calculated from the averaged stress change $\bar{\tau}^{fcc} = \Delta\tau^{fcc}_{1-2ML}/\Delta t^{fcc}_F$ using Equation 5.1. Over 2 ML, the film structure changes into bcc, and the film strain in the bcc-Fe layers is calculated with the relative stress change $\Delta\tau^{bcc}$ and thickness Δt^{bcc}_F. Both the 2 ML fcc-Fe and the bcc-Fe layers coexist, therefore
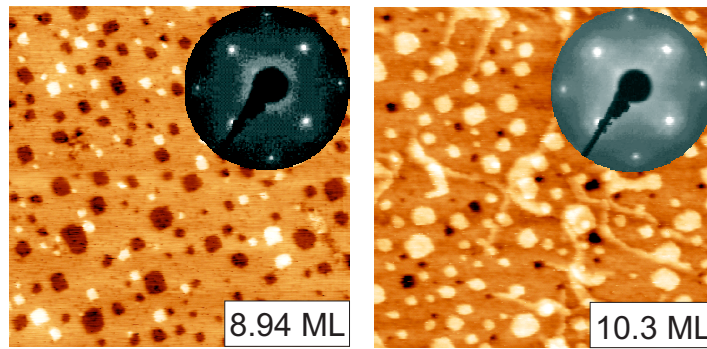
(a) STM images (1000Å×1000Å) for Fe films on Ir(100)-(1×1) from Ref. [94]. Extra feature (stripes) appears over 10 ML.
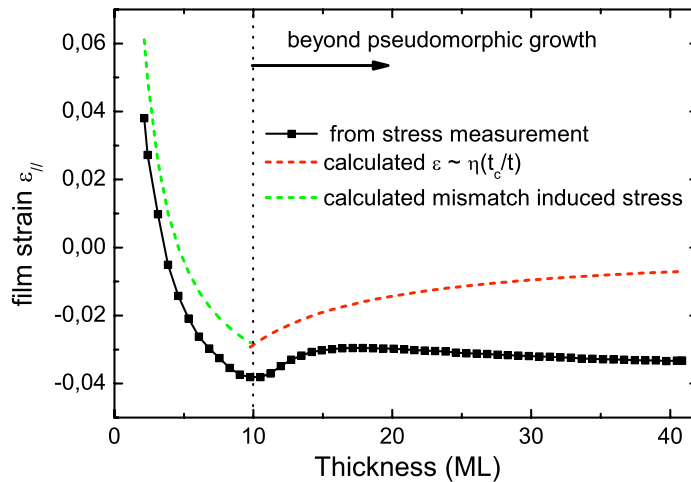
(b) Film strain of Fe/Ir(100)

Figure 5.3: STM images for Fe films on Ir(100)-(1×1) around 10 ML from Ref. [94]. Film strain obtained from stress measurement (black) and the calculation using dislocation model (red).

the film strain throughout the whole film is averaged as $\bar{\epsilon} = (\bar{\epsilon}^{fcc}\Delta t_F^{fcc} + \bar{\epsilon}^{bcc}\Delta t_F^{bcc})/t_F$, in which the averaged film strain for fcc-Fe and bcc-Fe layers are calculated separately using Equation 5.1 and the respective elastic moduli. Film strain obtained following these considerations is shown in Figure 5.3.

In the case of dislocation formation, according to Bruno [95], the film strain follows

$$\epsilon \sim \eta \frac{t_c}{t_F} \tag{5.2}$$

in which η is the mismatch strain and t_c is the critical thickness when dislocations start to appear. For Fe on Ir(100), the LEED images exhibit extra spots around original spots arising from dislocations when the thickness is more than 10 ML, as has been shown in Figure 4.2. The STM image of 10.3 ML Fe on Ir(100)-(1×1) also shows extra features that may come from the misfit dislocations (Figure 5.3(a)). These results point to a critical thickness t_c of 10 ML for Fe grown on Ir(100), corresponding to 8 ML bcc-Fe and 2 ML fcc-Fe. Additionally, the misfit strain for bcc Fe on Ir(100) is -5.3%, therefore according to Eqn. 5.2 the strain of the bcc-Fe layers beyond pseudomorphic growth should be $\epsilon \sim -0.053 \times 8/t_F^{bcc}$.

Film strain beyond pseudomorphic growth of Fe on Ir(100)-(1×1) from stress measurements and calculated strain using the dislocation-model is presented in Figure 5.3(b). The dislocation-model results in a totally relaxed film with $\epsilon \rightarrow 0$ when the thickness increases to infinite, while stress measurements reveal that a residual stress exists even when the thickness is more than 6 nm, and thus the residual film strain also should not be zero. (The film strain beyond pseudomorphic growth of Ni and Co on Ir(100) are shown in Section 5.1.3)

The satellite spots observed around the (00) spots and (01) spots in LEED images of Fe and Co films thicker than 10 ML can be ascribed to a dislocation network formation [96]. As the (00) diffraction spot is obtained with the reciprocal-lattice vectors $q_{//} = 0$ and $q_{\perp} \neq 0$, the satellite spots around (00) spot indicate a vertical lattice spacing modulation by the dislocation formation. In addition, the satellite spots around (01) show in-plane modulations by the dislocations. Therefore the dislocations formed in Fe and Co films result in a 3-dimensional structural modulation. Due to the multi-scattering nature of the LEED images, an in-depth qualitative analysis requires investigation for the spots intensity, and measurements with vanishing q are necessary (e.g., by X-ray diffraction). Nevertheless, a rough estimation by comparing the distance between the satellite spots and the primary (00) spot to the distance between two primary spots (e.g., (10) and (01)) reveals that the period of the modulation is about 5-6 atomic distances. The satellite spots around (10) spots are hardly distinguishable for thicker films, suggesting a worse long range periodicity of the dislocations. For LEED images of Ni monolayers on Ir(100), it is even more difficult to identify the satellite spots, suggesting a poor order of the long range periodicity.

The stress change in the film is also correlated with structural modifications such as dislocation formation and mesoscopic misfit changes. However, the quantitative analysis requires calculations and theoretical models. For Ni monolayers grown on Ir(100), the film stress is relaxed after 2 ML where pseudomorphic growth ends to less than half of the misfit induced stress. From 2 ML to 11 ML, slight modulations of the stress change are observed that imply fine structural modifications. STM studies reveal that Shockley partial dislocations appear for a Ni thickness of more than 2 ML [97], which relieve tensile stress in film [47]. Hence, the combination of stress measurement and STM work figures out the growth of Ni monolayers on Ir(100): fcc-Ni is formed with large tensile film stress of 15 GPa below 2 ML in pseudomorphic growth. As the thickness increases Shockley partial dislocation are formed to relieve the mismatch induced stress, the film stress is indeed considerably relaxed to 6 GPa in average and changes during the dislocation formation process.

Similar to Co films grown on Cu(100) [98], stress oscillations are also observed in epitaxial growth of Co on Ir(100), indicating the mesoscopic strain relaxation during island growth. For Co thickness $t_F \geq 3$ ML, the increase of integrated film stress $\Delta \tau_F t_F$ for less than half filled layer is smaller than for filled layers, and this oscillation extends to less than 6 ML (Figure 4.4(b)). As also indicated by the MEED oscillations up to 5 ML, the growth mode of Co on Ir(100) is layer-by-layer. However, the ad-atoms on a filled layer may form islands, as has been observed for Co films grown on Cu(100) [99]. The calculation of Sander and Stepanyuk et al. [98] indicates: the island-induced stress strongly depends on the island size, larger islands induce larger stress; the Cu substrate underneath Co islands exhibit a strong compressive stress while the outer atoms are under tensile stress; the island coalescence increases the tensile stress in the coalesced

islands and reduces the compressive stress in the Cu substrate. For Co films on Ir(100), the stress curve show smaller or even negative slope for less than half filled layer, which is ascribed to the relaxed stress within small islands, and the compressive stress underneath the islands; the larger tensile stress for more than half filled layer is ascribed to the coalescence of Co islands. It is notable that the misfit strain between fcc-Co and Ir(100) ($\eta = 8.2\%$) is much larger than the misfit strain for Co films grown on Cu(100) ($\eta = 1.7\%$), however, the relaxation of the tensile stress during islands growth is no less than on Cu(100) substrate, even a compressive stress change (negative slope of ~ 3.5 GPa) is observed, while on Cu(100) substrate only tensile stress is observed during the stress oscillations. Following the line of thought in the calculation, the Co islands on Ir(100) causes larger compressive stress in the substrate compared to that on Cu(100) despite of a larger misfit induced tensile stress.

5.1.2 The link between magnetism, magnetoelastic coupling and structure— as given by the coercivity

In micromagnetic theory, the coercivity of magnetic films with the magnetic field applied along an easy axis is described by a domain wall motion model [3]. The main factor that influences the motion of the domain walls and causes an increase of the coercivity is the pinning effect of the defects, such as dislocations and inhomogeneity of the magnetic properties . The coercivity H_c for Co monolayers on Ir(100) is shown in Figure 5.4, as deduced from MOKE measurements with the magnetic field parallel to Co(100)-[100]. The increase of H_c at about 5 ML can be understood with the domain wall pinning model [3]: when the domain wall thickness δ_{dw} exceeds the dimension of the defects D, the coercivity H_c is proportional to the normalized defect size $w = D/\delta_{dw}$; when $\delta_{dw} \ll D$, $H_c \sim \delta_{dw}/D$. The coercivity peaks around $D \approx \delta_{dw}$ ($w \approx 1$), which is found for hard magnetic materials (rare-earth transition metal borides) [100] and soft magnetic materials (cobalt rich amorphous alloys) [101]. For Co monolayers grown on Ir(100), pseudomorphic growth is observed below 2 ML, and a prototype layer-by-layer growth mode is found from 2 ML to less than 6 ML as discussed above. During the pseudomorphic growth, both LEED and stress measurement indicate a perfect Co layer, which means that the dimension of the defects are close to zero. From 2 ML to 5 ML (region(I)), it is reasonable to believe that the dimension of the defects increases with the thickness during the coalescence of the islands, therefore the coercivity increases with thickness as $H_c \sim D/\delta_{dw}$. The coercivity decreases after 5 ML until about 20 ML, which can be understood as the dimension of the defects exceeds the domain wall thickness so that $H_c \sim \delta_{dw}/D$ (region(II)-a). When D increases due to the end of layer-by-layer growth after 5 ML, H_c increases. Remarkably enough, a corresponding change in the experimental B_1^{eff} and B_2^{eff} is found at a thickness t_F above 5 ML (region(II)-a, b, c), e.g., when $10 < t_F < 40$ ML, $|B_i^{eff}|$ increases while H_c decreases with film thickness, and $|B_i^{eff}|$ decreases as H_c increases. After about 40 ML, both H_c and $|B_i^{eff}|$ stay constant.

In region II where $H_c \sim \delta_{dw}/D$, the change in the dimension of defects is supposed to saturate as the structural fluctuation normally will not increase dramatically. According to a uniaxial anisotropy assumption, the domain wall thickness δ_{dw} can be calculated from $\sqrt{A/K}$, with K being the anisotropy constant. The contribution of magnetoelastic
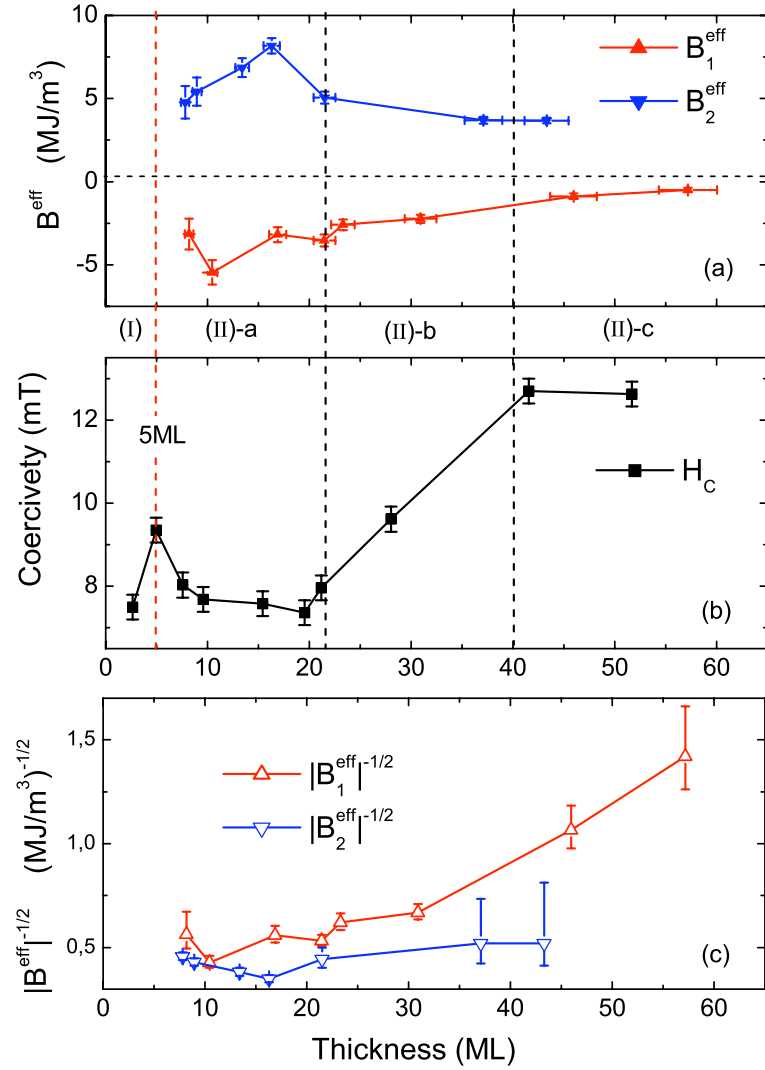
Figure 5.4: Comparison of the thickness dependence of (a), the effective magnetoelastic coefficient B_i^{eff} and (b), the coercivity H_c of Co monolayers on Ir(100). The thickness is divided into two main regimes: in region I the dimension of the defect is smaller than the domain wall thickness; in region II the domain wall thickness is smaller than the dimensions of the defects. (a) and (b) show the different thickness dependence of H_c and B_i^{eff} obtained from magnetoelastic stress measurement (see text), and (c) shows the value of $\sqrt{1/|B_i^{eff}|}$ is calculated from (a).

coupling to an magnetic anisotropy is of order $B_i\epsilon$. Therefore a $\sqrt{1/|B_i^{eff}|}$ dependence of δ_{dw} is expected when the change in ϵ is small. As the change of the film strain of Co on Ir(100) is rather small after about 15 ML, the focus is hence on $\sqrt{1/|B_i|}$. In Figure 5.4(c), the values of $\sqrt{1/|B_i^{eff}|}$ calculated from the experimental B_1^{eff} and B_2^{eff} are plotted with respect to the film thickness. Despite of the rough estimation, the thickness dependence of $\sqrt{1/|B_i^{eff}|}$ is qualitatively consistent with the behavior of H_c, in agreement with the expectation.

The pinning and motion of the domain walls in a magnetic film is very often a com-

plicated problem, in which many factors are involved such as the type of domain wall, structural and magnetic properties of the sample and the microscopic heterogeneity distribution. Nevertheless, the analysis based on the simple model can be used and gives a qualitative agreement. The importance of magnetoelastic coupling in micromagnetic problems is thus also demonstrated.

5.1.3 Strain dependent magnetoelastic coupling and its impact on magnetic anisotropy

In a bulk sample, the magnetostriction constant λ_i is proportional to the magnetoelastic coefficient B_i as given by Equation 2.7. Therefore, the bulk value of the magnetoelastic coefficient B_i can be obtained by measuring the magnetostriction constant in a bulk sample. In the past, the bulk values of B_i have been taken into account for an estimation of magnetoelastic energy and magnetic anisotropy energy not only for bulk samples but also for nano-size samples, such as ultrathin films. However, a significant difference for magnetoelastic coefficients at a surface as compared to bulk was found by O'Handley and co-workers [13]. Following Néel's model, this has been ascribed to a so called surface magnetoelastic coupling contribution, and the effective magnetoelastic coupling coefficient has been expressed as

$$B_{eff} = B_{bulk} + B_s/t \tag{5.3}$$

in which t is the film thickness. It has then been found by Koch [16] that B_1^{eff} of Fe films with same thickness may show different values when the film stress is modulated on various substrates, and this disagrees with the surface effect senario. Later, O'Handley [20] and Sander *et al.* [17] also found that the magnetoelastic coupling coefficients in thin films may dramatically differ from the bulk value, and suggested that film strain is a decisive factor for this deviation. More experimental results reveal that the effective magnetoelastic coupling coefficients may be strain-dependent rather than a surface effect. However, due to the complexity of the relation between strain and magnetic anisotropy, as well as the difficulties to measure the magnetoelastic coupling coefficients in a large strain range, the present experimental results are rather insufficient to provide a full understanding of the non bulk-like magnetoelastic coupling. In addition, the discrepancy between theoretical and experimental results are still under investigations. In this work, the magnetoelastic coefficients B_1^{eff} and B_2^{eff} of Fe, Co and Ni are obtained by magnetoelastic stress measurements, and the values will be compared to theoretical results.

Beyond the linear approximation the expression of ME energy density is expanded as $f_{ME} = f_{ME}^{(1)} + f_{ME}^{(2)} + \cdots$, in which the higher orders of strain tensor components ϵ_{ij} are included. The idea of this expansion is given in Ref. [102] based on a phenomenological theory of nonlinear magnetoelasticity and is simplified by limiting the expansion to the quadratic harmonic polynomials in α_i in this model [23]:

$$f_{ME}^{(1)} = B_1(\epsilon_{11}\alpha_1^2 + \epsilon_{22}\alpha_2^2 + \epsilon_{33}\alpha_3^2) + 2B_2(\epsilon_{12}\alpha_1\alpha_2 + \epsilon_{23}\alpha_2\alpha_3 + \epsilon_{31}\alpha_3\alpha_1) \tag{5.4}$$

$$f_{ME}^{(2)} = \frac{1}{2}(B_1 + m_1^{\gamma,2})(\epsilon_{11}^2\alpha_1^2 + \epsilon_{22}^2\alpha_2^2 + \epsilon_{33}^2\alpha_3^2) + \frac{1}{2}m_2^{\gamma,2}(\epsilon_{11}\epsilon_{22}\alpha_3^2 + cycl.)$$

Table 5.3: Magnetoelastic coefficients B_i, $m_i^{\gamma,2}$, $m_i^{\epsilon,2}$ (in MJ/m^3) and elastic constants C_{ij} (in 10^{11} N/m^2) from ab initio calculation [93, 103]

		B_1	B_2	$m_1^{\gamma,2}$	$m_2^{\gamma,2}$	$m_1^{\epsilon,2}$	$m_2^{\epsilon,2}$	$m_3^{\gamma,2}$	$m_3^{\epsilon,2}$	C_{11}	C_{12}
fcc Co	LSDA	-15.9	3	243	-53	81	102	795	796	3.85	2.26
	GGA	-9.8	4.5	184	3	59	-41	862	1681	3.13	1.8
fcc Ni	LSDA	12.6	16.9	-117	23	168	-47	-2	388	3.63	2.2
	GGA	10.2	11.1	-95	71	90	-4	108	96	2.95	1.75
bcc Fe	LSDA	-10.1	-7.0	322	84	-25	-48	-11	-77		
	GGA	-2.4	-3.9	315	126	111	81	-463	-868		

$$+\frac{1}{2}(m_3^{\gamma,2} - B_1) \times (\epsilon_{12}^2 \alpha_3^2 + cycl.) + m_1^{\epsilon,2}(\epsilon_{11}\epsilon_{23}\alpha_2\alpha_3 + cycl.)$$

$$+(B_2 + m_2^{\epsilon,2})\left[(\epsilon_{11} + \epsilon_{22})\epsilon_{12}\alpha_1\alpha_2 + cycl.\right]$$

$$+(B_2 + m_3^{\epsilon,2})(\epsilon_{12}\epsilon_{23}\alpha_1\alpha_3 + cycl.) \tag{5.5}$$

In these expressions B_1 and B_2 are the first-order ME coefficients. The second-order ME coefficients, $(m_1^{\gamma,2}, m_2^{\gamma,2}, m_1^{\epsilon,2}, m_2^{\epsilon,2}, m_3^{\gamma,2}, m_3^{\epsilon,2})$, $(m_1^{\gamma,2}, m_2^{\gamma,2})$ are related to pure tensile strains, $(m_1^{\epsilon,2}, m_2^{\epsilon,2})$ to tensile and shear strains, $(m_3^{\gamma,2}, m_3^{\epsilon,2})$ to pure shear strain.

The concept to measure the ME coefficients by ME stress measurements has been introduced in Sec. 2.4: the magnetization is switched between certain directions, and the magnetoelastic coupling induced stress change during the process is related to the ME coefficients according to the geometry of the measurement. The calculations proposed six geometries with which the ME coefficients can be obtained by ME stress measurements [23]. In practice, the ME stress measurements are limited by the geometry of the external magnets, i. e. the magnetic fields necessary to force the magnetization along a given direction. For example, the magnetic field is normally applied along two orthogonal directions and it is very often that the magnetization cannot be saturated along the hard axis. Therefore it is very difficult to achieve all proposed geometries.

Under this situation, the measurements on effective ME coefficients B_i^{eff} by measuring the magnetoelastic stress difference do not give directly the second-order ME coefficients as defined above, but the combination with first-order ME coefficients and elastic constants. According to the geometries of the ME stress measurements taken in this work, the expression of B_i^{eff} in terms of the magnetoelastic coefficients in Equation 5.5 is as follows:

$$B_1^{eff} = B_1 + D_1\epsilon_{//}, \quad D_1 = B_1 + m_1^{\gamma,2} + \frac{c_{12}}{c_{11}}m_2^{\gamma,2}$$

$$B_2^{eff}(\epsilon) = B_2 + 2D_2\epsilon_{//}, \quad D_2 = \frac{1}{2}\left[(B_2 + m_2^{\epsilon,2}) - \frac{c_{12}}{c_{11}}m_1^{\epsilon,2}\right].$$

Here the in-plane film strain is taken as homogeneous, with $\epsilon_{11} = \epsilon_{22} = \epsilon_{//}$, and the out-of-plane strain follows as $\epsilon_{\perp} = -2\frac{c_{12}}{c_{11}}\epsilon_{//}$. Together with Equation 5.4 and 5.5, the relation between magnetoelastic energy and film strain is a parabola considering both

the first and the second order strain contribution, and the higher orders may lead to more complicated curves [11,93] with non-monotonic behavior.

The relation between our experimentally determined B_i^{eff} and $\epsilon_{//}$ is fitted with a linear relation for Fe, Co and Ni thin films on Ir(100), the results are as follows:

(bcc-Fe with negative film strain)

$$B_1^{eff} = -3.6\ (\pm1.0)\frac{\text{MJ}}{\text{m}^3} + 155\ (\pm37)\frac{\text{MJ}}{\text{m}^3} \cdot \epsilon_{\parallel}$$

(fcc-Co with positive film strain)

$$B_1^{eff} = 3.5\ (\pm0.7)\frac{\text{MJ}}{\text{m}^3} - 842\ (\pm126)\frac{\text{MJ}}{\text{m}^3}\cdot\epsilon_{\parallel} \qquad B_2^{eff} = 1.8\ (\pm1.3)\frac{\text{MJ}}{\text{m}^3} + 930\ (\pm195)\frac{\text{MJ}}{\text{m}^3}\cdot\epsilon_{\parallel}$$

(fcc-Ni with positive film strain)

$$B_1^{eff} = 1.3\ (\pm1.0)\frac{\text{MJ}}{\text{m}^3} + 273\ (\pm197)\frac{\text{MJ}}{\text{m}^3}\cdot\epsilon_{\parallel} \qquad B_2^{eff} = 6.6\ (\pm1.0)\frac{\text{MJ}}{\text{m}^3} - 408\ (\pm107)\frac{\text{MJ}}{\text{m}^3}\cdot\epsilon_{\parallel}$$

The comparison between this study and the calculations using LSDA and GGA methods is listed in Table 5.4, previous experimental determinations [16, 17, 25] are also summarized therein. The effective value B_4^{eff} of hcp-Co on W(100) has been studied [104], but the strain dependence of B_1^{eff} and B_2^{eff} for fcc Co as well as B_2^{eff} for fcc-Ni have not been obtained before. The values of B_1^{eff} for bcc-Fe with negative strain are also measured for the first time. For the other ME stress experiments listed in the table, as the value of B_i^{eff} may deviate from the simple linear-fitting $B_i^{eff} = B_i + D_i\epsilon_{//}$ dramatically in a larger strain range and the linear-fitting close to zero strain are forced to go through the bulk value of B_i. In this study we fitted all the data obtained by ME stress measurement without forcing the bulk value for zero strain, knowing that the linear fitting of the strain dependent B_i^{eff} considers only first- and second- order terms, and the higher order terms may also play an important role [93]. The values of B_i and D_i are obtained from least-square fitting of the experimentally determined of B_i^{eff} and $\epsilon_{//}$, as presented in the previous chapter.

The first-order ME coefficients B_i we obtained have the same sign as the other experimental and theoretical results, except for B_1 of fcc-Co. Considering that the B_i values we obtained are actually the extrapolation to zero strain without forcing the linear-fitting go through the bulk value, this agreement is already quite impressive. However, the linear fitting is based on the phenomenological strain-dependence model considering up to the second-order strain contribution, it may not be able to describe the whole strain range, and the bulk value can be obtained only when the strain approaches to zero, therefore the extrapolation to $\epsilon = 0$ may not correspond to the bulk value. Comparing B_1 and D_1 for bcc-Fe with negative strain ($\epsilon_{\parallel}$ between -1% and -4%) to the previous experimental results for bcc-Fe under positive strain, one finds that the values of B_1 are almost the same, while D_1 is quite different. This indicates that the strain dependence of B_i is not the same for positive and negative strain, which is in line with the non-monotonic behavior of magnetic anisotropy energy corresponding to the lattice distortion. For the same reason, the opposite sign of D_1 for fcc-Ni on Cu(100) [17] ($\epsilon_{\parallel}$ between 1%-2.5%) and Ir(100) (this study, $\epsilon_{\parallel} \sim 0.4\%$-0.7%) may also be understood. Therefore, the bulk values of B_i do not apply for a sample with strain, and it is also

Table 5.4: Theoretical (adapted from Table 5.3) and experimental results of magnetoelastic coupling coefficients B_i and the non-linear strain dependence D_i. (The values are in unit of MJ/m^3.)

		B_1	D_1	B_2	$2D_2$
fcc Co	LSDA	-15.9	212	3	58
	GGA	-9.8	186	4.5	-71
	Exp.[1]	-9.2	—	7.7	—
	This study (positive strain)	3.5	-842	1.8	930
fcc Ni	LSDA	12.6	-103	16.9	-132
	GGA	10.2	-53	11.1	-47
	Exp.[2]	9.4	-234	10	—
	This study (positive strain)	1.3	273	6.6	-408
bcc Fe	LSDA	-10.1	337	-7.0	-40
	GGA	-2.4	383	-3.9	18
	Exp.[3]	-3.4	1100	7.8	-365
	This study[4] (negative strain)	-3.6	155	—	—

[1]The experimental value of first-order ME coefficients B_1, B_2 of fcc Co is calculated from the magnetostriction constant λ_{100} and λ_{111} that are extrapolated from measurements on PdCo alloys, from Ref. [25]. [2]Experimental data B_1, D_1 of fcc Ni are from Ref. [17] for Ni/Cu(100) with positive film strain. [3]The experimental data B_1, B_2, D_1 and D_2 of Fe are from Ref. [16] for Fe(001)/MgO(001) and Fe/Cr/MgO(001) with positive film strain, in which the Fe films are deposited at different temperature to obtain different film strain. [4]B_2^{eff} of bcc-Fe has been measured, see Fig.4.16, but the scatter of the data does not allow for a description in terms of $B_2 = B_2(\epsilon)$.

required to take B_i^{eff} from a different strain range to describe magnetoelastic effects properly.

The B_2^{eff} of Fe measured in this study does not show a clear strain dependence. The data show a large scatter, and they all fall into the range of $+0.1 - +3.8$ MJ/m^3. However, the values are of the same sign (positive) as the experimental value obtained on MgO(100) with negative film strain. This is of the opposite sign as compared to calculations (both LSDA and GGA). This disagreement between experiment and calculations on B_2 has been discussed before [23] : the most frequently used approximation methods are deficient for the calculation of the magnetoelastic properties of Fe; the former experimental determinations of B_2 for Fe is probably doubtful as the Fe crystal used in the experiment is doped with Si which may change the d-band filling, therefore the experimental determinations should be taken with caution.

The strain dependence D_i of the ME coefficients is non-exceptionally 2-3 orders of magnitude larger than the first-order ME coefficients B_i, hence a very small strain may cause large changes of the effective ME coefficient B_i^{eff}. Unfortunately, the experimental determinations of the non-linearity of ME coefficients are quite limited and sometimes vary from case to case. This may be due to the difficulty to determine the film strain, which is normally obtained from the averaged film stress using $\tau = \frac{Y}{(1-\nu)}\epsilon$. However, the shear stress is not taken into consideration, which have a different relation
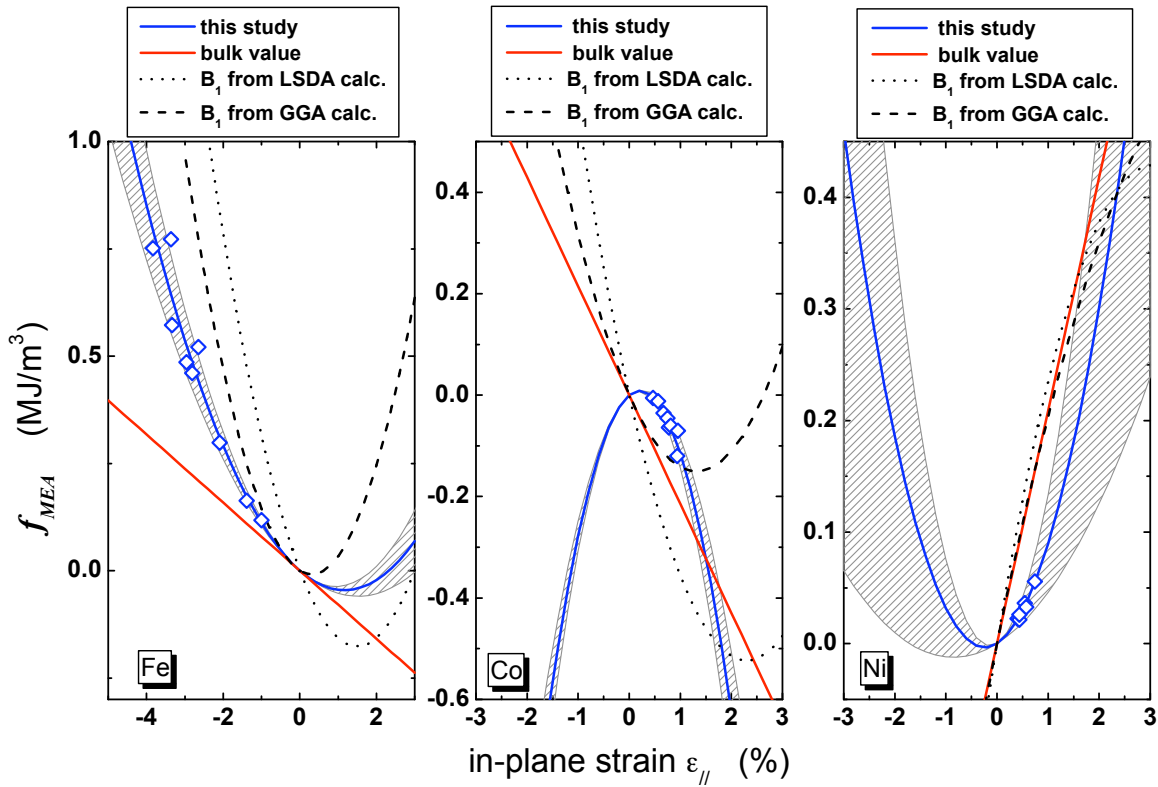
Figure 5.5: Magnetoelastic anisotropy for an out-of-plane magnetization direction of Fe(001), Co(001) and Ni(001) films. The blue hollow dots are calculated directly from the magnetoelastic stress measurement; the blue solid curve is from the linear fitting of B_1^{eff} obtained from experiment, and the uncertainty caused by the error-bar of the linear fitting is indicated as the shadowed area. The red solid line is calculated with the bulk value—i.e. a constant magnetoelastic coupling—giving rise to a linear magnetoelastic anisotropy contribution; the dashed and doted black curves represent the magnetoelastic anisotropy based on B_1^{eff} from *ab initio* calculation by GGA and LSDA, respectively, considering the second-order strain contribution to the magnetoelastic anisotropy. The GGA and LSDA data are taken from Ref. [93, 103].

with strain as $\tau_{ij} = 2G\epsilon_{ij}$ ($i \neq j$, $G = Y/2(1 + \nu)$ is the shear modulus). The shear strain might appear near misfit dislocations. It is almost impossible to distinguish shear stress from tensile stress only by stress measurement. In addition, film stress can also be influenced by other factors such as grain boundaries, and the linear relation between strain and stress is no longer sufficient. The relation between stress and strain in thin films beyond pseudomorphic growth still needs further studies. Due to the lack of a more sophisticated strain analysis, we took the simple proportionality between stress and strain for the sake of simplicity. It has been proved by previous experiments that this treatment works well for ultra-thin films of a few monolayers [25], and may deviate for higher thicknesses depending on growth conditions. For these reasons, the linear fitting is performed separately for B_2^{eff} of fcc-Co on Ir(100) (Figure 4.13), which shows a different strain dependence for a film thickness larger and less than 20 ML corresponding to the film strain of ∼0.8%.

Furthermore, with the effective ME coefficients B_i^{eff}, magnetoelastic anisotropy can

be calculated from Eqn. 5.4. The magnetoelastic anisotropy f_{ME} of (001) film for out-of-plane magnetization direction is

$$f_{ME} = B_1^{eff}(\epsilon_\parallel - \epsilon_\perp)$$

in which $\epsilon_\parallel$ and $\epsilon_\perp$ are in-plane strain and out-of-plane strain of the magnetic films, which are linked by $\epsilon_\perp = -2\frac{c_{12}}{c_{11}}\epsilon_\parallel$, assuming a homogeneous in-plane strain. The strain dependent magnetoelastic anisotropy curves of Fe, Co and Ni films are shown in Figure 5.5. They were calculated using B_1^{eff} from experiment and calculations.

As shown in Figure 5.5, our study indicates that the positive value of the magnetoelastic anisotropy for bcc-Fe(001) and fcc-Ni(001) films will contribute to the out-of-plane anisotropy and may give rise to a perpendicular magnetization easy axis, but for fcc-Co(001) films the magnetoelastic anisotropy energy is always negative, and this will prefer an in-plane easy axis. For bcc Fe, the experimental and theoretical results reflect the same tendency, especially in the negative strain range where the measurements were taken. Interestingly, though the sign of B_i and D_i for Co and Ni is different for experimental results and the calculations, the values of f_{ME} are not much different in the strain range of Co and Ni on Ir(100) investigated here. Taking the error-bar for the linear fitting of strain dependent B_i^{eff} into consideration, the uncertainty of the magnetoelastic anisotropy is also estimated and it is shown in the graph as the shadowed area. The errorbar of the second-order magnetoelastic coefficient D_1 causes a dominating uncertainty of f_{ME} for large film strain, as it is orders of magnitude larger than the first-order coefficient B_1.

Note, that in the strain range we studied, the calculated magnetoelastic anisotropy energy (hollow squares) does not deviate significantly from the curves obtained using B_1^{eff} from *ab initio* calculation considering the second-order, especially close to the results of GGA calculation (dashed lines). However, the opening of the parabola are opposite for Ni and Co, which is due to the opposite sign of D_1, as derived from for experiment and theory. As has been mentioned above, the estimations consider only the first- and second-order terms of the strain tensors for magnetoelastic energy, higher orders in strain are not considered. Nevertheless, it is likely that for larger film strain the higher orders cannot be neglected for Ni and Co, and the magnetoelastic energy expressed as quadratic polynomials is a poor approximation.

Out-of-plane anisotropy is defined as the magnetic energy difference between the in-plane magnetization state and out-of-plane magnetization state: $f_{MA} = f_\rightarrow - f_\uparrow$. With $f_{MA} > 0$, the magnetization prefers an out-of-plane direction, the easy axis is then along the perpendicular direction; with $f_{MA} < 0$ the easy magnetization direction is in-plane. The main contributions to the magnetic anisotropy are the shape anisotropy, magnetoelastic anisotropy and magnetocrystalline anisotropy $f_{MA} = f_{shape} + f_{ME} + f_{MC}$. In the cubic systems the [001] axis is equivalent to [100] and [010], and the magnetocrystalline anisotropy is normally much smaller than the shape anisotropy and the magnetoelastic anisotropy in the thin films, therefore we consider only the shape anisotropy and magnetoelastic anisotropy for the sake of simplicity.

Note that the simulations are based on the following assumptions:

- The magnetic moment of a bulk sample is used and the possible enhancement of the magnetic moment at surface/interface is not considered.

- Shape anisotropy is considered.

- Surface anisotropies are not considered.

- The elastic coefficients are given by bulk values.

In the following I discuss the validity of these approximations.

It has been found that the magnetic moment is enhanced at the surface as compared to the bulk, and this is ascribed to the reduced coordination and resulting band narrowing [105]. The calculated results (Ref. [106] and references therein) of ab initio methods predict an enhancement of 30% for magnetic moments of bcc-Fe(001) at the surface comparing to that in the center layer, 23% for fcc-Ni(100) and 13% for fcc-Co(100). This phenomenon is also observed at surfaces as well as interfaces experimentally [107, 108]. However, within the sensitivity of our MOKE measurement (Section 4.2, Figure 4.8(b), 4.11 and 4.14), there is no indication of magnetic moment enhancement for the magnetic monolayers on Ir(100) as the M_s signal extrapolated to zero for Ni and Co, and Fe films suffers from the Curie temperature effect. Moreover, the enhancement of magnetic moment for surface atoms will be averaged out with increasing film thickness, e.g. the averaged enhancement for 10 ML Fe(100) is 3% (for 30% enhancement at the surface). Therefore the possible moment enhancement in surfaces or interfaces are not accounted for.

According to Néel's original definition [109], surfaces anisotropies in thin films are due to the symmetry loss at the surface or interface. This gives a constant contribution of the anisotropy. The magnitude of the surface anisotropy constant K_s is predicted to be of the order 0.1 to 1×10^{-3} J/m^2. Usually K_s is extracted from a $1/t_F$ (t_F is the film thickness) fit of the thickness dependence of the magnetic anisotropy [9]. An example is Ni on Cu(100), where K_s/1 ML=-80 μeV (≈ 1 MJ/m^3) is obtained, which is dramatically large compared to the shape anisotropy of ≈ 0.15 MJ/m^3 for Ni thin films. However, K_s obtained from this fit disregards the contribution of the magnetoelastic anisotropy and its deviation from the bulk value, due to lattice strain. A quantitative prediction of K_s is rather empirical [105], and a high precision structural analysis of the real system is necessary for *ab inito* calculations. Due to the above reasons, the so called surface anisotropy is not considered in the following analysis.

It is surprising that the bulk reference data on both lattice spacing and elastic constants should also work for monolayers. However, our stress measurement presented here and previous work on other systems provide compelling evidence that continuum elasticity can provide very reasonable description of film stress and layer relaxation for pseudomorphic films thicker than 2 ML [98, 110]. The use of elastic constants of the film taken from bulk values appears to be a good and valid approximation. Therefore the bulk values of the elastic constants are applied for the estimations of the magnetoelastic anisotropy, and the results are discussed in the following.

Among the three most common ferromagnetic transition metals Fe, Co and Ni, bulk Ni has the lowest Curie temperature of 627 K and the smallest magnetic moment of 0.62 μ_B. The easy axis of bulk Ni is along [111] . During the last two decades, magnetic anisotropy of fcc-Ni films grown on Cu(001) was intensively studied for the unusual spin reorientation from in-plane to out-of-plane happened at around 7-12 ML [9, 10].

The strain dependent magnetic anisotropy curves for Ni films are shown in Figure 5.6 according to the above description. The estimation based on the linear strain dependence of B_1^{eff} from our measurements suggests that the magnetic easy axis is out-of-plane with positive film strain larger than 1.35%, or the absolute value of negative
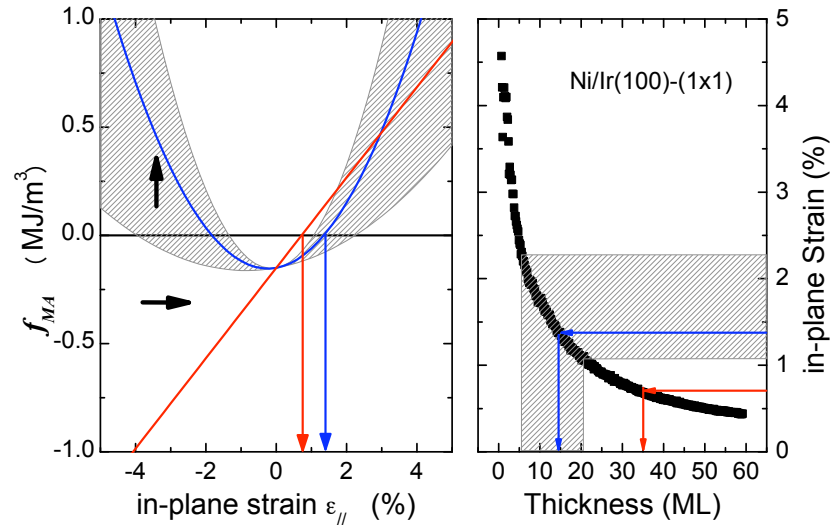
Figure 5.6: Comparison of the magnetic anisotropy energy ($f_{MA} = f_{\rightarrow} - f_{\uparrow}$) and the in-plane strain from stress measurement for Ni monolayers on Ir(100). The magnetic anisotropy is calculated considering shape anisotropy (using M_s of bulk value) and magnetoelastic anisotropy. The blue curve shows the magnetic anisotropy with strain dependent B_1^{eff} obtained from our experimental results, and the red curve takes the constant bulk value of B_1. Accordingly, the film strain and thickness where a spin reorientation may occur is marked by the blue and red arrows, respectively. The uncertainty caused by the error-bar in the linear fitting is indicated as the shadowed area.

film strain larger than 1.8% ($\epsilon_{//} < -1.8\%$). Our stress measurement during deposition of Ni on Ir(100) indicate that the pseudomorphic growth of fcc Ni stops after 2 ML, the film strain during pseudomorphic growth is 7.1%, as calculated from the film stress of 15 GPa. Beyond pseudomorphic growth the average film strain is shown in Figure 5.6. According to this strain-thickness curve, the estimation of the magnetic anisotropy suggests a spin reorientation transition at about 15 ML. (Due to the uncertainty in the magnetoelastic anisotropy, the possible thickness range is within 6-21 ML.) However, the magnetic anisotropy estimated using constant bulk value of B_1 predicts that the spin reorientation occurs at $\epsilon_{//} \sim 0.7\%$, corresponding to film thickness of about 35 ML. MOKE measurements tell that the easy axis is out-of-plane for Ni films between 7 ML to about 15-18 ML, where a spin reorientation occurs and the easy axis change to in-plane for thicker Ni films. This is in contrast to the estimation using bulk value of B_1, and this result suggests a validity of a strain dependent B_1^{eff}.

Similarly, the magnetic anisotropies for Co(001) and Fe(001) monolayers on Ir(100) are also analyzed. For Co monolayers on Ir(100), the estimations using ME coefficients from our measurement suggest that no out-of-plane easy axis appears since f_{MA} is negative, though the film strain during pseudomorphic growth is as large as +8.5%. Our MOKE measurements indicate that the easy magnetic axis is in plane from 2 ML up to a few nanometers, and no perpendicular magnetization is observed. For Fe(001) films on Ir(001), the film strain is about $-4.0\% < \epsilon < 4.0\%$ and in-plane easy axis is expected in the strain range of $-6.3\% < \epsilon < 8.7\%$ according to the estimation with the same idea. Therefore an in-plane magnetization easy axis is expected. Indeed, MOKE measurements show an in-plane magnetization from 4 ML (at LT) to a few nanometers
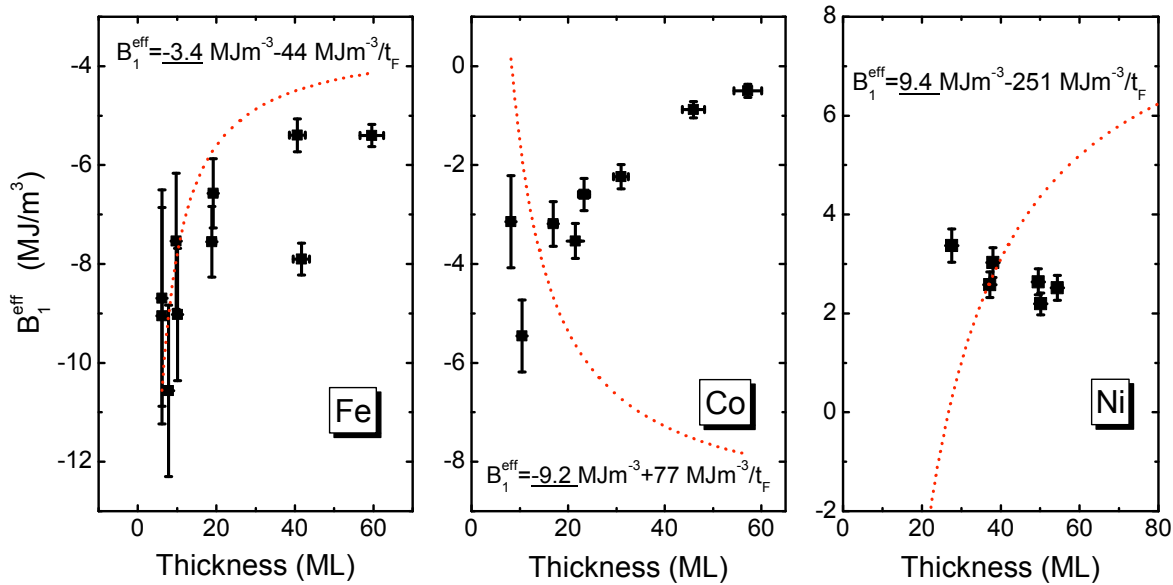
Figure 5.7: Experimental results (squares) of the effective magnetoelastic coupling co-efficients B_1^{eff} are fitted with $B_1^{eff} = \underline{B_1^{bulk}} + B_s/t_F$. The fit are shown as dotted red lines. The experimental B_1^{eff} of thicker Fe films deviates from the fitting, and B_1^{eff} of Co and Ni films cannot be described by the fitting over the whole thickness range. The strain dependance of B_1^{eff} gives a better description of the variation of B_1^{eff}, as shown in Section 4.2 above.

at RT, in agreement with the estimation based on a linear strain dependence of B_1^{eff}.

In conclusion, for Fe, Co and Ni monolayers on Ir(100), our estimation for easy the magnetization direction based on B_i^{eff} obtained from ME stress measurement agrees well with the MOKE measurement, and no further anisotropy contributions need to be included (such as, e.g. so called surface anisotropy).

The surface magnetoelastic coupling model

The strain-dependent magnetoelastic coupling discussed above agrees quite well with the observed out-of-plane magnetization. Although the linear relation between the effective magnetoelastic coupling coefficients may properly describe the strain dependence in the strain range being explored, it seems to be insufficient to describe the whole strain range, as some of the fitting curves do not extrapolate to the bulk values for vanishing strain. The reason is still not clear. Hence the surface contribution model is also considered here to see whether it may give a better description.

According to the surface contribution model, B_1^{eff} is separated into bulk value B_1^{bulk} and surface magnetoelastic coupling contribution that shows a $1/t$ dependence. The experimental value of B_1^{eff} is hence fitted with the expression of $B_1^{eff} = B_1^{bulk} + B_s/t_F$. For this fitting, the value of B_1^{eff} should go to the bulk value with infinite film thickness t_F. As shown in Figure 5.7, the fitting is much worse than the strain-dependent fittings as presented in Section 4.2, especially for B_1^{eff} of Co and Ni films. Therefore it will not give a better description of the effective magnetoelastic coupling coefficients.

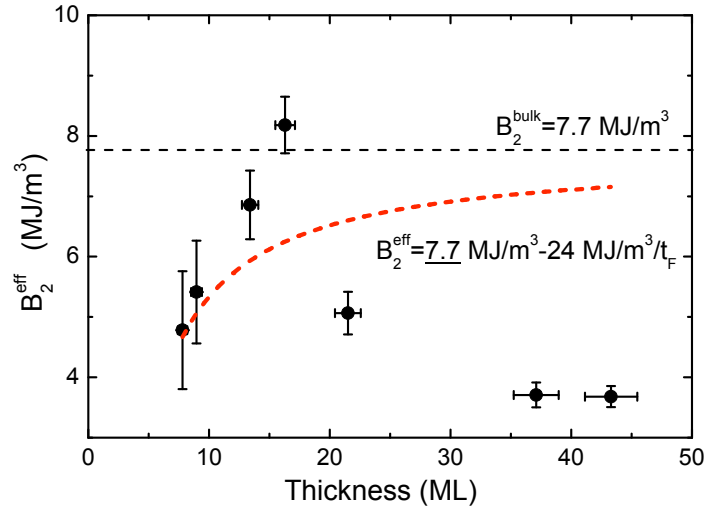For B_2^{eff} of Co films, the linear strain-dependence of B_2^{eff} does not give a satisfac-

Figure 5.8: Curve fitting (red dash line) of the experimental B_2^{eff} of Co films with $B_2^{eff} = B_2^{bulk} + B_s/t_F$ with $B_2^{bulk} = 7.7$ MJ/m^3. The B_2^{eff} are obtained from magnetoelastic stress measurement. The surface contribution model is not able to fit the experimental values of B_2^{eff}.

tory description of the experimental values, therefore the surface contribution model is applied as shown in Figure 5.8. The curve fitting is quite poor, and it is also not able to fit the experimental values.

The above comparisons suggest that the surface contribution model is less accurate in describing the effective magnetoelastic coupling coefficients in magnetic monolayers, as compared to a strain dependence of B_i^{eff}.

5.2   Influence of surface stress on surface structures

5.2.1   The role of surface stress in surface reconstruction

Surface stress plays an important role in surface reconstruction, especially when the atomic density is changed during the reconstruction [111]. For solid surface, the thermodynamic driving force to change the atomic density of the surface is considered to be $(\tau_s - \gamma)$ [112, 113], the difference between surface stress τ_s and surface specific free energy γ. With $(\tau_s - \gamma) > 0$, the surface has the tendency to have more atoms in the surface layer and when $(\tau_s - \gamma) < 0$ it prefers to a lower atomic density. In addition, to change the atomic density of the surface layer, more energy is needed to compensate the energy cost considering the following important effects [112]:

- the interactions related with breaking the surface-substrate bonding;

- the energy cost or gain of removing atoms from or to the surface layer;

- the energy difference in the bonds between the surface layer and the substrate underneath.

Clean metal surfaces normally show tensile surface stress [114, 115]. This is ascribed to the lack of nearest neighbors for the surface layer, the intra-layer bonding is then enhanced to accommodate the redistributed charge. Similar to the other fcc 5d metals Pt and Au, the clean Ir(100) surface exhibits a quasi-hexagonal reconstruction—Ir(100)-(5×1)Hex. The surface reconstruction from a clean fcc-Ir(100) surface to the (5×1)Hex surface increases the surface atomic density. 20% extra atoms are accommodated in the topmost layer. Ir atoms are closely packed to a quasi-hexagonal structure (Figure 3.9(a)). As a simple estimation considering only the mismatch between the top most layer and the underlayer, the (5×1)Hex surface is taken as a quasi-hexagonal atomic arrangement of the outermost layer as (111) face. The stress difference between this highly densed layer and the (1×1) surface is calculated naively considering a (111) layer accommodated on (1×1) substrate, with anisotropic in-plane strain to be $\epsilon_1 = 0$ and $\epsilon_2 = -3.8\%$, and the resulting anisotropic stress are expected to be $\tau_1 = -0.68$ GPa and $\tau_2 = -2.4$ GPa according to elasticity (Equation 5.6). Therefore the averaged in-plane stress is $\frac{1}{2}(\tau_1 + \tau_2)d_{12} = -0.35$ N/m, with d_{12} being the lattice spacing (~ 2.25 Å) between the outermost two layers determined by LEED analysis. This estimation suggests that the tensile stress of (1×1) surface may be changed to a compressive stress due to the higher density of the Hex surface.

Indirect experimental evidence for stress relief in the reconstruction was obtained for the Ir(100) surface [116], and the authors in this work propose that surface stress is the driving force for the surface reconstruction of Ir(100)-(5×1) to Ir(100)-(5×1). However, *ab-initio* calculation [117] suggests that although the tensile stress of Ir(100) surface is large, the $(\tau_s - \gamma)$ is too small to be the driving force for the reconstruction to a surface with higher surface atom density [111], unlike for Au(100) and Pt(100).

The reconstructed quasi-hexagonal phase is not stable when adatom-adsorption is beyond a critical coverage. Upon H exposure, the surface reconstruction changes from Ir(100)-(5×1)Hex to Ir(100)-(5×1)-H [74], and the surface atomic density is greatly reduced. The 20% extra atoms are lifted up to form mono-atomic rows on the fcc-(1×1)
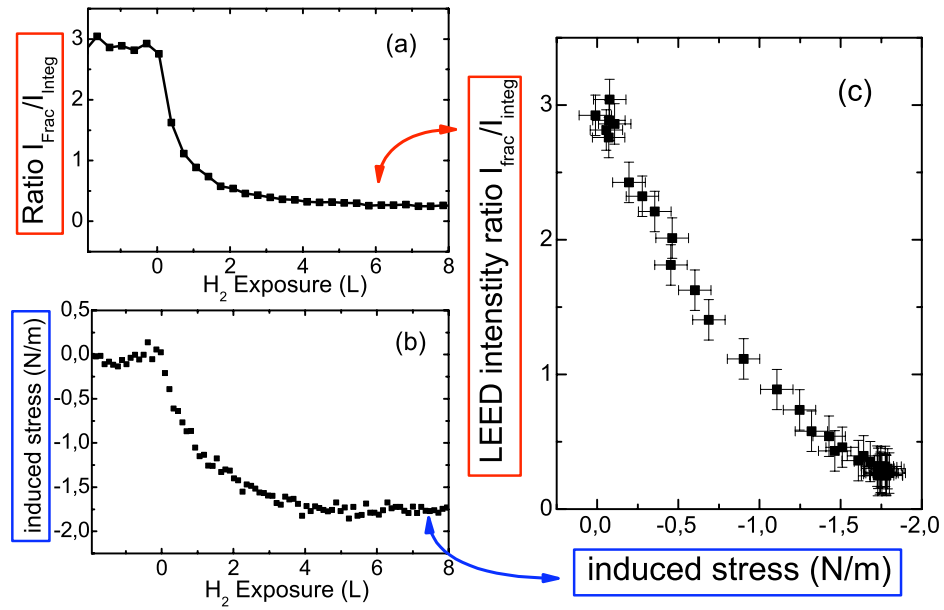
Figure 5.9: The H-adsorption induced stress change and the LEED intensity ratio I_{frac}/I_{integ} upon the same amount of H exposure are ploted as X and Y to show the relation between stress change and the structural change.

restructured substrates with a dominant period of 5 times of the Ir substrate lattice constant. For the adsorbate covered surface, both surface stress and surface free energy may be quite different from those of the clean surface. For this reason, the adsorbate covered surface should be treated as a new surface, and the driving force for surface reconstruction also need to be reconsidered accordingly.

The surface stress change and structural evolution during H-induced surface reconstruction on Ir(100)-(5×1)Hex are presented in Section 4.3. Compressive stress change of −1.7 N/m is induced as shown in Figure 4.17. As can be seen from the LEED images for both (5×1)Hex and (5×1)-H surfaces, there are two orthogonal structure domains in coexistence. STM studies show the size of these domains are as large as hundreds of nanometers, suggesting the influence of the structure domains is not dramatic.

The compressive stress change observed during the H-induced surface reconstruction on Ir(100) can be understood with the scenario similar to the surface stress change for hydrogen adsorption on Pt(111) [118]. The "effective medium model" indicate that the tensile stress at a clean surface is due to lack of nearest neighbors comparing to the bulk layers, therefore the adatoms should reduce the tensile stress by restoring the missing charge. This qualitative model can be also used for Ir(100)-(5×1)Hex surface, where a relaxation of the tensile stress is induced by hydrogen adsorption.

It is not necessary that the stress change is accompanied with surface reconstructions as hydrogen adsorption itself may induce a compressive stress change. For example, calculations show that the hydrogen coverage on Pt(111) will reduce the tensile stress of clean Pt(111) surface. However, for hydrogen adsorption on Ir(100)-(5×1)Hex surface, a direct relation between stress and structural change can be clearly seen in Figure 5.9 by combining the stress and LEED measurements. The structural change is characterized by the LEED intensity ratio between integer spots intensity and fractional spots intensity. The experimental results reveal that the surface stress change during the
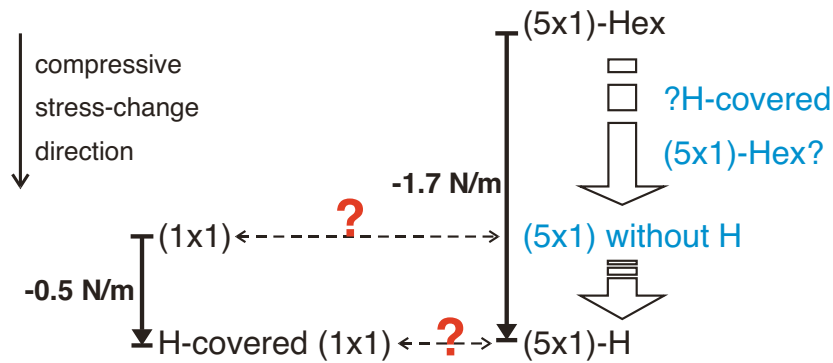
Figure 5.10: Illustration of the relation between H-induced stress change for Ir(100)-(5×1)Hex and Ir(100)-(1×1) surfaces. Two assumed surfaces—(5×1)-H without H coverage and a H-covered (5×1)Hex surface— are shown in blue. It is not clear whether the H-covered (1×1) surface has the same surface stress as (5×1)-H.

surface reconstruction is directly related with structural change. Considering the stress relaxation factors such as domain boundaries and surface steps, the stress change for an ideal single structural domain will be larger than the experimental result of -1.7 N/m. Due to the lack of the absolute value of the surface stress for Ir(100)-(5×1)Hex, it is hard to tell whether the tensile stress of (5×1)Hex surface is changed into compressive stress upon H-adsorption.

To analyze the role of surface stress change in the surface reconstruction process, it is helpful to assume two so-far invalid surfaces: a (5×1)-H surface reconstruction with H coverage being removed and the arrangements of Ir atoms remain unchanged (it is called (5×1) surface in the following discussion), an H-covered unreconstructed Ir(100)-(5×1)Hex surface. The Ir atomic arrangements at the (5×1)-H surface is quite similar to that of the (1×1) surface, with atomic rows being accommodated on (1×1) rearranged underlayers. The differences between (1×1) and (5×1)-H surface reconstruction are: Ir atomic rows at the (5×1)-H surface, as opposed to square Ir patches at the (1×1) surface; (5×1)-H surface is covered with hydrogen adsorbates. Due to the similar atomic arrangements, it is reasonable to consider that the surface stress for the assumed (5×1) surface is close to the (1×1) surface, and the surface stress for (5×1)-H surface is close to the H-covered (1×1) surface. The relations between the surface stresses of different reconstructions are shown in Figure 5.10. However, our stress measurements show that the surface stress change during H adsorption on the (5×1)Hex surface is much larger than that on the (1×1) surface. Assuming the surface stress of (5×1)-H surface is the same as the H-covered (1×1) surface, this result suggests that the (5×1)Hex surface has a larger tensile stress than (1×1) surface, which is against the belief from previous study [116]. It would also be very surprising if the surface stress of (1×1) is much larger (~ 1.2 N/m) than the assumed (5×1) surface.

If the surface stress of (5×1)Hex reconstruction is larger than the tensile stress of (1×1) surface (as illustrated in Figure 5.10), the large tensile stress of (5×1)Hex surface is relieved during H-induced surface reconstruction. The surface stress of (5×1)-H could still be compressive, and therefore the reconstruction of (5×1)Hex to (5×1)-H may be driven by the surface stress relaxation.

5.2.2 Stress change due to oxide formation

The metal oxides have attracted increasing interest in the last two decades, because of their wide technological applications such as sensors and catalysts, as well as in many basic researches fields [119]. As one of the transition metal oxide, CoO has attracted wide attention especially due to its magnetism. Bulk CoO is antiferromagnetic with a relatively low Néel temperature (292 K) compared to NiO (570 K). Investigations on the influence of the Néel temperature on the exchange bias have been performed [120], and quite recently, in the CoO nanopaticles on CoO matrix, a new mechanism considering the exchange bias is found to provide a way to beat the superparamagnetic limit in isolated particles [121].

CoO(111) has polar surfaces, and polar surfaces often show peculiar chemical and physical properties different from those of the neutral surfaces. According to analysis on the electronic structures of both neutral and polar surfaces, it is found that the polar surfaces are normally more chemical active as the wide energy gap for neutral surfaces does not exist in polar surfaces of oxide, and the cation surfaces are even expected to be metallic [122]. And it is found that the CoO(111) surface may be metal terminated, in contrast to the O-terminated NiO(111), which may lead to special applications. In addition, neutron diffraction results suggest that CoO has alternating ferromagnetic (111) planes alternatively arranged along the [111] direction, therefore it is expected that the uncompensated magnetic moments would appear and the anti-ferromagnetic order of a CoO(111) film would change into ferromagnetic [123].

For these reasons, the properties and fabrication of CoO(111) is of great interest, and the recent success in growing CoO(111) films on Ir(100) by post-oxidation of 2 ML Co films allows to study the stress change involved in the oxide formation.

Bulk CoO crystal has a fcc-type rock-salt crystal structure as shown in Figure 5.11. The Co^{2+} and O^{2-} (111) planes are alternatively arranged along [111] direction, hence the CoO(111) is a polar surface. The ideal polar (111) surface is considered to be unstable according to classical electrostatics. However, the polar surface can still be stabilized if the macroscopic component of the dipole moment and the polarity is canceled out by modification of the charge density in the outer layers, provided the condition for cancellation is fulfilled [124, 125]. Different depolarization mechanisms have been proposed, such as defect structures, reconstructions and adsorption of impurities. The CoO(111) surface obtained by cutting a CoO bulk sample are stabilized by reconstruction or adsorption of foreign atoms [126]. In addtion, CoO(111) films stabilized by OH adsorptions have been reported by Camppus et. al [127] and Sindhu et. al. [128]. In contrast, clean and unreconstructed CoO(111) films are reported to be achieved by alternative depositing Co and O layers on Pt(111) substrate [129].

Simply suppose an ideal (111) polar surface, the coulomb interaction between the intra-layer atoms with same charge polarity would result in a repulsive force, hence a compressive stress is expected. If a metal surface—which is normally with tensile stress—would change into a polar (111) surface, a compressive stress change is anticipated. However, the stress change involved in the process of creating a polar oxide surface has not been measured up to now, and the first result is presented here.

In this study, the stress measurements performed during oxidation of 2 ML Co(100) on Ir(100)-(1×1) indicate that indeed a compressive stress change is induced (see Figure 5.13(e)). Although the maximum stress change is as large as -4.3 N/m, the overall
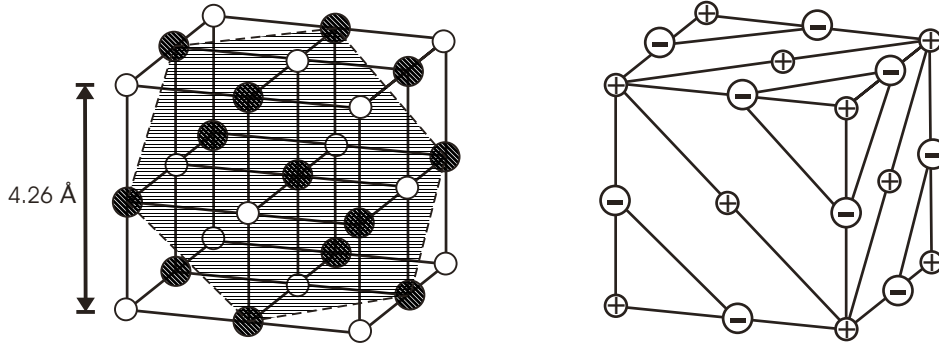
Figure 5.11: Lattice of CoO crystal with rock-salt crystal structure and the respective (111) polar planes. The lattice constant of CoO bulk crystal is 4.26 Å.

stress change is only about -0.5 N/m. However, the tensile stress of the Co layer needs to be considered also, as discussed below.

    To analyze the stress change induced by oxidation of 2 ML Co on Ir(100), our starting point is to estimate the mismatch induced stress between Ir(100) and CoO(111). LEED and STM [80] study reveal that the hard sphere model of CoO(111) film as illustrated in Figure 5.12 gives the main structural features. At the interface, the Co layer or the oxygen layer rearranges into a c(10×2) structure after oxidation. As shown in Figure 5.11, the lattice constant of bulk CoO is 4.26 Å , so the nearest neighbor between Co ions or oxygen ions in the CoO(111) plane is 3.01 Å. The nearest neighbor of Ir(100) square lattice is 2.715 Å along [110] direction, therefore the hexagonal CoO(111) lattice is slightly distorted to fit the Ir(100) substrate by establishing the c(10×2) reconstruction. Along the length of the c(10×2) unit, the original $9a_{CoO}^{NN}$ length is expanded into $10a_{Ir}^{NN}$, which causes an in-plane strain of 0.22%. Similarly, in the primitive CoO(111) lattice the width of the c(10×2) unit is $\sqrt{3}a_{CoO}^{NN} = 5.21$ Å, which is expanded to Ir(100) substrate of the width $2a_{Ir}^{NN} = 5.43$ Å and causes an in-plane strain of 4.2%. We conclude that the CoO films is under an anisotropic in-plane strain of +0.22% and +4.2%.

    The relation between in-plane strain and stress for a (111) film with cubic structure follows as [25]

$$
\begin{aligned}
\tau_i &= (\frac{1}{2}c_{11} + \frac{1}{2}c_{12} + c_{44} - \frac{1}{3}\frac{(c_{11} + 2c_{12} - 2c_{44})^2}{c_{11} + 2c_{12} + 4c_{44}})\epsilon_i \\
&+ (\frac{1}{6}c_{11} + \frac{5}{6}c_{12} - \frac{1}{3}c_{44} - \frac{1}{3}\frac{(c_{11} + 2c_{12} - 2c_{44})^2}{c_{11} + 2c_{12} + 4c_{44}})\epsilon_j
\end{aligned}
\tag{5.6}
$$

with $i = 1$, $j = 2$ and $i = 2$, $j = 1$. For CoO(111) on Ir(100), the in-plane strain is 0.22% and 4.2% along the two orthogonal vectors of c(10×2) unit mesh respectively, as indicated in Figure 5.12. And the elastic coefficients of CoO are shown in Table 5.5.

    The in-plane mismatch-induced stress for 2 layers of CoO is calculated as $\tau_x = 0.52$ N/m and $\tau_y = 3.59$ N/m respectively. As the Ir(100) substrate has a four-fold symmetry and the c(10×1) reconstruction of CoO(111) films is two-fold symmetric, there are two orthogonal structural domains to fit the Ir(100) substrate as shown in Figure 5.12(c), which is proven by the LEED images (Figure 5.13(d)) that show two set of spots rotated 90° from one another. Considering the existence of the two equivalent orthogonal
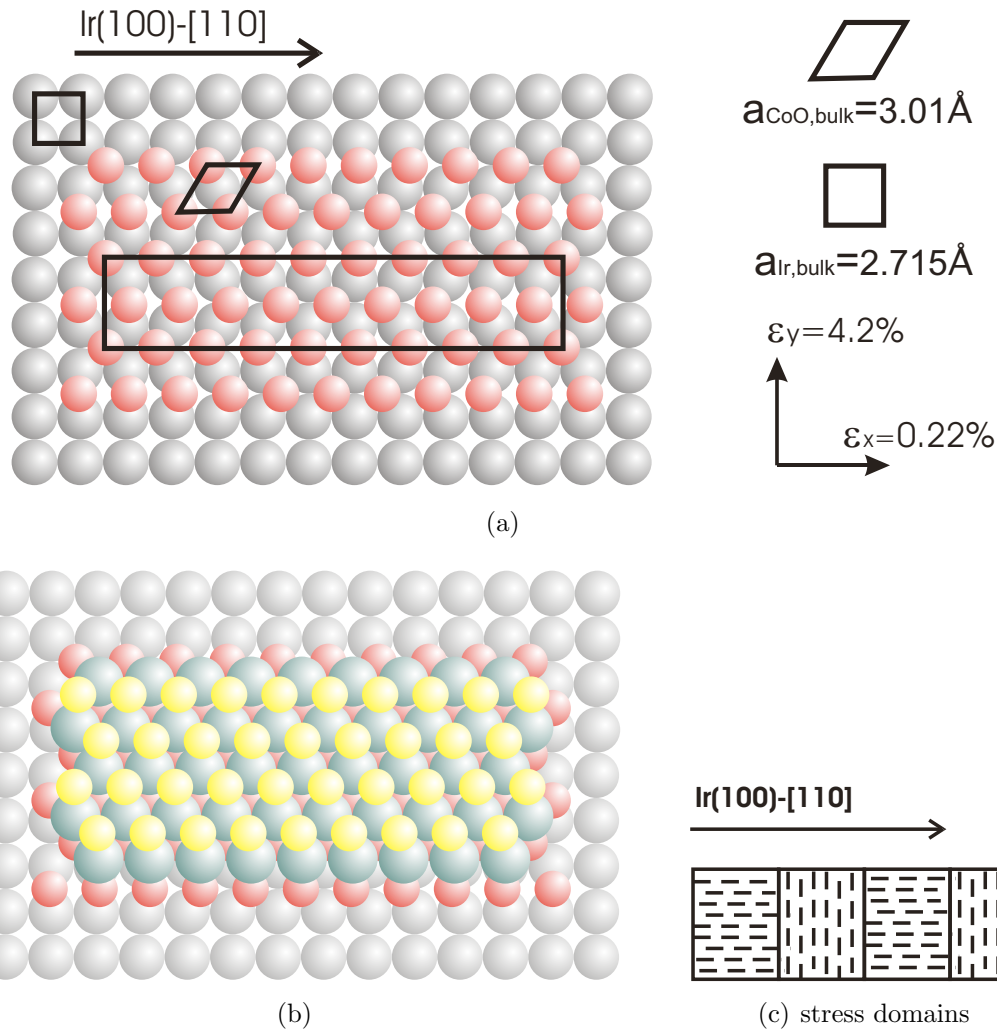
Figure 5.12: Hard sphere model of CoO films on Ir(100)-(1×1) from STM and LEED study [80]. 1 ML CoO film (a) and 2 ML CoO (b) shows c(10×2) reconstruction. Two structural domains coexist at the surface as is illustrated in (c).

reconstruction domains, it is appropriate to calculate the average in-plane stress as

$$\tau_{avg} \approx (\tau_x + \tau_y)/2 = 2.05 \quad \text{(N/m)}$$

for 2 layers CoO(111).

During the epitaxial growth of 2 ML Co on Ir(100), I measured a stress change of $\Delta\tau = +2.6$ N/m. The complete oxidation of 2 ML Co to get 2 layers of CoO(111) induced a stress change $\Delta\tau_2 = -0.5$ N/m. As a result, the overall stress change is measured as $\Delta\tau = \Delta\tau_1 + \Delta\tau_2 = +2.1$ N/m, which is almost the same with the mismatch induced stress change for 2 ML CoO on Ir(100). The measured stress can be completely ascribed to the misfit. This finding is in line with the idea that the polar surface may be stabilized if the polarity is canceled out. The stress measuremental result is, therefore, an indirect evidence that the polarity of the CoO(111) films are canceled with the formation of c(10×2) surface reconstruction.

LEED images as shown in Figure 5.13 (see also Figure 4.22) suggest the structural evolution during post-oxidation of 2 ML Co. As the diffraction spots originate from

Table 5.5: The elasitic coefficients of CoO from [130]. s_{ij} is in $(TPa)^{-1}$ and c_{ij} is in GPa.

| | s_{11} | s_{44} | s_{12} | c_{11} | c_{44} | c_{12} |
		$(TPa)^{-1}$			GPa	
CoO	6.43	12.1	-2.31	260	82.4	14.5

(a) 10 L   (b) 100 L   (c) 160 L   (d) 400 L
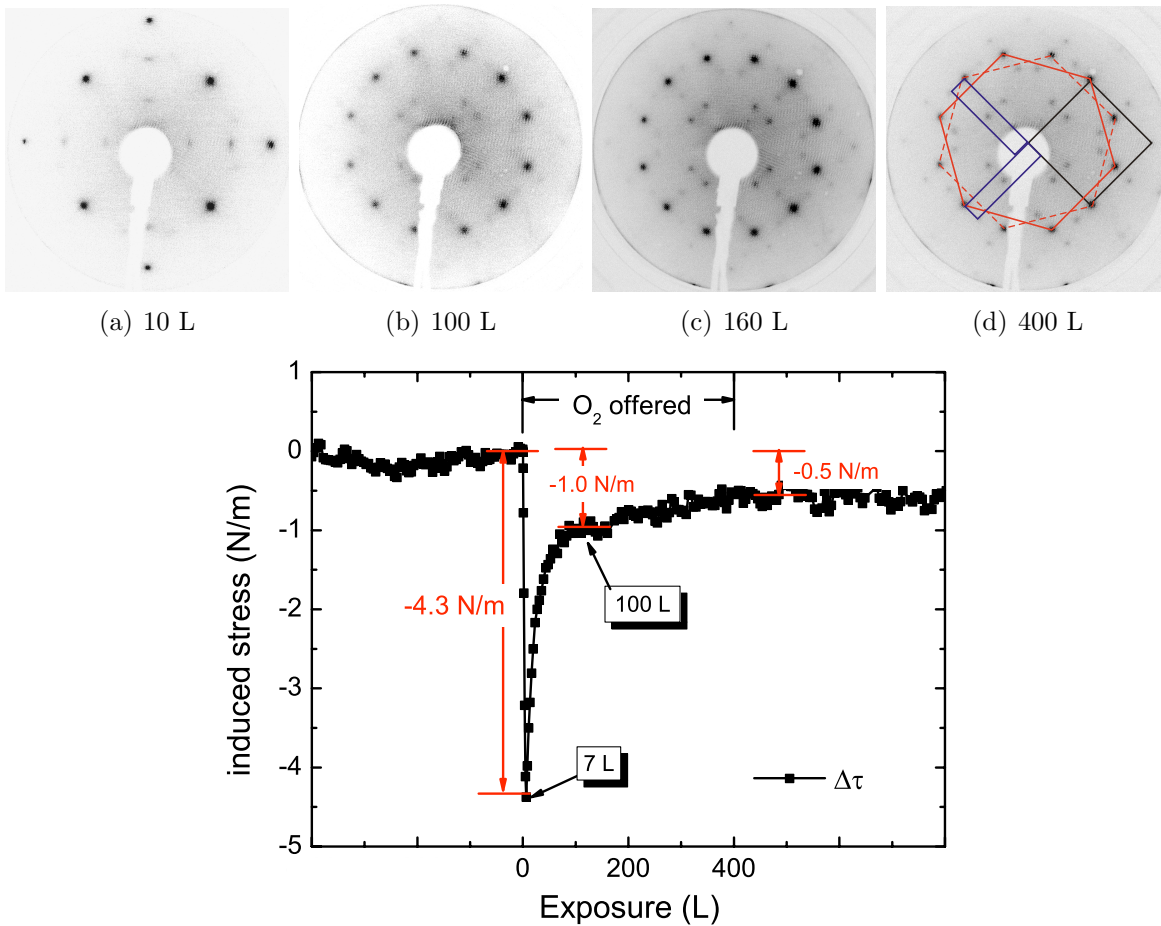
Figure 5.13: Stress change measured during post-oxidation of 2 ML Co on Ir(100) at about 200 °C and the corresponding LEED pattern of 2 ML CoO/Ir(100) (see text), and the LEED images of post oxidation of 2 ML Co on Ir(100)-(1×1) upon different amount of oxygen exposure.

the quadratic substrate, the quasihexagonal CoO(111) film and the c(10×2) reconstructions, the appearance of the corresponding LEED spots implies the formation of the related lattice structure. Compared to the stress curve, the stress changed with respect to the structure change may be figured out. In the LEED image (Figure 5.13(a)) taken for 2 ML Co(100) upon oxygen exposure of 10 L, it is obvious that in this oxidation stage the CoO(111) layers is not formed yet, as the spots mainly stem from the quadratic Co(100)-(1×1) layers and Ir(100) substrate. It is excluded that the large compressive stress change observed soon after the oxygen is offered corresponds to the formation of

the polar (111) surface. Only after oxygen exposure of 100 L, the LEED pattern (Figure 5.13(b))shows diffraction spots, from the quasi-hexagonal layers, indicating the Co and O atoms are already arranged into the CoO(111) layers. The c(10×2) spots are very weak, suggesting that after the remarkable stress change within exposure of 100 L the CoO(111) layers are already created, yet still not arranged well in a long range order to accommodate on the quadratic substrate. The LEED images taken with oxygen exposure of more than 160 L (Figure 5.13(c)) present LEED spots corresponding to the completely oxidized layer, which means that the small variation in the stress curve is related with the structural rearrangement of the atoms. In summary, the LEED patterns at different oxidation stages reveal that the oxygen firstly react with Co layers to CoO(111) layers, and then the c(10×2) reconstruction is gradually developed.

Chapter 6

Conclusions and outlook

In this work the correlation between stress, strain and magnetic anisotropy is studied with the optical bending beam method, LEED and MOKE. Stress measurements are combined with LEED to explore the correlation between stress and structural change in epitaxial thin films, during surface reconstruction and in an oxide layer on Ir(100). With high sensitivity stress measurements, the strain dependence of magnetoelastic coupling coefficients is explored for magnetic monolayers.

The structure of epitaxial thin films very often differs from the bulk, and film stress help to determine the film structure. As the obtained film stress can be quantitatively compared to the misfit induced stress in the film, our experimental results clearly determined the pseudomorphic growth of Fe, Co and Ni monolayers on Ir(100), in combination with LEED measurements. In addition, the magnitude of film stress suggests a structural transition from a fcc-Fe precursor to a bcc lattice at 2 ML. This result goes beyond the results of a quantitative LEED analysis, as the misfit stress of bcc-Fe differs in magnitude and sign from that of fcc-Fe for the same in-plane atomic distance. The film stress during pseudomorphic growth is ascribed to the misfit induced stress, and it relaxes as the thickness increases further. Our combined stress and diffraction studies identify the formation of misfit dislocations as a stress relaxation mechanism in monolayer thin film. Stress measurements can also be seen from the oscillatory modulations of the stress curves, which are accompanied with the dislocation formation (for 2-12 ML Ni/Ir(100)) or caused by mesoscopic structures (for 2-5 ML Co/Ir(100)).

Our stress measurements show that different surface reconstructions of Ir(100) induce comparable film stress except for the first few monolayers. These results suggest that the surface reconstructions are lifted after the deposition of the metal layers, and the structure evolution of the lattice shows a similar behavior. This conclusion is in agreement with previous STM and LEED-I(V) studies.

Nevertheless, the relation between structure, strain and stress is complex beyond pseudomorphic growth. Our experimental results indicate that there are more factors that may influence the stress we measured. The simple relation between stress and strain works well for pseudomorphic growth, but it is only an approximation for thicker films. Our measurements of film stress in thicker films, beyond pseudomorphic growth suggests that an $1/t_F$ (t_F is film thickness) dependence of film strain is a bad approximation, and a sizeable residual film strain ($\epsilon^{res} \neq 0$) remains up to tens of nm.

Another aspect of the relation between stress and structure is the role of surface stress in surface reconstruction. A tensile stress change of -1.75 N/m is measured during

the H-induced surface reconstruction change from Ir(100)-(5×1)Hex to Ir(100)-(5×1)-H. Our combined LEED and stress measurements identify a direct correlation between surface stress and surface reconstruction . However, more messages such as the surface stresses of Ir(100)-(5×1)Hex and Ir(100)-(5×1)-H are required for further conclusions.

For the first time the relation between stress and misfit of an oxide layer on a metal substrate is explored. The stress in 2 layers of CoO(111) is measured and a tensile overall stress change of +4.3 GPa. This result indicates that misfit, rather than a repulsive coulomb interaction, determines the stress behavior of CoO(111). It shows that stress measurement can be a convenient method to study a potential charge polarity of oxide layers. For CoO(111), our results do not indicate repulsive interactions which might have been anticipated. Thus, stress studies provide a new aspect for the understanding of polar surfaces. More studies such as on the atomic structure of the interface and the layer sequences are required in order to find the depolarization mechanism which seems to be operative in CoO(111) layers.

It has been found that the magnetoelastic coupling is closely related to the film strain in the magnetic monolayers. Therefore, we studied the strain dependence of the magnetoelastic coefficients B_1 and B_2 for Fe, Co and Ni on Ir(100). All the effective values of B_1 and B_2 we obtained differ from the respective bulk values. B_i^{eff} for Fe, Co and Ni films at different thickness but similar film strain are alike, which suggests a strain dependence of the magnetoelastic coupling effects. The values of B_1^{eff} and B_2^{eff} for fcc-Co as well as B_2^{eff} fcc-Ni are measured for the first time in strained monolayers. Magnetoelastic coupling of Fe is investigated in a negative strain range, and the strain dependence differs from previous studies with positive strain. In addition, the obtained B_i^{eff} values for Fe on different Ir(100) surface reconstructions indicate that the effective magnetoelastic coupling coefficients do not depend on the details of surface reconstruction. Our experimental results reveal that the linear strain dependence of B_i^{eff} can be applied for a certain strain range, and higher orders of strain contribution may play a role for a larger strain range.

Our estimations of the magnetic anisotropy using the linear strain dependent B_1^{eff} agree with the MOKE measurements within the thickness range being studied. Especially, a spin reorientation transition is observed for Ni on Ir(100). The magnetic easy axis changes from out-of-plane to in-plane at about 15 ML as the thickness increases. This is in line with the expectation using the strain dependent B_1^{eff} we obtained. Such a favorable description cannot be obtained with the bulk value of B_1. These results indicate that the bulk values of the magnetoelastic coefficients cannot be applied to a strained sample, whereas the linear strain dependence of B_i^{eff} is appropriate in a certain strain range. The strain range in which a linear dependence of B^{eff} on strain is a valid description depends on the specific system.

Due to the experimental limitation of our present experimental set-up, there are questions left open. The magnetic properties of the magnetic monolayers with thickness of 1-3 ML may be investigated at a lower temperature, and the magnetic anisotropy for out-of-plane magnetization can be used to examine our understanding of the strain dependent magnetoelastic coupling coefficients. This work may stimulate more interest in the study of magnetoelastic coupling in a nano-sized sample. Following the idea of this study, the stress change during oxide formation and reconstruction may be systematically studied for more systems, so that an better understanding of the correlation between surface stress and surface reconstruction may be obtained.

Bibliography

[1] M. Wuttig and X. Liu, *Ultrathin Metal Films: Magnetic and Structural Properties*, Springer-Verlag, 2004.

[2] D. Mills, J. Magn. Magn. Mater. **100**, 515 (1991).

[3] R. C. O'Handley, *Modern Magnetic Materials: Principles and Applications*, JOHN WILEY & SONS, INC., New York, 2000.

[4] M. Bander and D. Mills, Phys. Rev. B **38**, 12015 (1988).

[5] P. Grünberg, Phys. Today **54**, 31 (2001).

[6] R. Skomski and J. M. D. Coey, *Permanent Magnetism*, Institute of Physics Publishing, Bristol, 1999.

[7] S. D. Bader, Surf. Sci **500**, 172 (2002).

[8] D. Sander, J. Phys: Condens. Matter **16**, R603–R636 (2004).

[9] B. Schulz and K. Baberschke, Phys. Rev. B **50**, 13467 (1994).

[10] Y. Z. Wu, R. Vollmer, H. Regensburger, and J. Kirschner, Phys. Rev. B **62**, 5810 (2000).

[11] T. Burkert, O. Eriksson, P. James, S. I. Simak, B. Johansson, and L. Norstöm, Phys. Rev. B **69**, 104426 (2004).

[12] T. Burkert, L. Nordström, O. Eriksson, and O. Heinonen, Phys. Rev. Lett. **93**, 027203 (2004).

[13] S. W. Sun and R. C. O'Handley, Phys. Rev. Lett. **66**, 2798 (1991).

[14] G. Bochi, O. Song, and R. C. O'Handley, Phys. Rev. B **50**, 2043 (1994).

[15] G. Bochi, C. A. Ballentine, H. E. Inglefield, C. V. Thompson, and H. R. C. O'Handley, Phys. Rev. B **53**, R1729 (1996).

[16] G. Wedler, J. Walz, , A. Greuer, and R. Koch, Phys. Rev. B **60**, 11313 (1999).

[17] T. Gutjahr-Löser, D. Sander, and J. Kirschner, J. Appl. Phys. **87**, 1085 (2000).

[18] R. Koch, M. Weber, K. Thürmer, and K. H. Rieder, J. Magn. Magn. Mater. **159**, L11–L16 (1996).

[19] M. Ciria, J. I. Arnaudas, and A. del Moral, Phys. Rev. B **70**, 054431 (2004).

[20] M. Ciria, K. Ha, D. Bono, and R. C. O'Handley, J. Appl. Phys. **91**, 8150 (2002).

[21] K. Baberschke, K. Donath, and W. Nolting, Band-Ferromagnetism, in *Lecture Notes in Physics: Physics and Astronomy*, Springer, 2001.

[22] R. Q. Wu, L. J. Chen, A. Schick, and A. J. Freeman, J. Magn. Magn. Mater. **177**, 1216 (1998).

[23] M. Komelj and M. Fähnle, Phys. Rev. B **65**, 092403 (2002).

[24] G. Y. Guo, J. Magn. Magn. Mater. **209**, 33–36 (2000).

[25] D. Sander, Rep. Prog. Phys. **62**, 809 (1999).

[26] T. Gutjahr-Löser, D. Sander, and J. Kirschner, J. Mag. Mag. Mat. **220**, L1–L7 (2000).

[27] J. M. Barandiarán, A. Hernando, V. Madurga, O. V. Nielsen, M. Vázquez, and M. Vázquez-López, Phys. Rev. B **35**, 5066 (1987).

[28] M. Weber, R. Koch, , and K. H. Rieder, Phys. Rev. Lett. **73**, 1166 (1994).

[29] M. Ciria, J. I. Arnaudas, L. Benito, C. de la Fuente, A. del Moral, J. K. Ha, and R. C. O'Handley, Phys. Rev. B **67**, 024429 (2003).

[30] R. Koch, C. Pampuch, H. Yamaguchi, A. K. Das, A. Ney, L. Däweritz, and K. H. Ploog, Phys. Rev. B **70**, 092406 (2004).

[31] W. Haiss, Rep. Prog. Phys. **64**, 591–648 (2001).

[32] J. Fritz, M. K. Baller, H. P. Lang, T. Strunz, E. Meyer, H. J. Güntherodt, E. Delamarche, C. Gerber, and J. K. Gimzewski, Langmuir **16**, 9694 (2000).

[33] J. E. Müller, M. Wuttig, and H. Ibach, Phys. Rev. Lett. **56**, 1583 (1986).

[34] C. E. Bach, M. Giesen, and H. Ibach, Phys. Rev. Lett. **78**, 4225 (1997).

[35] M. J. Harrison, D. P. Woodruff, , J. Robinson, D. Sander, W. Pan, and J. Kirschner, Phys. Rev. B **74**, 165402 (2006).

[36] J. W. Gibbs, in *The Scientific Papers of J. W. Gibbs*, volume 1, page 55, Longmans-Green, 1906.

[37] R. Shuttleworth, Proc. Phys. Soc. **A63**, 445 (1950).

[38] H. Ibach, Surf. Sci. Rep. **29**, 193 (1997).

[39] D. Sander, U. Linke, and H. Ibach, Surf. Sci. **272**, 318 (1992).

[40] A. Grossmann, W. Erley, and H. Ibach, Surf. Sci. **337**, 183 (1995).

[41] R. C. Cammarata and T. Trimble, J. Mater. Res. **15**, 2468 (2000).

[42] D. Sander and H. Ibach, Physics of covered solid surfaces, in *Landolt-Börnstein, Numerical Data and Functional Relationships in Science and Technology*, volume 42 of *Group III Condensed Matter*, Springer, 2002.

[43] A. Zangwill, *Physics at Surfaces*, Cambridge University Press, Cambridge, 1988.

[44] F. C. Frank and J. H. van der Merwe, Proc. Roy. Soc. **A 198**, 216 (1949).

[45] J. H. van der Merwe, J. Appl. Phys. **34**, 117 (1963).

[46] J. W. Matthews and A. E. Blakeslee, Journal of Crystal Growth **27**, 118–125 (1974).

[47] J. W. Matthews, J. Vac. Sci. Technol. **12**, 126 (1975).

[48] G. L. Price, Appl. Phys. Lett. **53**, 1288 (1988).

[49] K. Baberschke, Appl. Phys. A **62**, 417 (1996).

[50] P. Bruno, Physical Origins and Theoretical Models of Magnetic Anisotropy, in *Magnetismus von Festkörpern und Grenzflächen*, Forschungszentrum Jülich, 1993.

[51] P. Poulopoulos, J. Lindner, M. Farle, and K. Baberschke, Surf. Sci. **437**, 277 (1999).

[52] J. K. D. Sander, A. Enders, J. Magn. Magn. Mater. **200**, 439–455 (1999).

[53] E. P. Wohlfarth and K. H. J. Buschow, *Ferromagnetic Materialsa handbook on the properties of magnetically ordered substances*, North-Holland Publ. Co., Amsterdam, 1986.

[54] M. B. Stearns, Magnetic Properties of 3d, 4d and 5d Elements, Alloys and Compounds, in *(Landolt-Börnstein Numerical Data and Functional Relationships in Science and Technology*, volume 19a of *Group III*, 1984.

[55] C. Kittel, Rev. Mod. Phys. **21**, 541 (1949).

[56] E. W. Lee, Rep. Prog. Phys. **18**, 184 (1955).

[57] R. Becker and W. Döring, *Ferromagnetismus*, Springer, Berlin, 1939.

[58] W. J. J. Carr, Secondary Effects in Ferromagnetism, in *Handbuch der Physik*, volume 2 of *XVIII*, Springer, 1966.

[59] G. Stoney, Proc. R. Soc. London A **82**, 172 (1909).

[60] D. Sander and J. Kirschner, Appl. Phys. A **87**, 419 (2007).

[61] D. Sander, A. Enders, , and J. Kirschner, Rev. Sci. Instrum. **66**, 4734 (1995).

[62] R. E. Martinez, W. M. Augustyniak, and J. A. Golovchenko, Phys. Rev. Lett. **64**, 1035 (1990).

[63] A. J. Schell-Sorokin and R. M. Tromp, Phys. Rev. Lett. **64**, 1039 (1990).

[64] D. Sander, S. Ouazi, A. Enders, T. Gutjahr-Löser, V. S. Stepanyuk, D. I. Bazhanov, and J. Kirschner, J. Phys.Condens. Matter. **14**, 4165 (2002).

[65] K. Dahmen, S. Lehwald, and H. Ibach, Surf. Sci. **446**, 161 (2000).

[66] D. Sander, Current Opinion in Solid State and Material Science **7**, 51 (2003).

[67] E. du Trémolet de Lacheisserie and J. C. Peuzin, J. Magn. Magn. Mater. **136**, 189 (1994).

[68] R. F. S. Hearmon, The elastic constants of nonpiezoelectric crystals, in *Landolt-Börnstein Numerical Data and Functional Relationships in Science and Technology*, volume 2 of *Group III*, Springer-Verlag, 1969.

[69] L. J. Clarke, *Surface Crystallography, An Introduction to Low Energy Electron Diffraction*, JOHN WILEY & SONS, 1985.

[70] S. D. Bader, J. Magn. Magn. Mater. **100**, 440 (1991).

[71] Z. Q. Qiu and S. D. Bader, Rev. Sci. Instr. **71**, 1243 (2000).

[72] L. D. Landau and E. M. Lifshtz, *Electrodynamics of Continuous Media*, Pergamon, London, 1960.

[73] A. Schmidt, W. Meier, L. Hammer, and K. Heinz, J. Phys.Condens. Matter **14**, 12353 (2002).

[74] L. Hammer, W. Meier, A. Klein, P. Landfried, A. Schmidt, and K. Heinz, Phys. Rev. Lett. **91**, 156101 (2003).

[75] K. Heinz, G. Schmidt, L. Hammer, and K. Müller, Phys. Rev. B **32**, 6214 (1985).

[76] K. Johnson, Q. Ge, S. Titmuss, and D. A. King, J. Chem. Phys. **112**, 10460 (2000).

[77] A. Klein, *Dissertation*, Universität Erlangen-Nürnberg, 2007.

[78] G. A. Prinz, Phys. Rev. Lett. **54**, 1051 (1985).

[79] D. Lerch, A. Klein, A. Schmidt, S. Müller, L. Hammer, K. Heinz, and M. Weinert, Phys. Rev. B **73**, 075403 (2006).

[80] C. Giovanardi, L. Hammer, and K. Heinz, Phys. Rev. B **74**, 125429 (2006).

[81] J. Donnay and H. Ondik, *Crystal data*, National Bureau of Standards, Gaithersburg, MD, 1973.

[82] J. Zarestky and C. Stassis, Phys. Rev. B **35**, 4500 (1987).

[83] J. Adams, D. Agosta, R. Leisure, , and H. Ledbetter, J. Appl. Phys. **100**, 113530 (2006).

[84] D. Pescia, G. Zampieri, M. Stampanoni, G. L. Bona, R. F. Willis, and F. Meier, Phys. Rev. Lett. **58**, 933 (1987).

[85] L. Smardz, U. Koebler, D. Kerkmann, F. Schumann, D. Pescia, and W. Zinn, Z. Phys. B-Condensed Matter **80**, 1 (1990).

[86] C. M. Schneider, P. Bressler, P. Schuster, and J. Kirschner, Phys. Rev. Lett. **64**, 1095 (1990).

[87] B. Heinrich, A. Arrott, J. F. Cochran, S. T. Purcell, K. B. Urquhart, and K. Myrtle, Journal of Crystal Growth **81**, 562 (1987).

[88] Z. Wang, Y. Li, F. Jona, and P. Marcus, Solid State Commun. **61**, 623 (1987).

[89] C. S. Tian, D. Qian, D. Wu, R. H. He, Y. Z. Wu, W. X. Tang, L. F. Yin, Y. S. Shi, G. S. Dong, X. F. Jin, X. M. Jiang, F. Q. Liu, H. J. Qian, K. Sun, L. Wang, G. Rossi, Z. Q. Qiu, and J. Shi, Phys. Rev. Lett. **94**, 137210 (2005).

[90] S. M. Valvidares, T. Schroeder, O. Robach, C. Quirós, T.-L, Lee, and S. Ferrer, Phys. Rev. B **70**, 224413 (2004).

[91] V. L. M. et al., Phys. Rev. Lett. **57**, 2211 (1986).

[92] G. Y. Guo and H. H. Wang, Chinese Journal of Physics **38**, 949 (2000).

[93] M. Fähnle, M. Komelj, R. Q. Wu, and G. Y. Guo, Phys. Rev. B **65**, 144436 (2002).

[94] V. Martin, W. Meyer, C. Giovanardi, L. Hammer, K. Heinz, Z. Tian, D. Sander, and J. Kirschner, Phys. Rev. B **76**, 205418 (2007).

[95] P. Bruno, Appl. Phys. A **49**, 499 (1989).

[96] R. Popescu, H. L. Meyerheim, D. Sander, J. Kirschner, P. Steadman, O. Robach, and S. Ferrer, Phys. Rev. B **68**, 155421 (2003).

[97] A. Klein, L. Hammer, and K. Heinz, private communications .

[98] D. Sander, S. Ouazi, V. S. Stepanyuk, D. I. Bazhanov, and J. Kirschner, Surf. Sci. **512**, 281 (2002).

[99] A. K. Schmid and J. Kirschner, Ultramicroscopy **42-44**, 483 (1992).

[100] J. J. Croat, J. Appl. Phys. **55**, 1984 (2078).

[101] R. C. O'Handley, J. Megusar, S. Sun, Y. Hara, and N. J. Grant, J. Appl. Phys. **57**, 1985 (3563).

[102] E. du Trémolet de Lacheisserie, *MagnetostrictionTheory and Applications of Magnetoelasticity*, CRC press, Boca Raton, FL, 1993.

[103] M. Fähnle and M. Komelj, Z. Metallkd. **93**, 970 (2002).

[104] T. Gutjahr-Löser, D. Sander, and J. Kirschner, J. Magn. Magn. Matter. **220**, L1 (2000).

[105] U. Gradmann, J. Magn. Magn. Mater. **100**, 481 (1991).

[106] A. J. Freeman and R. Q. Wu, J. Magn. Magn. Mater. **100**, 497 (1991).

[107] U. Gradmann, K.Wagner, N.Weber, and H. J. Elmers, J. Magn. Magn. Mater. **167**, 21 (1997).

[108] J. A. C. Bland, C. Daboo, B. Heinrich, Z. Celinski, and R. D. Bateson, Phys. Rev. B **51**, 258 (1995).

[109] L. Néel, J. Phys. Rad. **15**, 376 (1954).

[110] W. Pan, D. Sander, M. Lin, and J. Kirschner, Phys. Rev. B **68**, 224419 (2003).

[111] H. Ibach, Surf. Sci. Rep. **35**, 71 (1999).

[112] M. Mansfield and R. J. Needs, J. Phys.:Condens. Matter **2**, 2361 (1990).

[113] R. C. Cammarata, Surf. Sci. **279**, 341 (1992).

[114] L. Pauling, *The Nature of the Chemical Bond*, Cornell Univ. Press, Ithaca, NY, 1960.

[115] R. J. Needs, Phys. Rev. Lett. **58**, 53 (1987).

[116] S. Lehwald, J. G. Chen, G. Kisters, E. Preuss, and H. Ibach, Phys. Rev. B **43**, 3920 (1991).

[117] A. Filipetti and V. Fiorentini, Surf. Sci. **112**, 377 (1997).

[118] P. J. Feibelman, Phys. Rev. B **56**, 2175 (1997).

[119] V. Henrich and P. Cox, *The Surface Science of Metal Oxide*, Cambridge University Press, Cambridge, 1994.

[120] F. Voges, H. de Gronchkel, C. Osthöber, R. Schreiber, and P. Grünberg, J. Magn. Magn. Mater. **190**, 183 (1998).

[121] V. Skumryev, S. Stoyanov, Y. Zhang, G. Hadjipanayis, D. Givord, and J. Nogués, Naure **423**, 850 (2003).

[122] M. Tsukada, H. Adachi, and C. Satoko, Progress in Surface Science **14**, 113 (1983).

[123] T. Ambrose and C. L. Chien, Phys. Rev. Lett. **76**, 1743 (1996).

[124] C. Noguera, J. Phys.Condens. Matter. **12**, R367 (2000).

[125] C. Tusche, H. L. Meyerheim, and J. Kirschner, Phys. Rev. Lett. **99**, 026102 (2007).

[126] C. Mocuta, A. Barbier, and G. Renaud, Appl. Surf. Sci. **162**, 56 (2000).

[127] D. Cappu, M. Haßel, E. Neuhaus, M. Heber, F. Rohr, and H. J. Freund, Surf. Sci. 337 (1995) 268 **337**, 268 (1995).

[128] S. Sindhu, M. Heiler, K. M. Schindler, and H. Neddermeyer, Surf. Sci. **541**, 197 (2003).

[129] S. Entani, M. Kiguchi, and K. Saiki, Surf. Sci. **566-568**, 165 (2004).

[130] R. Hearmon, The Elastic Constants of Crystals and Other Anisotropic Materials, in *Landolt-Börnstein Numerical Data and Functional Relationships in Science and Technology*, volume 18 of *Group III*, Springer, 1984.

Acknowledgements

Eidesstattliche Erklärung

Ich erkläre hiermit, dass ich keine anderen als die von mir angegebenen Quellen und Hilfsmittel zur Erstellung meiner Dissertation verwendet habe. Den benutzten Werken wörtlich oder inhaltlich entnommene Stellen sind als solche gekennzeichnet.

Zhen Tian

Halle (Saale), August 4, 2008

Curriculum vitae

First Name	Zhen
Family Name	Tian
Date of Birth	January 06, 1978
Place of Birth	Hebei, China
Nationality	P. R. China
E-mail	tianzhen@mpi-halle.de

EDUCATION

Sep. 1996 - Jul. 2000	Fudan University (Shanghai, China) Department of Physics Bachelor of Science
Sep. 2001 - Jul. 2004	Fudan University (Shanghai, China) Department of Physics Master of Science
Since Sept. 2004	Max-Planck Institute of Microstructure Physics and Martin-Luther-Universität Halle-Wittenberg Ph. D. candidate (Supervisor: Prof. Jürgen Kirschner)

Contributed presentations

1. Film stress, structure and magnetic properties of Ni grown on Ir(100)
   Tian, Z., D. Sander, and J. Kirschner.
   The 8th International Conference on the Structure of Surfaces, München, Germany.
   18.-22.07.2005, Poster

2. Large film stress of Fe, Co and Ni monolayers on Ir(100).
   Tian, Z. C. S. Tian, D. Sander, and J. Kirschner.
   Frühjahrstagung des Arbeitskreises Festkörperphysik der Deutschen Physikalischen Gesellschaft, Dresden, Germany.
   27.-31.03.2006, Talk

3. Second-order magnetoelastic coupling of strained Fe monolayers.
   Tian, Z. ,C. S. Tian, D. Sander, and J. Kirschner.
   Frühjahrstagung des Arbeitskreises Festkörperphysik der Deutschen Physikalischen Gesellschaft, Dresden, Germany.
   27.-31.03.2006, Talk

4. Stress beyond elasticity limits and magnetic anisotropy of ferromagnetic monolayers.
   Tian, Z. C. S. Tian, D. Sander, and J. Kirschner.
   5th German-Brazilian Workshop, Mangaratiba, Brazil.
   03.-07.04. 2006, Poster

5. Nonlinear magnetoelastic coupling coefficients in strained Fe, Co and Ni monolayers
   Tian, Z., D. Sander, and J. Kirschner
   Frühjahrstagung des Arbeitskreises Festkörperphysik der Deutschen Physikalischen Gesellschaft, Regensburg, Germany.
   26.-30.03.2007, Talk

6. Surface stress change during H- induced surface reconstruction on Ir(100)
   Tian, Z., W. Pan, D. Sander, J. Kirschner.
   Frühjahrstagung des Arbeitskreises Festkörperphysik der Deutschen Physikalischen Gesellschaft, Dresden, Germany.
   26.-30.03.2007, Talk

7. Nonlinear magnetoelastic coupling coefficients and magnetic anisotropy in strained Fe, Co and Ni monolayers
   Tian, Z., D. Sander, J. Kirschner
   3rd Seeheim Conference on Magnetism, Germany
   26.-30. 08.2007, Talk (accepted)

8. Large film stress and strain in ferromagnetic monolayers on Ir(100): The impact on films structure and magnetoelastic coupling

Tian, Z., D. Sander, J. Kirschner
9th European Conference on Surface Crystallography and Dynamics, Vienna, Austria 02.-05. 09. 2007, Poster (accepted)

9. Surface stress change during H-induced surface reconstruction on Ir(100)
Tian, Z., W. Pan, D. Sander, J. Kirschner
9th European Conference on Surface Crystallography and Dynamics, Vienna, Austria 02.-05. 09. 2007, Poster (accepted)